Modeling and Simulation of High-Speed Wake Flows

A DISSERTATION
SUBMITTED TO THE FACULTY OF THE GRADUATE SCHOOL
OF THE UNIVERSITY OF MINNESOTA
BY

Michael Daniel Barnhardt

IN PARTIAL FULFILLMENT OF THE REQUIREMENTS
FOR THE DEGREE OF
DOCTOR OF PHILOSOPHY

Graham V. Candler, Adviser

August 2009

Acknowledgments

The very existence of this dissertation is a testament to the support and encouragement I've received from so many individuals. Foremost among these is my adviser, Professor Graham Candler, for motivating this work, and for his considerable patience, enthusiasm, and guidance throughout the process. Similarly, I must thank Professor Ellen Longmire for allowing me to tinker around late nights in her lab as an undergraduate; without those experiences, I would've never been stimulated to attend graduate school in the first place. I owe a particularly large debt to Drs. Pramod Subbareddy, Michael Wright, and Ioannis Nompelis for never cutting me any slack when I did something stupid and always pushing me to think bigger and better. Our countless hours of discussions provided a great deal of insight into all aspects of CFD and buoyed me through the many difficult times when codes wouldn't compile, simulations crashed, and everything generally seemed to be broken. I also have to thank Travis Drayna and all of my other friends and colleagues at the University of Minnesota and NASA Ames. Dr. Matt MacLean of CUBRC and Dr. Anita Sengupta at JPL provided much of the experimental results and were very helpful throughout the evolution of the project.

Finally, I am most grateful to my family: to my parents, for their constant faith and encouragement, and especially to my wife, DeEtta, to whom this work is dedicated, for bravely putting up with me over the years.

Abstract

High-speed, unsteady flows represent a unique challenge in computational hypersonics research. They are found in nearly all applications of interest, including the wakes of reentry vehicles, RCS jet interactions, and scramjet combustors. In each of these examples, accurate modeling of the flow dynamics plays a critical role in design performance. Nevertheless, literature surveys reveal that very little modern research effort has been made toward understanding these problems. The objective of this work is to synthesize current computational methods for high-speed flows with ideas commonly used to model low-speed, turbulent flows in order to create a framework by which we may reliably predict unsteady, hypersonic flows.

In particular, we wish to validate the new methodology for the case of a turbulent wake flow at reentry conditions. Currently, heat shield designs incur significant mass penalties due to the large margins applied to vehicle afterbodies in lieu of a thorough understanding of the wake aerothermodynamics. Comprehensive validation studies are required to accurately quantify these modeling uncertainties. To this end, we select three candidate experiments against which we evaluate the accuracy of our methodology. The first set of experiments concern the Mars Science Laboratory (MSL) parachute system and serve to demonstrate that our implementation produces results consistent with prior studies at supersonic conditions. Second, we use the Reentry-F flight test to expand the application envelope to realistic flight conditions. Finally, in the last set of experiments, we examine a spherical capsule wind tunnel configuration in order to perform a more detailed analysis of a realistic flight geometry.

In each case, we find that current 1st order in time, 2nd order in space upwind numerical methods are sufficiently accurate to predict statistical measurements: mean, RMS, standard deviation, and so forth. Further potential gains in numerical accuracy are demonstrated using a new class of flux evaluation schemes in combination with 2nd order dual-time stepping. For cases with transitional or turbulent Reynolds numbers, we show that the detached eddy simulation (DES) method holds clear advantage over heritage RANS methods. From this, we conclude that the current methodology is sufficient to predict heating of external, reentry-type applications within experimental uncertainty.

Contents

List of Tables

List of Figures

Chapter 1

Introduction

1.1 Motivation

Since its conception, computational fluid dynamics has experienced a tremendous amount of development activity, transforming from a chiefly theoretical discipline to one of nearly ubiquitous practicality in the aerospace community. This process has been driven by the vision of a new industry model in which numerical experimentation largely supplants physical experimentation as the primary tool for vehicle design and research. The march toward this goal has never been uniform however, with some applications maturing rather quickly while others languish due to either complex technical challenges or a simple lack of interest from the research community. For example, over the last few decades there have been numerous notable advances in the field of hypersonics with respect to modeling of physical processes like laminar transport, chemical kinetics, radiation, and ablation. In contrast, however, the analysis of *unsteady*, hypersonic flows, about which this study is chiefly concerned, has remained largely unchanged over the last 20 years due to a combination of problem complexity, the attendant demand on computing resources, and lack of enthusiasm/funding on the part of research institutions.

To understand why we believe this is a situation which ought to be rectified, it is helpful to review what constitutes a hypersonic flow. A hypersonic flow is exemplified as having a large Mach number, typically in excess of Mach 5. The freestream enthalpy of the gas (predominantly a function of speed) is therefore often quite large. In the presence of a body, the constituent particles are forced to slow, transferring bulk kinetic energy to the molecule's internal energy modes. If the amount of transferred energy is sufficient, the molecules will begin to dissociate and possibly ionize. The rates at which these processes occur define a wide range of length and time scales. As a result, the gas is often in a state of chemical and thermal nonequilibrium. To be successful, a simulation must correctly model all of the important physics in a manner which is computationally tractable. The picture is further complicated by the addition of any number of flow features and interactions, such as shock waves, shock-shock or shock-boundary layer interactions, surface catalysis and ablation, or shock layer radiation. In spite of this complexity, CFD has demonstrated a remarkable ability to accurately capture many of the most important aspects of these flows. While acknowledging this success, it is notable that it has come almost entirely from applications in which the flow is steady and laminar. We know from experience, however, that in many applications the effects of turbulent heating are a significant contributor to overall vehicle heating. In fact, when any appreciable amount of flow unsteadiness is present, whether laminar or turbulent, it is most often offset by design margins which try to compensate for the unknown accuracy of the computational results.

As hypersonic applications become increasingly complex, the demand for computational tools capable of accurately predicting unsteady, separated flows naturally increases as well. The current practice of applying design margins is severely limiting, especially in light of the industry's post-Apollo shift toward the *"faster, better, cheaper"* ethos. A prime example is thermal protection system (TPS) design for space vehicles. The launch cost of a space vehicle is predominantly a function of its mass: more mass requires more fuel and greater vehicle complexity. In the context of the Space Shuttle, the average \$500 Million launch cost results in a net payload cost of approximately \$22,000 *per kilogram.* Thus it is critically important to a program budget that payload mass be minimized to the extent possible. One must also consider that, in the event that a launch vehicle's payload limit is exceeded, it becomes necessary to trim payload mass. In this scenario, every kilogram allocated to TPS is one which must be subtracted from the science payload, resulting in the reduction or elimination of mission objectives. Therefore, by applying margins to the TPS, programs may unnecessarily reduce risk at the expense of greater mission costs or a reduction in science payload. As of this writing, the TPS margin policy for NASA's

Crew Exploration Vehicle (CEV) lists the margin due to turbulent afterbody heating second only to that due to radiative heating.

Numerous turbulence models have been formulated over the years, from simple algebraic forms to more complex models requiring the solution of any number of differential equations. Similarly, there is a wide array of modeling *strategies* available, of which the most common can be summarized as follows. The most conceptually straightforward strategy is to simply resolve all of the relevant length and time scales through direct numerical simulation (DNS) of the Navier-Stokes equations, which obviates the need for a turbulence model but is typically too computationally expensive except at low Reynolds numbers. On the other end of the spectrum, one can choose instead to solve the Reynolds-averaged Navier-Stokes (RANS) with the intent of capturing the mean characteristics of the flow. A RANS simulation requires closure for the Reynolds stresses generated by the averaging process, and this is the objective of most turbulence modeling. In between the two extremes lies Large Eddy Simulation (LES) which seeks to resolve the largest, energy-containing scales of the flow while modeling only those motions occurring at the sub-grid scale. Each approach has its benefits and limitations, however their true utility in the context of separated hypersonic flows has never been thoroughly investigated. With few exceptions, turbulence models have been developed, calibrated, and tested within the incompressible regime.[1] Some were later extended to compressible flows through the addition of corrective terms. Over time many models have taken on an ad-hoc character from which it is impossible to extract *a priori* how the model will behave under given circumstances. Considering that the aforementioned margin policies are driven by this modeling uncertainty, it is natural to seek a means of diminishing it.

1.2 The Structure of Wake Flows

Wake flows are generally characterized by the presence of free shear layers and vortical structures emanating from behind a body. The wake can be either steady or unsteady and range from laminar to turbulent. The large-scale structures of the wake are peculiar to the vehicle geometry and its orientation to the freestream. If the Reynolds number is sufficiently large, the eddy structure begins to break down

---

[1] See Marvin and Coakley (1989) for an overview of the evolution of hypersonic turbulence modeling. Recent literature surveys have revealed few changes since the time of their publication.

and the turbulent energy is distributed across a range of scales. Moving down the spectrum to smaller scales, the eddies begin to take on a universal character before finally being eliminated by molecular dissipation.

The wake structure is influenced by the nature of the flow upstream of the separation point. At subsonic Mach numbers, the wake might consist of a series of vortices shedding from the back surface with a characteristic frequency, which then spread as they travel downstream. As the Mach number is increased past a critical point, however, the separating shear layers and strong expansion of the flow dominate the turbulent motions and keep them within a well-defined recirculating region. This is illustrated schematically in Figure 1.1 and it is representative of the types of flows considered in the current study. Under these conditions, it is useful to break the description down to near and far wake regions. The extent of the near wake region (also referred to as the recirculating region) is defined largely by the shear layer separation and expansion. Consequently, proper characterization of the forebody boundary layer as laminar, transitional, or turbulent is a crucial element to capture in a numerical simulation. Not only does it influence the point of separation but it also affects the spreading rate of the shear layers downstream. Relaminarization of the near wake has also been observed in conditions where the separating flow is subjected to a strong enough expansion. This creates a region of low-density fluid and effectively reduces the local Reynolds number. Once the separated shear layers rejoin downstream, the flow is recompressed, heating the fluid, and a recompression shock is generated. The flow in the viscous core nearly stagnates at the neck and is therefore nominally laminar as it exits into the far wake. The radial extent of the wake is suppressed significantly as the fluid continues into this region, typically consisting of a relatively thin region of vortical structures. At sufficiently high Reynolds numbers, the far wake will itself often transition to turbulence some distance downstream of the neck.

It is well understood that a turbulent flow greatly enhances mixing and transport. In the hypersonic regime, this will lead to elevated heating of the vehicle. In the boundary layer, momentum transport brings faster moving and hotter fluid near the vehicle surface, creating fuller boundary layer profiles and sharper gradients and thus enhancing convective heating. Similarly, it has been conjectured that surface catalysis may be enhanced by the presence of larger concentration gradients. In the near wake, turbulent diffusion serves to bring hot fluid in toward the body from the

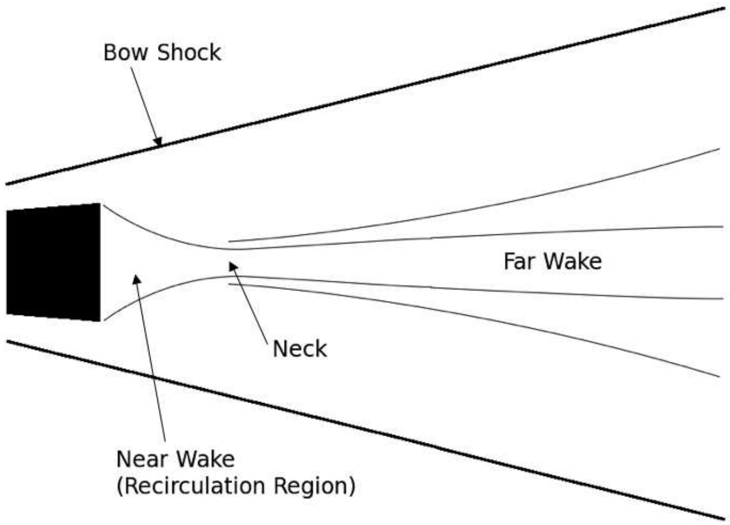

Figure 1.1: Schematic sketch of typical wake structure in a hypersonic flow.

shear layer and recompression point. The near wake region becomes uniformly hotter and exposed afterbody surfaces experience more heating. A secondary mechanism of momentum and energy redistribution results from the topological change experienced by the wake. In a laminar base flow, it is not uncommon to see peaked heating profiles along the base. This is usually the result of a single toroidal vortex drawing fluid from the hot recompression and directing it axially to the surface, whereupon the center of the vehicle base experiences a peak temperature which decreases radially outward. The situation is exacerbated if the axially impinging flow is supersonic: the formation of a disk shock on the base is then possible which will further heat the gas. In contrast, a turbulent base flow does not permit the formation of such a strong component of axial flow because instabilities break down the near wake into smaller constituent eddies. Combined with the aforementioned mixing, this results in a much more even heating distribution along the base.

1.3 Review of Related Work

The analysis of hypersonic wakes was initially stimulated in the late 1950's by the problems associated with observing and tracking slender bodies entering the Earth's atmosphere. It was discovered during this time that the entropy layer on such a configuration is enveloped by the boundary layer and thus a slender vehicle's trail is a valuable source of observables, i.e. electrons and radiating species. Initial research naturally concentrated on analytical approaches, especially the application of integral methods and the proto-computational integral-strip method (see Pallone et al. (1963) and Lien et al. (1963)). These approaches relied on finding *approximate* solutions to the far wake (assumed to be governed by the boundary layer equations) by expressing velocity and enthalpy profiles as polynomial functions.

Around this same time, the alternative approach of finding *exact* solutions to approximate, discretized equations was also being advanced and, as computational power gradually grew, the integral-strip methods gave way to finite-difference calculations. Zeiberg and Bleich (1964) provides an early such example in which the far wake (assumed again to be governed by the boundary layer equations) is computed together with models for turbulent diffusion and an eight-species chemical kinetics mechanism. Their analysis pointed out striking differences between the predicted axial profiles of momentum, temperature, and electron density of integral and finite-difference methods, yet did not provide a resolution due to a lack of experimental evidence. While their results are certainly crude by modern standards, their approach anticipated the direction of future research.

In subsequent years, up until the mid 1980's, the focus of hypersonics shifted toward blunt body analysis in which the wake problem was overshadowed by the need for accurate modeling of forebody heating. Eventually, finite-difference was replaced by the conservative finite-volume approach. The Aeroassist Flight Experiment (AFE), begun in 1988 but which was ultimately canceled, renewed interest in wake flow computations. A series of papers [Gnoffo (1990), Gnoffo et al. (1991), Venkatapathy et al. (1991)] were published which examined the structure of the laminar AFE wake. The first paper by Gnoffo, in particular, demonstrated by experimental validation that it was possible to numerically predict laminar aftbody heating with a reasonable degree of accuracy. A similar conclusion was echoed by Conti and MacCormack (1992).

In response to the formation of AGARD Working Group 18, a panel meant to address issues related to blunt body wake flowfields, two independent test programs were initiated. In Horvath et al. (1996) and Horvath and Hannemann (1997), numerical and experimental results were obtained on a 6-in. diameter 70° blunted cone at

Mach 6 and 10, respectively. An especially interesting outcome of these studies was confirmation that heating due to shear layer impingement could actually be greatest when the shear layer was transitional, versus purely laminar or turbulent. Numerical comparisons were somewhat inconclusive however because of the use of an axisymmetric formulation and lack of a turbulence model, in contradiction to the experimental data which suggested a transitional/turbulent shear layer. Holden et al. (1997) tested an identical configuration using a variety of numerical techniques, ranging from Direct Simulation Monte-Carlo (DSMC) to continuum Navier-Stokes simulations and several hybrid combinations thereof. Again, the flow was treated axisymmetrically and assumed to be laminar. Base pressure and heat transfer were generally in poor agreement with experimental data, especially so for the Navier-Stokes calculations. Expansion of the base flow to a rarefied state was raised as a possible explanation for the error, although results of hybrid DSMC/Navier-Stokes calculations presented in the study seem to suggest that this effect is not solely accountable.

Within the past decade, the wake problem has been revisited in light of NASA's high-profile Mars Science Laboratory (MSL) and CEV missions. It is common for these types of missions to employ safety margins on unsteady/turbulent afterbody heating in excess of 50-100%. Wright et al. (2006) performed an in-depth analysis of available data from the Apollo AS-202 flight test. The flow was uniformly laminar throughout the trajectory and agreement was generally fair in light of the estimated 20% uncertainty in the flight data. Still, several of the gauge locations showed gross error and the authors acknowledged unsteadiness in the computations which was not accounted for in the analysis. A similar attempt was made to examine afterbody heating of Viking Lander 1 in Edquist et al. (2006). This study relied on the same methodology as in the AS-202 study. Results were not very favorable for a variety of proposed reasons including underestimation of conduction effects in the heatshield, improper modeling of surface catalysis, and various limitations of the computational methods. In fact, these very methods, although they are still widely regarded as the state of the art in aerothermal modeling today, originated over 20 years ago.

Over the same period of years, computational analysis of *low-speed* wake flows was progressing rapidly. Numerous advances were made to improve time accuracy, spatial accuracy, and turbulence modeling. A strong interplay between the experimental and computational communities ensured that methods were continuously evolving in order to reach their limits of numerical efficiency and fidelity. One is free to speculate as to why similar ideas have not always been adapted for use by the hypersonics community. To be sure, oftentimes the reason is simply a matter of considering the vastly different physics of high-speed, compressible flows. Nevertheless, it is apparent that a certain disparity exists between the quality of modeling used for low-speed flows and that used in the hypersonic regime.

1.4 Scope of Present Work

From the studies we have cited, we may conclude the following about the current state of the art:

1. Despite nearly 50 years of research, analysis of high-speed, unsteady wake flows remains a very difficult and unsolved problem.

2. No single methodology has been advanced within the hypersonic community by which this type of analysis can be consistently performed with confidence.

3. There is a dearth of validation studies by which a researcher may be guided to adopt a consistent methodology.

4. Little effort has been made to incorporate successful ideas from the low-speed modeling world.

This study seeks to alleviate some of the ambiguity surrounding the simulation of unsteady flows under hypersonic conditions. Influenced by ideas used to successfully model low-speed flows, we adopt a strategy which minimizes the dependence on modeling assumptions and develop a methodology that is capable of reliably predicting an unsteady aerothermal environment. The utility and robustness of the approach are confirmed through comprehensive validation of numerical results with several sets of available experimental data.

Chapters 2 and 3 present the governing equations and mathematical framework by which they are solved. In Chapter 4, we apply the developed methodology to the MSL parachute problem. The analysis is used to establish confidence in the current implementation and to bridge the gap between prior supersonic flow analyses and the hypersonic flows which are our primary interest. In Chapter 5, we analyze the results of the Mach 20 Reentry-F flight experiment in order to establish the efficacy of our methodology at realistic reentry conditions. The analysis reveals some ambiguity regarding the original flight data which is resolved through a basic sensitivity analysis. Finally, in Chapter 6, we use a series of ground tests of a spherical capsule geometry to 1) allay concerns raised by the ambiguity of the Reentry-F experiment, and 2) establish the efficacy of our methodology for realistic capsule geometries.

Chapter 2

Mathematical Formulation

2.1 Introduction

In this section, we introduce the coupled set of equations governing the dynamics of a compressible flowfield. For a thermally perfect gas, the Navier-Stokes equations along with an appropriate equation of state are sufficient to describe the transport of mass, momentum, and energy. Under certain flow conditions presented in this work, the gas may become sufficiently energetic such that various chemical and thermal relaxation processes are activated. The extension of the Navier-Stokes equations to incorporate real-gas effects has been reviewed previously in a number of sources [see, for example, Candler (1988)] and so will only be presented briefly here. Modeling of the reaction chemistry, energy relaxation, and diffusive transport processes is discussed for use when appropriate. Additionally, we seek to simulate turbulent, unsteady flows and therefore incorporate a coupled turbulence model into our equation set. While there are numerous choices available, we restrict our presentation to the one equation Spalart-Allmaras (S-A) model.

2.2 Basic Assumptions

It is assumed that the flows of interest are adequately described by a continuum formulation. For this to be true, the Knudsen parameter, defined as $Kn = \lambda/L$, must in general have a value much less than 1. Here, λ is defined as the mean free path of the gas particles and L is a characteristic length of the vehicle. The most rarefied condition that we shall consider is at an altitude of 80,000 feet. At this altitude, λ is on the order of 10 μm and we can therefore expect our results to lie well within the continuum regime.

Flows in thermochemical nonequilibrium are assumed to be governed by a two temperature model. Rotational and translational energy modes of a molecule typically equilibrate within five collisions and so the translational-rotational state of the gas is described by a single temperature, T. Vibrational nonequilibrium may be appreciable through a strong shock however. It is assumed that the vibrational modes are strongly coupled and that a single vibrational temperature T_v is sufficient to describe this energy mode. Rotation-vibration coupling is not appreciable at the temperatures considered in this work and is neglected.

The Spalart-Allmaras model was developed for use in incompressible simulations and subsequently modified [Catris and Aupoix (2000)] to account for compressibility effects. It is assumed that this model is applicable across the entire range of flow conditions encountered herein. In fact, to our knowledge, this has not been shown previously and so to a degree the results of this work will stand as a validation of this assumption.

2.3 Navier-Stokes Equations

The derivation of the Navier-Stokes equations, which describe the transport of mass, momentum, and energy in a viscous, compressible fluid, can be found in numerous textbooks and other sources. For flows in chemical and thermal nonequilibrium, the set of equations is extended to account for individual species conservation and transfer of energy between various internal modes. While only some of the results presented here incorporate nonequilibrium effects, we present the full equation set (developed under the assumptions outlined above) for completeness.

For a chemically reacting flow, it is necessary to solve ns individual species conservation equations. The conservation of mass of chemical species s is given by the following relation

$$\frac{\partial \rho_s}{\partial t} + \frac{\partial}{\partial x_i}(\rho_s u_i) = -\frac{\partial}{\partial x_i}(\rho_s v_{si}) + w_s \tag{2.1}$$

Here v_{si} are the velocity vector components due to diffusion and w_s is a source term which governs production of the species through chemical processes. The individual species velocities are approximated by the mass-averaged velocity, defined as

$$u_i = \sum_{s=1}^{\mathrm{ns}} \frac{\rho_s}{\rho} u_{si}$$

By summing this equation over all species, the source terms add identically to zero and we recover the traditional continuity equation.

The mass-averaged momentum transport equation is expressed as

$$\frac{\partial}{\partial t}(\rho u_i) + \frac{\partial}{\partial x_j}(\rho u_i u_j) = -\frac{\partial p}{\partial x_i} + \frac{\partial \tau_{ij}}{\partial x_j} \tag{2.2}$$

where p denotes pressure and τ_{ij} is the viscous stress tensor. An equation of this type is solved for each spatial degree of freedom. Note that the mass-averaged diffusion velocity is identically zero and therefore does not appear on the right-hand side.

For flows in thermal nonequilibrium, we model energy transport with a series of equations for the individual internal modes and the total energy. According to our basic set of assumptions, rotational energy is in equilibrium with the translational mode and therefore a separate rotational energy equation is not required. The vibrational energy equation takes the form

$$\frac{\partial E_v}{\partial t} + \frac{\partial}{\partial x_i}(E_v u_i) = -\frac{\partial q_{vi}}{\partial x_i} - \frac{\partial}{\partial x_i} \sum_{s=1}^{\mathrm{nd}} \rho_s e_{vs} v_{si} + \sum_{s=1}^{\mathrm{nd}} w_s e_{vs} + Q_{T-V} \tag{2.3}$$

where q_{vi} are the components of the vibrational heat conduction vector and Q_{T-V} is a source term which describes the transfer of energy between translational and vibrational modes. The second and third terms on the right hand side represent change of vibrational energy due to diffusion and chemical production, respectively. The total energy equation is represented as

$$\frac{\partial E}{\partial t} + \frac{\partial}{\partial x_i}(E + p)u_i = \frac{\partial}{\partial x_j}(\tau_{ij} u_i) - \frac{\partial}{\partial x_i}(q_i + q_{vi}) - \frac{\partial}{\partial x_i} \sum_{s=1}^{\mathrm{ns}} \rho_s h_s v_{si} \tag{2.4}$$

In this equation, q_i denote the components of the translational-rotational heat flux vector. As with equation (2.3), the final term on the right-hand side represents the transfer of energy due to diffusion.

These equations have been written with the inviscid flux contributions on the left-hand side and viscous fluxes and source terms on the right-hand side. To close the set, we must introduce a state equation. Additionally, several terms on the right-hand side are subject to constitutive relations or models to complete the description. These will be presented in a subsequent section.

2.4 Spalart-Allmaras Turbulence Model

We wish to simulate turbulent, unsteady flows. Instead of performing a direct numerical simulation, which would be far too computationally expensive, we choose to augment our initial equation set with another equation to model the unresolved turbulent features. A wide variety of options are available for this purpose, including algebraic, one-equation, two-equation, and Reynolds stress models. In this work, we opt to use the S-A model, in part because of its simplicity but also because it is the model most traditionally used in formulating detached eddy simulation (DES) which forms the basis of our investigations.

The S-A model was created initially in response to the complexity of popular two-equation models. Inspired by the similar one-equation Baldwin-Barth model, the authors set out to construct a generic transport equation for eddy viscosity and then tuned the adjustable parameters to reflect an array of validation cases. The result is a model built from a blend of analysis and empiricism that has demonstrated a remarkable robustness across a range of aerodynamic flows. Having been developed primarily for subsonic, incompressible flows, it has subsequently been extended to incorporate compressibility effects. It is assumed in this work that the compressible form of the equation is applicable to the conditions of interest.

The compressible form of the S-A model suggested by Catris and Aupoix (2000) takes the form

$$\frac{D\rho\tilde{\nu}}{Dt} = \frac{1}{\sigma}\left[\nabla\cdot\left(\mu\nabla\tilde{\nu} + \sqrt{\rho}\tilde{\nu}\nabla\sqrt{\rho}\tilde{\nu}\right) + c_{b2}\left(\nabla\sqrt{\rho}\tilde{\nu}\right)^2\right] + c_{b1}\rho\tilde{S}\tilde{\nu} - c_{w1}f_w\rho\left(\frac{\tilde{\nu}}{d}\right)^2 \tag{2.5}$$

Rather than modeling eddy viscosity transport directly (as is the case with the high Reynolds number form), the equation models transport of $\tilde{\nu}$ which is related to the eddy viscosity through the following definitions:

$$\nu_T = \tilde{\nu} f_{v1} \qquad \text{where} \qquad f_{v1} = \frac{\chi^3}{\chi^3 + c_{v1}^3} \qquad \text{and} \qquad \chi = \frac{\tilde{\nu}}{\nu}$$

where ν is the kinematic molecular viscosity (note also the appearance of the dynamic molecular viscosity μ in equation (2.5)). The modified equation ensures that boundary layer profiles in the near wall region are correctly modeled. The remaining functions to be defined are

$$\tilde{S} = S + \frac{\tilde{\nu}}{\kappa^2 d^2} f_{v2} \qquad \text{where} \qquad f_{v2} = 1 - \frac{\chi}{1 + \chi f_{v1}}$$

and

$$f_w = g \left(\frac{1 + c_{w3}^6}{g^6 + c_{w3}^6} \right)^{1/6} \qquad \text{where} \qquad g = r + c_{w2}(r^6 - r) \qquad \text{and} \qquad r = \frac{\tilde{\nu}}{\tilde{S} \kappa^2 d^2}$$

The constants, $c_{(x)}$, κ, and σ, are provided in the Appendix. The interested reader is referred to Spalart and Allmaras (1992) for details on the form and calibration of the control functions outlined above.

The first three terms on the right-hand side of equation (2.5) are diffusive and function to preserve smoothness of the solution. The fourth term controls production and is proportional to the magnitude of vorticity, S. This is balanced in the near wall region by the final destruction term which depends on the wall distance, d. Later it will be convenient to refer to the S-A source term as

$$w_{\tilde{\nu}} = \frac{c_{b2}}{\sigma} \left(\nabla \sqrt{\rho} \tilde{\nu} \right)^2 + c_{b1} \rho \tilde{S} \tilde{\nu} - c_{w1} f_w \rho \left(\frac{\tilde{\nu}}{d} \right)^2$$

2.5 Equations of State and Constitutive Relations

An equation of state is required to provide a relationship among thermodynamic variables and close the system of governing equations. This is given by the perfect gas law for a multicomponent gas mixture:

$$p = \sum_{s=1}^{\text{ns}} \rho_s \frac{R}{M_s} T = \rho \bar{R} T, \qquad \text{where} \qquad \bar{R} \equiv \sum_{s=1}^{\text{ns}} \frac{\rho_s}{\rho} \frac{R}{M_s},$$

R is the universal gas constant, and M_s is the species molecular weight. It remains to provide relationships between the conserved and primitive variables.

The total energy per unit volume of the gas is simply a sum of the separate energy components and may be written as

$$E = \sum_{s=1}^{\text{ns}} \rho_s C_{\text{v}s} T + \frac{1}{2}\rho u_i u_i + \sum_{s=1}^{\text{nd}} \rho_s e_{vs} + \sum_{s=1}^{\text{ns}} \rho_s h_s^\circ$$

where nd indicates the polyatomic subset of species, and $C_{\text{v}s}$ is the translational-rotational specific heat at constant volume. It is computed as

$$C_{\text{v}s} = C_{\text{v}s}^{(tr)} + C_{\text{v}s}^{(rot)} = \frac{3}{2}\frac{R}{M_s} + \frac{R}{M_s}$$

Note that the rotational contribution of specific heat is only relevant to the nd polyatomic species. The first term in the energy equation therefore is the energy due to translational-rotational motions of the particles. The second term is the bulk kinetic energy. The third term is internal energy stored by polyatomic species in vibrational modes and is equivalent to E_v. The vibrational energy per unit mass is derived from statistical mechanics to be

$$e_{vs} = \frac{R}{M_s}\frac{\theta_{vs}}{\exp\left(\theta_{vs}/T_v\right) - 1}$$

where θ_{vs} is the characteristic vibrational temperature of species s (specific values are listed in the Appendix) and T_v is the vibrational temperature. This expression in effect serves as a definition for T_v, however it is not directly invertible and the vibrational temperature must be computed using an iterative procedure. The final term in the total energy expression represents the energy of formation. The values of the formation enthalpies h_s° are provided in the Appendix.

The fluid is assumed to be Newtonian such that the viscous stress tensor is proportional to gradients of the velocity field

$$\tau_{ij} = \mu\left(\frac{\partial u_i}{\partial x_j} + \frac{\partial u_j}{\partial x_i} - \frac{2}{3}\frac{\partial u_k}{\partial x_k}\delta_{ij}\right) + \mu_B \frac{\partial u_k}{\partial x_k}\delta_{ij}$$

Furthermore, we apply the Stokes assumption for the bulk viscosity so that

$$\mu_B = 0$$

Heat conduction is assumed to be governed by Fourier's law, where

$$\begin{aligned} q_i &= -\left(\kappa_t + \kappa_r\right)\frac{\partial T}{\partial x_i} \\ q_{vi} &= -\,\kappa_v \frac{\partial T_v}{\partial x_i} \end{aligned}$$

and κ_t, κ_r, and κ_v are the thermal conductivities corresponding to the translational, rotational, and vibrational energy modes. The diffusive transport coefficients for mass, momentum, and energy are dependent on the state of the fluid. The models used to compute them in this work will be discussed in further detail in the next section.

2.6 Diffusive Transport Models

2.6.1 Mass Diffusion

In general, mass diffusion is driven by gradients of temperature, pressure, and concentration. If the flow becomes ionized, it may also be influenced by the presence of electromagnetic fields. Gas temperatures do not exceed 6,000 K in the flows of interest, however, and therefore diffusion of the gas will not be influenced by electromagnetic fields. Thermal gradients are typically only important in rarefied flows where the continuum assumption breaks down. In this regime, one must resort to particle-based computational methods and so this class of flows is not considered. Similarly, diffusion due to pressure gradients is assumed to be negligible. What remains is the familiar expression of Fick's Law for the diffusive flux, written in terms of mole and mass fractions as

$$\mathbf{J}_s = \rho_s \vec{v}_s = -\gamma M_s D_s \nabla X_s = -\rho D_s \nabla c_s$$

where γ is the concentration, D_s is the mixture diffusion coefficient, and X_s and c_s are the mole and mass fractions, respectively, of species s. It has been noted [Ramshaw and Chang (1991)] that this formulation is not consistent with respect to mass conservation and corrections have been proposed which distribute the approximation error among the species. This approach has not been applied to the present work, however its use in conjunction with the Gupta-Yos transport model will be discussed in a subsequent section. The concentration is defined as

$$\gamma = \sum_{s=1}^{\mathrm{ns}} \frac{\rho_s}{M_s} = \frac{\rho}{M} \qquad \text{with} \qquad M^{-1} = \sum_{s=1}^{\mathrm{ns}} \frac{c_s}{M_s}$$

We assume in this work that, in the absence of light species like hydrogen, the species-specific mixture diffusion coefficients can be approximated by a single diffusion coefficient. Hence, we derive the diffusion coefficient using the Lewis number definition

$$\mathrm{Le} = D\frac{\rho C_{\mathrm{p}}}{\kappa}$$

where $C_{\mathrm{p}} = C_{\mathrm{v}} + \bar{R}$ is the translational-rotational specific heat at constant pressure, κ is the mixture thermal conductivity, and the Lewis number is assumed constant and equal to 1.4.

2.6.2 Momentum Diffusion

Momentum diffusion is modeled through the action of viscosity. Blottner curve fits are used in this work to calculate coefficients for the individual species. The curve fits are given as functions of temperature and are valid up to 10,000 K. They have the following form

$$\mu_s = 0.1 \exp\big((A_s \ln T + B_s) \ln T + C_s\big)$$

Values of A_s, B_s, and C_s are given in the Appendix. The viscosity of the gas is then obtained by means of Wilke's mixing rule

$$\mu = \sum_{s=1}^{\mathrm{ns}} \frac{X_s \mu_s}{\phi_s}$$

where

$$\phi_s = \sum_{r=1}^{\mathrm{ns}} X_r \left[1 + \sqrt{\frac{\mu_s}{\mu_r}} \left(\frac{M_r}{M_s}\right)^{1/4}\right]^2 \left[\sqrt{8\left(1 + \frac{M_s}{M_r}\right)}\right]^{-1}$$

2.6.3 Energy Diffusion

Thermal conductivities are calculated according to an Eucken relation [Vincenti and Kruger (1982)] as

$$\kappa_{ts} = \frac{5}{2}\mu_s C_{\mathrm{vs}}^{(tr)}, \qquad \kappa_{rs} = \mu_s C_{\mathrm{vs}}^{(rot)}, \qquad \kappa_{vs} = \mu_s C_{\mathrm{vs}}^{(vib)}$$

and mixed via Wilke's mixing rule. The vibrational specific heat is found from its definition to be

$$C_{\mathrm{vs}}^{(vib)} = \frac{\partial e_{vs}}{\partial T_v} = \frac{R}{M_s}\left(\frac{\theta_{vs}}{T_v}\right)^2 \frac{\exp\left(\theta_{vs}/T_v\right)}{\left(\exp\left(\theta_{vs}/T_v\right) - 1\right)^2}$$

2.6.4 Improved Models

The transport models presented thus far, while adequate for the flows of interest, are not suitable for all conditions one may encounter nor do they represent the latest level of modeling sophistication. Their use in the present work was adopted early on as a matter of convenience. However, more generally appropriate models exist and they are accurate over a much greater range of conditions, including ionization of the gas. We believe, therefore, that their use should be preferred in most circumstances. In this spirit, we now review the transport models of Ramshaw and Chang (1991) and Gupta et al. (1990).

The Self-Consistent Effective Binary Diffusion (SCEBD) formulation of Ramshaw and Chang eliminates mass conservation error that arises from the computation of mass diffusion fluxes by distributing it amongst species according to their mass fractions. Thus Fick's Law is recast as

$$\mathbf{J}_s = \gamma\left[-M_s D_s \nabla X_s + c_s \sum_{j=1}^{\mathrm{ns}} M_j D_j \nabla X_j\right]$$

so that the sum over $\mathbf{J}_s$ is enforced to be identically zero. For ionized gases, one includes an additional term to account for the electric field, $\mathbf{E}$

$$\mathbf{J}_s = \gamma\left[-M_s D_s \nabla X_s + c_s \sum_{j=1}^{\mathrm{ns}} M_j D_j \nabla X_j\right] + \frac{\gamma}{p}\left[M_s q_s \rho_s D_s - c_s \sum_{j=1}^{\mathrm{ns}} M_j q_j \rho_j D_j\right]\mathbf{E}$$

where q_s is the charge per unit mass of species s. The electric field can be derived from this expression by applying the ambipolar assumption, $\mathbf{J}_q = \sum q_s \mathbf{J}_s = 0$. While this approach is somewhat more complicated than that presented earlier, it is more physically correct in general and thus applicable to a much broader class of flows.

Several different methods for computing the coefficients of mass, momentum, and energy transport are found in the work of Gupta et al. (1990). Here, the authors apply additional approximations to the Chapman-Enskog procedure to obtain the following accurate yet practical forms

$$\begin{aligned}
D_{ij} &= \frac{kT}{p\Delta_{ij}^{(1)}} \\
\mu &= \frac{1}{N_A} \sum_i \left(\frac{M_i X_i}{\sum_j X_j \Delta_{ij}^{(2)}} \right) \\
\kappa &= \underbrace{\frac{15}{4} k \sum_i \left(\frac{X_i}{\sum_j \alpha_{ij} X_j \Delta_{ij}^{(2)}} \right)}_{translational} + \underbrace{\frac{1}{N_A} \sum_i \left(\frac{C_{\mathrm{p}_i}^{(int)} M_i X_i}{\sum_j X_j \Delta_{ij}^{(1)}} \right)}_{internal}
\end{aligned}$$

where the subscripts i and j indicate individual species, k is the Boltzmann constant, N_A is Avogadro's number, and $\Delta_{ij}^{(l)}$ are related to the collision integrals, $\pi\overline{\Omega}_{ij}^{(l,l)}$. The complete expressions, as well as that for α_{ij}, are provided in the Appendix. The momentum and energy transport coefficients, μ and κ, are expressed as mixture properties. D_{ij} is the binary diffusion coefficient and is related to the mixture diffusion coefficient by

$$\frac{(1 - X_s)}{D_s} = \sum_{j=1}^{\mathrm{ns}} \frac{X_j}{D_{js}}$$

2.7 Source Terms

The source terms w_s which appear in the mass conservation equations represent the rate of production (both positive and negative) of species s due to chemical reactions. Similarly, Q_{T-V} is the rate of energy exchange between translational and vibrational modes. In this section, we present models for the source terms, which will then close our set of governing equations.

The flows of interest all have air as the freestream gas and can be described with either a single species perfect gas model or, if dissociation occurs, a five species chemical kinetics model. In practice, the single species model is treated in the same manner as a multi-species model with the exception that the chemical source term is absent. The five species chemical kinetics model consists of N_2, O_2, NO, N, and O. The relevant chemical reactions are

$$\begin{aligned}
\mathrm{N_2 + M} &\rightleftharpoons \mathrm{2N + M} && (1)\\
\mathrm{O_2 + M} &\rightleftharpoons \mathrm{2O + M} && (2)\\
\mathrm{NO + M} &\rightleftharpoons \mathrm{N + O + M} && (3)\\
\mathrm{N_2 + O} &\rightleftharpoons \mathrm{NO + N} && (4)\\
\mathrm{NO + O} &\rightleftharpoons \mathrm{O_2 + N} && (5)
\end{aligned}$$

The first three reactions are dissociation reactions for the diatomic species due to collisions. In the forward dissociative direction, M is an arbitrary collision partner whose relative kinetic energy provides the energy necessary to break the chemical bond. The reverse recombination process has M absorbing the energy released by the recombining pair. The final two reactions are the Zeldovich exchange reactions.

The chemical source terms are formed by summing the reaction rates. The rates of reaction can be written in an Arrhenius form and are governed by forward and backward rate coefficients k_{fr} and k_{br}. Then the rate of reaction is simply the sum of the forward and backward rates

$$\begin{aligned}
\mathcal{R}_1 &= \sum_m \left[k_{b1_m} \frac{\rho_{\mathrm{N}}}{M_{\mathrm{N}}} \frac{\rho_{\mathrm{N}}}{M_{\mathrm{N}}} \frac{\rho_m}{M_m} - k_{f1_m} \frac{\rho_{\mathrm{N_2}}}{M_{\mathrm{N_2}}} \frac{\rho_m}{M_m} \right]\\
\mathcal{R}_2 &= \sum_m \left[k_{b2_m} \frac{\rho_{\mathrm{O}}}{M_{\mathrm{O}}} \frac{\rho_{\mathrm{O}}}{M_{\mathrm{O}}} \frac{\rho_m}{M_m} - k_{f2_m} \frac{\rho_{\mathrm{O_2}}}{M_{\mathrm{O_2}}} \frac{\rho_m}{M_m} \right]\\
\mathcal{R}_3 &= \sum_m \left[k_{b3_m} \frac{\rho_{\mathrm{N}}}{M_{\mathrm{N}}} \frac{\rho_{\mathrm{O}}}{M_{\mathrm{O}}} \frac{\rho_m}{M_m} - k_{f3_m} \frac{\rho_{\mathrm{NO}}}{M_{\mathrm{NO}}} \frac{\rho_m}{M_m} \right]\\
\mathcal{R}_4 &= k_{b4} \frac{\rho_{\mathrm{NO}}}{M_{\mathrm{NO}}} \frac{\rho_{\mathrm{N}}}{M_{\mathrm{N}}} - k_{f4} \frac{\rho_{\mathrm{N_2}}}{M_{\mathrm{N_2}}} \frac{\rho_{\mathrm{O}}}{M_{\mathrm{O}}}\\
\mathcal{R}_5 &= k_{b5} \frac{\rho_{\mathrm{O_2}}}{M_{\mathrm{O_2}}} \frac{\rho_{\mathrm{N}}}{M_{\mathrm{N}}} - k_{f5} \frac{\rho_{\mathrm{NO}}}{M_{\mathrm{NO}}} \frac{\rho_{\mathrm{O}}}{M_{\mathrm{O}}}
\end{aligned}$$

The resulting source terms are written as

$$
\begin{aligned}
w_{\mathrm{N}_2} &= M_{\mathrm{N}_2}\left(\mathcal{R}_1 + \mathcal{R}_4\right) \\
w_{\mathrm{O}_2} &= M_{\mathrm{O}_2}\left(\mathcal{R}_2 - \mathcal{R}_5\right) \\
w_{\mathrm{NO}} &= M_{\mathrm{NO}}\left(\mathcal{R}_3 - \mathcal{R}_4 + \mathcal{R}_5\right) \\
w_{\mathrm{N}} &= M_{\mathrm{N}}\left(-2\mathcal{R}_1 - \mathcal{R}_3 - \mathcal{R}_4 - \mathcal{R}_5\right) \\
w_{\mathrm{O}} &= M_{\mathrm{O}}\left(-2\mathcal{R}_2 - \mathcal{R}_3 + \mathcal{R}_4 + \mathcal{R}_5\right)
\end{aligned}
$$

The reaction rate coefficients may be assumed to be functions of temperature and expressed in a modified Arrhenius form. The Park model has been chosen for this work: it has been used extensively and has performed well under a variety of flow conditions [Olejniczak (1997)]. This model further assumes that the reaction rate is governed by an effective temperature T_a, which depends on the type of reaction

$$
\begin{aligned}
k_{fr_m}(T_a) &= C_{f_m} T_a^{\eta_m} \exp\left(-\theta_m / T_a\right) \\
k_{br_m}(T_a) &= \frac{k_{fr_m}(T_a)}{K_{c_m}}
\end{aligned}
$$

The reaction constants C_{f_m}, η_m, and θ_m are provided in the Appendix for a five species chemical kinetic air model. For the dissociation reactions, the forward rate will be a function of the vibrational excitation of the dissociating molecule as well as the translational energy of the impacting particle. Thus we can reason that the governing temperature for these reactions will be of the form

$$
T_a = T^q T_v^{1-q} \qquad 0 < q < 1
$$

For most flows of interest, $\eta = 0.5$ as specified by Park (1989) provides good results and the governing temperature is simply the geometric average of the translational and vibrational energy states. Recombination rates will depend only on the translational temperature, however, since the recombining particles are atomic and therefore do not possess vibrational energy. For this case, $T_a = T$.

The equilibrium constant K_{c_m} (here the subscript c signifies an expression in terms of *concentration* units) is derived either directly or indirectly from curve fits to experimental data. An example of the direct method is provided by Park (1990)

$$K_{c_m} = C_m \exp\left(A_{1m}Z^{-1} + A_{2m} + A_{3m} \ln Z + A_{4m}Z + A_{5m}Z^2\right)$$

where $Z = 10,000/T$ and the constants are given for each reaction m. An alternative approach is to incorporate experimental data indirectly through calculation of equilibrium thermodynamic variables in combination with an expression of Gibbs free energy, which at equilibrium may be written as

$$\begin{aligned} \Delta G_m &= \Delta G^\circ_m + RT \ln K_{p_m} \\ &= \Delta H^\circ_m - T\Delta S^\circ_m + RT \ln K_{p_m} \\ &= 0 \end{aligned} \tag{2.6}$$

where ΔG_m, ΔH_m, and ΔS_m are the changes in Gibbs energy, enthalpy, and entropy, respectively, as a result of reaction m. Superscripts indicate quantities associated with formation of a compound in its standard state. Note that K_{p_m} is the equilibrium constant in *pressure* units and is related to K_{c_m} [Kee (2003)] by

$$K_{c_m} = K_{p_m}\left(\frac{p_\circ}{RT}\right)^{\nu_m} \qquad \text{where} \qquad \nu_m \equiv \sum_s \left(\nu''_{sm} - \nu'_{sm}\right)$$

and ν_{sm} are the stoichiometric coefficients of species s in reaction m. A single accent mark indicates a reactant while a double accent indicates a product. $P_\circ$ is the standard state pressure equivalent to 1 bar (10^5 Pa). Using the forgoing relation, it is useful to recast equation (2.6) in the following form for ease of computation

$$\begin{aligned} K_{c_m} &= \left(\frac{p_\circ}{RT}\right)^{\nu_m} \exp\left[-\frac{\Delta H^\circ_m}{RT} + \frac{\Delta S^\circ_m}{R}\right] \\ &= \left(\frac{p_\circ}{RT}\right)^{\nu_m} \exp\left[-\sum_s \left(\nu''_{sm} - \nu'_{sm}\right)\left(\frac{H^\circ_s}{RT} - \frac{S^\circ_s}{R}\right)\right] \end{aligned}$$

The nondimensionalized enthalpy and entropy are readily obtained from Gordon and McBride (1994). The data are published as curve fits for multiple temperature intervals up to 20,000 K

$$\frac{H_s^\circ}{RT} = -\, a_{1s}T^{-2} + a_{2s}T^{-1}\ \ln\, T + a_{3s} + a_{4s}\frac{T}{2} + a_{5s}\frac{T^2}{3} + a_{6s}\frac{T^3}{4} + a_{7s}\frac{T^4}{5} + \frac{a_{8s}}{T}$$

$$\frac{S_s^\circ}{R} = -\, a_{1s}\frac{T^{-2}}{2} - a_{2s}T^{-1} + a_{3s}\ \ln\, T + a_{4s}T + a_{5s}\frac{T^2}{2} + a_{6s}\frac{T^3}{3} + a_{7s}\frac{T^4}{4} + a_{9s}$$

This approach is known to provide a more accurate calculation of K_{c_m} across a wider range of temperatures than the Park method and it is therefore generally preferred. The a_{js} coefficients relevant to this work have been published in multiple sources, including Gordon and McBride (1999) and Zehe et al. (2002).

Finally, we must address the term representing energy transfer between translational and vibrational energy modes Q_{T-V}. The rate at which the vibrational energy of species s tends toward equilibrium is described by the Landau-Teller formulation

$$Q^{(LT)}_{T-V_s} = \rho_s \frac{e^*_{vs} - e_{vs}}{< \tau_s >}$$

where e^*_{vs} is the specific vibrational energy evaluated at the equilibrium translational temperature. Thus the rate of energy exchange is seen to be proportional to the deviation from equilibrium of the vibrational mode. The molar-averaged Landau-Teller relaxation time $< \tau_s >$ is given by Lee (1985)

$$< \tau_s > = \frac{\sum_r X_r}{\sum_r X_r/\tau_{sr}}$$

and the inter-species relaxation times τ_{sr} can be found in Millikan and White (1963) as

$$\begin{aligned} \tau_{sr} &= \frac{1}{p}\exp\left[A_{sr}\left(T^{-1/3} - 0.015\mu_{sr}^{1/4}\right) - 18.42\right] \qquad\qquad (p \text{ in atm}) \\ A_{sr} &= 1.16\times 10^{-3}\mu_{sr}^{1/2}\theta_{vs}^{4/3} \\ \mu_{sr} &= \frac{M_s M_r}{M_s + M_r} \end{aligned}$$

The total rate of energy exchange is simply the sum of contributions from the vibrationally excited species

$$Q_{T-V} = \sum_{s=1}^{\mathrm{nd}} Q^{(LT)}_{T-V_s}$$

The complete source term for vibrational energy is then comprised of this term along with the contribution due to chemical production of vibrationally excited species

$$w_v = Q_{T-V} + \sum_{s=1}^{\mathrm{nd}} w_s e_{vs}$$

Chapter 3

Numerical Method

3.1 Introduction

This chapter provides an overview of the basic numerical methods employed in this work, as well as a detailed presentation of the methodology adopted for computing high-speed, unsteady flows. The implicit, finite volume methods developed in Wright (1997) form the backbone of our solution procedure for the governing equations discussed in the previous chapter. In addition to this, we use the DES approach advanced by Spalart et al. (1997) for computing unsteady flows. To the author's knowledge, this is a feature heretofore unexplored in the hypersonic regime. Several numerical considerations arise from the discussion of time-accurate, unsteady computations and these are explained along with potential approaches for addressing each.

3.2 Basic Formulation

The finite volume method of discretization is derived from consideration of the weak formulation of the governing equations. For ease of presentation, we show only the two-dimensional case; note however that extension of the procedure to three dimensions (and incorporating any number of additional coupled equations) is straightforward. Beginning from the strong form of the equations presented in the previous chapter, we may write the vector of conserved variables as

$$U = (\rho_1, \ldots, \rho_{\mathrm{ns}}, \rho u, \rho v, E_v, E, \rho\tilde{\nu})^T \tag{3.1}$$

which leads to the following compact form of the conservation equations

$$\frac{\partial U}{\partial t}+\frac{\partial F}{\partial x}+\frac{\partial G}{\partial y}=W \tag{3.2}$$

where F and G denote the flux vectors in the x and y directions, and W contains the source terms

$$W=\left(w_1,\ldots,w_{\mathrm{ns}},0,0,w_v,0,w_{\tilde{\nu}}\right)^T$$

The flux can be split into convective (inviscid) and diffusive components. This is useful so that one may apply different flux evaluation methods to the components in order to take advantage of their differing character. Thus the total flux (of the x-component) is expressed as

$$F=F_I+F_V$$

where the Cartesian components of the flux vectors are found to be

$$F_I=\begin{pmatrix}\rho_1 u\\ \vdots\\ \rho_{\mathrm{ns}} u\\ \rho u u+p\\ \rho v u\\ E_v u\\ (E+p)\,u\\ \rho\tilde{\nu} u\end{pmatrix}\qquad F_V=\begin{pmatrix}-\rho D\frac{\partial}{\partial x}c_1\\ \vdots\\ -\rho D\frac{\partial}{\partial x}c_{\mathrm{ns}}\\ -\tau_{xx}\\ -\tau_{yx}\\ q_{v_x}+\sum\rho_s e_{vs}v_{s1}\\ q_x+q_{v_x}-\tau_{xx}u-\tau_{yx}v+\sum\rho_s h_s v_{s1}\\ -(\mu/\sigma)\frac{\partial}{\partial x}\tilde{\nu}-(\sqrt{\rho}\tilde{\nu}/\sigma)\frac{\partial}{\partial x}\sqrt{\rho}\tilde{\nu}\end{pmatrix} \tag{3.3}$$

Similar expressions are found for the components of G. The preceding can be adapted for a general $\xi-\eta$ curvilinear coordinate system by applying a simple transformation from Cartesian $x-y$ space

$$\begin{aligned}\frac{\partial}{\partial x}&=\frac{\partial\xi}{\partial x}\frac{\partial}{\partial\xi}+\frac{\partial\eta}{\partial x}\frac{\partial}{\partial\eta}\\ \frac{\partial}{\partial y}&=\frac{\partial\xi}{\partial y}\frac{\partial}{\partial\xi}+\frac{\partial\eta}{\partial y}\frac{\partial}{\partial\eta}\end{aligned} \tag{3.4}$$

For the remainder of this thesis, we shall refer to fluxes in the transformed coordinate system by F'. Combining equations (3.2) and (3.4) yields the following relationship between the fluxes

$$F' = \frac{\partial \xi}{\partial x} F + \frac{\partial \xi}{\partial y} G \qquad (3.5)$$

so that our set of governing equations expressed in the curvilinear system becomes

$$\frac{\partial U}{\partial t} + \frac{\partial F'}{\partial \xi} + \frac{\partial G'}{\partial \eta} = W \qquad (3.6)$$

The finite volume method is derived by rewriting equation (3.6) in its weak formulation. This is obtained by integrating over a fixed arbitrary control volume Ω in space. The resulting volume integral containing the flux vector is converted via Gauss's divergence theorem to a surface integral over $\partial\Omega$. Thus we obtain the following

$$\frac{\partial \bar{U}}{\partial t} + \frac{1}{V} \int_{\partial\Omega} F' \cdot dS = \bar{W} \qquad (3.7)$$

where V is the total volume, dS is the outward-pointing surface area vector, and $\bar{U}$ and $\bar{W}$ are volume-averaged over Ω. Thus by discretizing our domain into a set of sub-volumes, the problem may be expressed simply as a sum of the fluxes over the faces of the computational cells. In this scheme, the state of the gas is represented by cell-centered data and face-centered quantities are reconstructed by interpolation. In discrete form, equation (3.7) evaluated at a quadrilateral cell i, j may be written as

$$\frac{\partial \bar{U}_{ij}}{\partial t} = -\frac{1}{V_{ij}} \left[F'_{i+\frac{1}{2}j} S_{i+\frac{1}{2}j} - F'_{i-\frac{1}{2}j} S_{i-\frac{1}{2}j} + G'_{ij+\frac{1}{2}} S_{ij+\frac{1}{2}} - G'_{ij-\frac{1}{2}} S_{ij-\frac{1}{2}} \right] + \bar{W}_{ij} \qquad (3.8)$$

The ±1/2 indices indicate that quantities are evaluated at the face. Extension of the discretized form to three dimensions is trivial and results in an analogous expression. Additionally, equation (3.8) has been written assuming a structured, Cartesian computational domain but it is easily adapted to unstructured meshes of arbitrary cell shapes by simply replacing indices with corresponding cell and face numbers.

The flux evaluation methods used in this work have been extensively detailed elsewhere [see, for instance, Wright (1997)], however subsequent discussions will be facilitated by reviewing them briefly here. As noted previously, the fluxes may be decomposed into convective and diffusive parts in order to take advantage of their different character. The diffusive terms are elliptic in nature and so one may compute fluxes with simple central difference schemes. On the other hand, the inviscid terms are nonlinear and make the system of equations hyperbolic. For this, we apply a more sophisticated upwind-biased method which makes use of the fact that information is propagating along characteristic directions.

3.2.1 Convective Fluxes

We compute the convective fluxes using a modified form of Steger and Warming (1981) flux-vector splitting, which forms the required derivatives along the defined characteristic directions of the flow. This approach, as well as others of similar construction, are commonly referred to as upwind-biased schemes. The purpose of these schemes is to provide numerical stability in the presence of mixed (both positive and negative) characteristic speeds (i.e., eigenvalues) associated with the spatial flux terms of the governing equations. One may also consider an alternative class of schemes where the fluxes are reconstructed symmetrically without regard for flow characteristics. These schemes are stable in subsonic regions of the flow but require the addition of artificial dissipation to maintain stability near strong shock waves. Ultimately, both upwind-biasing and symmetric schemes with artificial dissipation are successful as shock-capturing techniques for the very same reason: numerical instabilities arising from the presence of strong discontinuities are damped out by numerical dissipation. Subbareddy (2007) demonstrates that Steger-Warming fluxes can be written in an equivalent symmetric-plus-dissipative form where the dissipation tensor is simply a well-defined function of the inviscid flux Jacobians and state vector. This is a very useful observation because it allows one to construct schemes in which numerical dissipation is controlled according to the local flow state, thus assuring that only a necessary amount is applied and diffusive errors are minimized. A brief presentation of these ideas and their relevance to this work is provided in the Numerical Considerations section.

To begin, let us first state the homogeneous property of the inviscid fluxes; that is

$$F_I'(\lambda U) = \lambda F_I'(U)$$

where λ is an arbitrary scalar. That the inviscid fluxes are homogeneous of degree one (i.e., linear) is easily verified by inspection of the inviscid flux vectors F_I' presented in the previous section. This allows us to express the flux exactly in a linearized form as a product of its Jacobian and the state vector

$$F_I' = \frac{\partial F_I'}{\partial U} U = A' U \tag{3.9}$$

By definition, flux-vector splitting methods seek to separate the inviscid flux vector into subvectors, each of which has an associated set of eigenvalues. The choice of subvectors is not unique but for our purposes the most useful is to split the flux into left and right moving characteristic components which can be stably computed using an upwind scheme. This is accomplished by noting that our system of m equations is hyperbolic and therefore, by definition, the flux Jacobian is diagonalizable with real eigenvalues λ_m

$$R^{-1} A' R = \Lambda = \begin{pmatrix} \lambda_1 & & & 0 \\ & \lambda_2 & & \\ & & \ddots & \\ 0 & & & \lambda_m \end{pmatrix} \tag{3.10}$$

The split-flux Jacobians are expressed in terms of the negative and positive elements of Λ. One possible splitting is to write

$$\Lambda^{\pm} = \frac{\Lambda \pm |\Lambda|}{2} \qquad \text{such that} \qquad \Lambda = \Lambda^- + \Lambda^+$$

Then by combining (3.9) and (3.10) we obtain

$$\begin{aligned} F_I' =& A'U = R\left(\Lambda^- + \Lambda^+\right) R^{-1} U \\ =& F_I'^- + F_I'^+ \end{aligned} \tag{3.11}$$

In practice, to facilitate the diagonalization of A', a variable transformation is introduced. The choice of variables is not unique, but for convenience we use the vector of primitives

$$V = (\rho_1, \ldots, \rho_{\text{ns}}, u, v, e_v, p, \tilde{\nu})^T$$

The Jacobian is then broken down into components via a similarity transformation. If we let $S^{-1} = \frac{\partial U}{\partial V}$, then the Jacobian may be written as

$$A' = \frac{\partial U}{\partial V} \frac{\partial V}{\partial U} \frac{\partial F_I'}{\partial V} \frac{\partial V}{\partial U} = S^{-1} \tilde{A}' S$$

where, by a property of similarity transformations,

$$\tilde{A}' = C_{\tilde{A}'}^{-1} \Lambda C_{\tilde{A}'}$$

The columns of $C_{\tilde{A}'}^{-1}$ are the eigenvectors of $\tilde{A}'$ and Λ has been previously defined. Putting this together with (3.11) results in the following expressions for the split fluxes

$$\begin{aligned} F_I'^- &= S^{-1} C_{\tilde{A}'}^{-1} \Lambda^- C_{\tilde{A}'} S U = A'^- U \\ F_I'^+ &= S^{-1} C_{\tilde{A}'}^{-1} \Lambda^+ C_{\tilde{A}'} S U = A'^+ U \end{aligned} \tag{3.12}$$

In their original formulation, Steger and Warming suggested that both $A'^{\pm}$ and U be evaluated using upwind cell center data. MacCormack and Candler (1989) proposed that the Jacobian instead be evaluated at the cell face, which reduces the numerical dissipation of the method but may not be sufficient to capture strong gradients. In this work, we use a pressure weighted average of adjacent cells to evaluate the Jacobian so that the model smoothly transitions between modified and true Steger-Warming in regions of large pressure gradients. It should also be noted that the original method is only first order accurate spatially. Higher order schemes can be constructed by extrapolating cell data to the face. We refer to the left and right extrapolated states as U^L and U^R respectively. Thus the split fluxes at a cell face are evaluated as

$$\begin{aligned} F_{I_{i+\frac{1}{2}}}'^- &= A'^-(\widetilde{U}_{i+\frac{1}{2}}) \cdot U_{i+\frac{1}{2}}^R \\ F_{I_{i+\frac{1}{2}}}'^+ &= A'^+(\widetilde{U}_{i+\frac{1}{2}}) \cdot U_{i+\frac{1}{2}}^L \end{aligned} \tag{3.13}$$

The notation $\widetilde{U}$ is to distinguish between the averaging used to evaluate $A'^{\pm}$ and the higher order extrapolations used to obtain U^L and U^R. By combination of (3.8), (3.11), and (3.13) we obtain the upwind finite volume formulation of the inviscid equations

$$
\begin{aligned}
\frac{\partial \bar{U}_{ij}}{\partial t} = -\frac{1}{V_{ij}} \Bigg[& \left(A'^{+}_{i+\frac{1}{2}j} S_{i+\frac{1}{2}j} U^{L}_{i+\frac{1}{2}j} - A'^{+}_{i-\frac{1}{2}j} S_{i-\frac{1}{2}j} U^{L}_{i-\frac{1}{2}j} \right) \\
& - \left(A'^{-}_{i-\frac{1}{2}j} S_{i-\frac{1}{2}j} U^{R}_{i-\frac{1}{2}j} - A'^{-}_{i+\frac{1}{2}j} S_{i+\frac{1}{2}j} U^{R}_{i+\frac{1}{2}j} \right) \\
& + \left(B'^{+}_{ij+\frac{1}{2}} S_{ij+\frac{1}{2}} U^{L}_{ij+\frac{1}{2}} - B'^{+}_{ij-\frac{1}{2}} S_{ij-\frac{1}{2}} U^{L}_{ij-\frac{1}{2}} \right) \\
& - \left(B'^{-}_{ij-\frac{1}{2}} S_{ij-\frac{1}{2}} U^{R}_{ij-\frac{1}{2}} - B'^{-}_{ij+\frac{1}{2}} S_{ij+\frac{1}{2}} U^{R}_{ij+\frac{1}{2}} \right) \Bigg] + \bar{W}_{ij}
\end{aligned}
\tag{3.14}
$$

3.2.2 Viscous Fluxes

The viscous fluxes are elliptic in nature which makes them suitable for evaluation by a symmetric difference scheme. The viscous flux vector of (3.3) is evaluated at the face using central differencing for the gradient terms. The resulting flux integrated over the face has the form

$$F'_{V_\mathrm{f}} S_\mathrm{f}$$

The viscous flux contribution is summed over each face in the same manner as the inviscid fluxes and added to the right-hand side of equation (3.14).

3.2.3 Time Advancement

The temporal derivative on the left-hand side of equation (3.14) must now be discretized in some manner in order to march the solution in time. The simplest discretization that we can employ is forward Euler differencing

$$\frac{\partial U^n_{ij}}{\partial t} \simeq \frac{U^{n+1}_{ij} - U^n_{ij}}{\Delta t} = \frac{\Delta U^n_{ij}}{\Delta t} \tag{3.15}$$

where the overbars indicating volume-averaged quantities have been dropped for clarity. With this expression we can now rewrite the upwind formulation of the inviscid problem as

$$\begin{aligned}\Delta U_{ij}^{n} = -\frac{\Delta t}{V_{ij}}\Bigg[&\left(A'^{+}_{i+\frac{1}{2}j} S_{i+\frac{1}{2}j} U^{L}_{i+\frac{1}{2}j} - A'^{+}_{i-\frac{1}{2}j} S_{i-\frac{1}{2}j} U^{L}_{i-\frac{1}{2}j}\right) \\ &- \left(A'^{-}_{i-\frac{1}{2}j} S_{i-\frac{1}{2}j} U^{R}_{i-\frac{1}{2}j} - A'^{-}_{i+\frac{1}{2}j} S_{i+\frac{1}{2}j} U^{R}_{i+\frac{1}{2}j}\right) \\ &+ \left(B'^{+}_{ij+\frac{1}{2}} S_{ij+\frac{1}{2}} U^{L}_{ij+\frac{1}{2}} - B'^{+}_{ij-\frac{1}{2}} S_{ij-\frac{1}{2}} U^{L}_{ij-\frac{1}{2}}\right) \\ &- \left(B'^{-}_{ij-\frac{1}{2}} S_{ij-\frac{1}{2}} U^{R}_{ij-\frac{1}{2}} - B'^{-}_{ij+\frac{1}{2}} S_{ij+\frac{1}{2}} U^{R}_{ij+\frac{1}{2}}\right)\Bigg]^{n} + \Delta t W_{ij}^{n} \qquad (3.16)\end{aligned}$$

Equation (3.16) defines an explicit time integration scheme with first order accuracy. ΔU_{ij}^{n} is the explicit residual and represents the change in the state vector from time level n to $n+1$. Thus, after computing (3.16), we obtain the solution at time level $n+1$ from

$$U_{ij}^{n+1} = U_{ij}^{n} + \Delta U_{ij}^{n} \qquad (3.17)$$

The numerical stability of explicit methods imposes a maximum stable time step, which is generally much smaller than the required simulation time. By evaluating the right-hand side of (3.16) at the $n+1$ time level, we can make the method implicit and thus greatly improve its stability at larger time steps. In order to obtain the fluxes and source terms at $n+1$, we linearize them about the n-th time level

$$\begin{aligned} F_I'^{n+1} \simeq & F_I'^{n} + \left(\frac{\partial F_I'}{\partial U}\right)^{n} \left(U^{n+1} - U^{n}\right) \\ \simeq & F_I'^{n} + A'^{n} \delta U^{n} \\ W^{n+1} \simeq & W^{n} + C^{n} \delta U^{n} \qquad (3.18)\end{aligned}$$

where C^n is the source term Jacobian and we have defined $\delta U^n = U^{n+1} - U^n$. The implicit form of the viscous fluxes is given by the linearization

$$F_V'^{n+1} = F_V'^{n} + \delta F_V'^{n}$$

where it remains to find a suitable expression for $\delta F_V'^{n}$. We note that the original expression for F_V' in (3.3) is functionally dependent on the state U and spatial derivatives of non-conserved variables. Thus we may express the implicit viscous flux as

$$\begin{aligned} F_V'^{n+1} =& F_V'^n + M_\xi \frac{\partial}{\partial \xi} \left(\delta \mathbf{V}\right)^n \\ =& F_V'^n + M_\xi \frac{\partial}{\partial \xi} \left(N \delta U\right)^n \end{aligned} \tag{3.19}$$

where we have introduced for convenience the vector of non-conserved variables

$$\mathbf{V} = \left(c_1, \ldots, c_{\mathrm{ns}}, u, v, e_v, T\right)^T$$

and $N = \frac{\partial \mathbf{V}}{\partial U}$ is the transformation between $\mathbf{V}$ and U. In equation (3.19), $\delta F_V'^n$ is evaluated by applying the thin-layer assumption to the derivative whereby only the component in the direction of the flux is retained. A similar process is applied in each direction so, for example, the approximation to $\delta G_V'^n$ is expressed in terms of derivatives with respect to η only. Note however that this approximation applies only to the *implicit* treatment of the diffusive fluxes; all derivatives are retained in the explicit fluxes and thus contribute to the physical solution. Expressions for the matrices M_ξ and M_η may be found in Nompelis (2004).

Applying the linearizations to our upwind formulation of the inviscid problem (3.14) and incorporating the viscous terms yields the following first order implicit equation

$$\begin{aligned} \delta U_{ij}^n + \frac{\Delta t}{V_{ij}} \Bigg[& \left(\tilde{A}^+_{i+\frac{1}{2}j} S_{i+\frac{1}{2}j} \delta U_{ij} - \tilde{A}^+_{i-\frac{1}{2}j} S_{i-\frac{1}{2}j} \delta U_{i-1j} \right) \\ & - \left(\tilde{A}^-_{i-\frac{1}{2}j} S_{i-\frac{1}{2}j} \delta U_{ij} - \tilde{A}^-_{i+\frac{1}{2}j} S_{i+\frac{1}{2}j} \delta U_{i+1j} \right) \Bigg]^n - \Delta t C_{ij}^n \delta U_{ij}^n = \Delta U_{ij}^n \end{aligned} \tag{3.20}$$

where we have dropped the η-direction fluxes for simplicity. $\tilde{A}$ has been defined to include both inviscid and viscous flux contributions such that

$$\tilde{A}^+ = A'^+ - M_\xi N \qquad \tilde{A}^- = A'^- + M_\xi N$$

In principle, we can solve equation (3.20) directly for δU_{ij}^n by forming and inverting a large block banded matrix. A direct inversion, however, would be too expensive numerically for most problems of interest. [Note: there also exist software packages which rely on Krylov subspace methods to solve the fully coupled problem in an iterative manner but they were not investigated during the course of this work.] In Wright (1997), several alternative approaches based on relaxation of the off-diagonal terms are examined which make the problem efficiently parallelizable in addition to providing robust solution convergence for high Reynolds number viscous problems. In this work, we make use of a hybridized version of the Full-Matrix Data-Parallel (FMDP) and Data-Parallel Line Relaxation (DPLR) methods. The details of the individual relaxation methods may be found in Wright et al. (1996, 1997, 1998). We defer to Nompelis et al. (2005) for a discussion of the coupling procedure.

3.3 Detached Eddy Simulation

The wake of many reentry configurations can be expected to be unsteady, characterized by a large number of vortices of various sizes shed from the base. Conventional aerothermal analysis would model this complex flow using a RANS approach. It is well known that traditional RANS formulations are incapable of accurately capturing the unsteady wake dynamics owing to the excessive amount of dissipation generated by them which tends to damp out all but the largest eddies. Alternative models must therefore be considered since a simulation's ability to accurately predict base heating rates will be determined by its ability to capture the effects of unsteady flow.

While DNS and LES are still the benchmarks for high-fidelity unsteady simulations, the associated computational costs make them impractical for use in flows such as that considered here. On the other hand, hybrid RANS/LES methods offer a relatively affordable combination of practicality and fidelity. In this paper, we consider the DES methodology advanced by Spalart et al. (1997). This method has been used extensively by a number of researchers over the past decade on a wide range of problems. It has proven to be quite robust and capable of accurately predicting separated flows. To the authors knowledge, however, it has not been thoroughly tested at hypersonic conditions in which aerothermal heating is a primary concern. For completeness, we present a brief overview of DES.

Let us consider the S-A RANS model presented in Section 2.4 and discuss how it functions in a separated flow. Recall the form of the model from equation (2.5)

$$\frac{D\rho\tilde{\nu}}{Dt} = \frac{1}{\sigma}\left[\nabla\cdot(\mu\nabla\tilde{\nu} + \sqrt{\rho}\tilde{\nu}\nabla\sqrt{\rho}\tilde{\nu}) + c_{b2}(\nabla\sqrt{\rho}\tilde{\nu})^2\right] + c_{b1}\rho\tilde{S}\tilde{\nu} - c_{w1}f_w\rho\left(\frac{\tilde{\nu}}{d}\right)^2$$

Note that the destruction term depends on the inverse distance to the nearest solid surface. Therefore when the model is used far from solid surfaces, there is very little destruction of turbulent viscosity, and high levels of $\tilde{\nu}$ persist. This is what causes the RANS approach to overpredict the turbulent dissipation levels in separated flow regions.

The DES solution of this problem is to replace the length scale of the model with a new one, such that the model behaves as a Smagorinsky-like subgrid scale model in regions where the flow is separated. Thus the new length scale should act as a filter, allowing the simulation to resolve eddies down to the grid scale while modeling those that are smaller. For the particular case of the S-A model, this is accomplished in a straightforward manner by replacing d with a new variable that depends on some measure of the local grid cell size

$$\tilde{d} = \min\left(d, C_{DES}\Delta\right) \tag{3.21}$$

With this definition, the modified equation is equivalent to the unchanged S-A RANS model near walls. Away from walls, if the filter width (i.e. cell size) is chosen to lie in the inertial subrange, then turbulent production and destruction should roughly balance each other. Under this assumption, it is easy to show that the S-A model reduces to the familiar Smagorinsky form

$$\begin{aligned} \tilde{\nu} &= \frac{c_{b1}}{c_{w1}f_w}\left(C_{DES}\Delta\right)^2\tilde{S} && \text{(S-A DES)} \\ \nu_t &= \left(C_s\Delta\right)^2\overline{S} && \text{(Smagorinsky)} \end{aligned}$$

C_{DES} is an adjustable parameter, conventionally set to 0.65, determined by Shur et al. (1999) using simulations of homogeneous turbulence. It should be noted that the DES approach is not limited to the S-A model, but has been extended to other popular two-equation formulations as well [see Strelets (2001)].

3.4 Numerical Considerations

There are several aspects of unsteady simulations in general and of the methods outlined above in particular which impact our ability to obtain a correct solution to the problem of interest. The most fundamental aspect is to determine the metric by which correctness is measured. For instance, a particular case may require a detailed account of the temporal evolution of a flow, while for another it may suffice to compute a flow that is only statistically similar. It is clear, however, that practices which promote improved solution accuracy will generally be preferred. We now present a brief discussion of the most important numerical considerations pertaining to this work.

3.4.1 Unstructured Mesh Design

The numerical methods presented up to this point have been incorporated into a code called US3D, developed at the University of Minnesota. Development of the code is documented by Nompelis et al. (2004, 2005). The code is designed to use unstructured grids, meaning that there is no assumed order to how discrete cell volumes and nodes are connected to each other. Rather, all information required for constructing and solving the systems outlined above is determined beforehand in a pre-processing step and read into the code. The code supports an arbitrary mix of tetrahedra, prisms, pyramids, and hexahedra in the domain discretization. With such a degree of generality, one issue that immediately arises is how to best construct the lines used for the DPLR method. Currently, US3D restricts line construction to hexahedra and prisms stacked outward from the wall. This is done for two reasons. First, stacks of these cell types are somewhat less ambiguous than other types in the sense that each face of the cell has a clearly defined opposing face. This ensures that solution lines are regularly aligned normal to the body and adjacent to each other. Secondly, the primary benefit of the DPLR method is in high Reynolds number wall-bounded flows where high-aspect-ratio cells are required to resolve near-wall gradients. This is due to the strong coupling of the flow in the direction of the wall-normal gradients, a feature that is mimicked numerically by line relaxation. In a separated, unsteady flow, however, this feature is undesirable because it incorrectly assumes directional flow coupling where there is none. Thus it is possible to impart bias into the solution.

Another commonly encountered problem in aerothermal applications is the influence of highly skewed cells on error generation. This issue has been documented by Gnoffo (2004) and Candler (2007) amongst others. Misalignment of the mesh near shock waves results in the production of large errors. Due to the weak transverse gradients and low convection speed, the errors become trapped along the stagnation streamline and can dominate the flow, potentially leading to an aphysical solution. Traditionally, we use eigenvalue limiters to address this problem, however the solution is sensitive to them, especially in boundary layers, and care must be taken in their application. With tetrahedra and pyramids, there is no possibility of exact alignment and so error generation is unavoidable. A similar issue arises when these non-uniform elements are used in the boundary layer where quantities like heat flux and shear are highly dependent upon the gradients being correctly resolved. These two observations, along with the limitations imposed on line construction, have led us to conclude that fully hexahedral meshes are the best candidates for accurate aerothermal simulations. In our experience, it is feasible to carefully construct high-quality grids of moderately complex geometries entirely with hexahedra. This is because the unstructured nature of the code obviates the need for grid blocks and we can employ extensive use of grid singularities and other complex topological structures. Tetrahedra, prisms, and pyramids are best reserved for facilitating the connections between large hexahedral blocks, if necessary, or if the geometry is simply so complex that alternatives are impracticable.

Of clearer concern is that the turbulence model depends explicitly on the grid spacing when used in DES mode. Care must therefore be taken in the generation of the mesh to ensure appropriate behavior. Spalart (2001) laid out guidelines for identifying regions of the flow and applying rules of thumb for generating a good grid. The primary concerns are to ensure that the switch from RANS to LES mode occurs outside of the boundary layer and to sufficiently resolve the wake such that the filter is operating appropriately. It is typically unknown beforehand what grid spacing is needed for this to occur and therefore a prudent study will always include a grid resolution analysis. While true grid convergence does not apply to turbulent flows, we can find convergence in a statistical sense by looking at mean flow and spectral quantities. More recent versions of the DES method have been proposed [Spalart (2006a, 2006b)] which seek to remove the RANS/LES switch dependence.

These have not been investigated in the current study.

Finally, there is the flow structure itself to consider. A typical aerothermal application may have any number of flow features present, including shocks, shear layers, and their many possible interactions. On the forebody, the grid must be shock-aligned for reasons noted above. The main concerns in the base region are to properly capture the primary shear layers developing off the vehicle afterbody and to adequately resolve the near wake. The development of the shear layers will largely determine the shape and extent of the recirculating region, which in turn drives the pressure and heating profiles on the base. In order to resolve the shear layers, the grid topology must be aligned and clustered to them as much as possible. The wake, however, is resolved most efficiently when the grid points are uniformly distributed. In each case presented here, various mesh topologies were explored until a suitable one was found to balance shear layer resolution and grid point distribution. The particular mesh designs used for our problems of interest will be discussed in further detail in their respective sections.

3.4.2 Evaluation of Gradients

Gradients of primitive variables are used in the computation of both the inviscid and viscous fluxes. Furthermore, the S-A turbulence model's production term is a function of vorticity. In both instances, correctly estimating flow gradients in order to maintain solution accuracy is a paramount concern. A typical structured finite volume code based on hexahedral elements computes gradients using knowledge of the local cell metrics. This may also be done in an unstructured code so long as the elements remain hexahedral. For a general mesh constructed of arbitrary polyhedra, however, different methods must be applied.

Several approaches for computing gradients on arbitrary polyhedral meshes can be found in the literature. One very popular method is to apply the divergence theorem at each cell from which the gradient can be derived explicitly. However, experience has shown this method to be prone to errors, especially for high aspect ratio or highly skewed cells. In this work, we use a weighted least-squares approach for gradient reconstruction. An excellent discussion of the procedure can be found in Mavriplis (2003). In this section, we summarize Mavriplis' presentation for the three-dimensional case.

The objective of weighted least-squares is to minimize the following expression

$$\sum_{k=1}^{N} w_{ik}^2 E_{ik}^2 \tag{3.22}$$

where N is the number of neighbors used in the reconstruction stencil and the error associated with computing the gradient at cell i is given by

$$E_{ik}^2 = \left(-du_{ik} + \nabla u_i \cdot d\vec{x}_{ik}\right)^2$$

In these expressions, du_{ik} is the difference $u_k - u_i$ of the quantity of interest, $d\vec{x}_{ik}$ is the relative position vector between points i and k, and w_{ik} is a weighting factor. Equation (3.22) is minimized by solving

$$\frac{\partial}{\partial u_x}\left(\sum w_{ik}^2 E_{ik}^2\right) = \frac{\partial}{\partial u_y}\left(\sum w_{ik}^2 E_{ik}^2\right) = \frac{\partial}{\partial u_z}\left(\sum w_{ik}^2 E_{ik}^2\right) = 0$$

which produces a system of equations of the following form

$$\begin{pmatrix} a_i & b_i & c_i \\ b_i & d_i & e_i \\ c_i & e_i & f_i \end{pmatrix} \begin{pmatrix} u_x \\ u_y \\ u_z \end{pmatrix} = \begin{pmatrix} p_i \\ q_i \\ r_i \end{pmatrix} \tag{3.23}$$

The elements of this system are given by

$$\begin{aligned} a_i &= \sum w_{ik}^2 dx_{ik}^2 & b_i &= \sum w_{ik}^2 dx_{ik} dy_{ik} & c_i &= \sum w_{ik}^2 dx_{ik} dz_{ik} \\ d_i &= \sum w_{ik}^2 dy_{ik}^2 & e_i &= \sum w_{ik}^2 dy_{ik} dz_{ik} & f_i &= \sum w_{ik}^2 dz_{ik}^2 \\ p_i &= \sum w_{ik}^2 du_{ik} dx_{ik} & q_i &= \sum w_{ik}^2 du_{ik} dy_{ik} & r_i &= \sum w_{ik}^2 du_{ik} dz_{ik} \end{aligned}$$

where the sums are taken from $k = 1$ to N over the stencil neighbors. The left-hand side of (3.23) is a function of the grid metrics only and can be pre-computed and stored for problems in which the mesh is static. Appropriate weighting functions are left for the user to determine; in this work, an inverse distance weighting is applied so that

$$w_{ik}^2 = \frac{1}{\|d\vec{x}_{ik}\|^2}$$

3.4.3 Low-Dissipation Fluxes

Because numerical dissipation acts to damp out small scale unsteady fluid motion, it is sensible (and more correct physically) to employ dissipation-free schemes for evaluation of the inviscid fluxes. On the other hand, dissipation is necessary to ensure stable behavior in the vicinity of strong discontinuities. In this section, we review some observations and suggestions by Subbareddy (2007) for minimizing the impact of dissipation generated by our shock-capturing scheme. As a general rule, what follows has not been applied to the present work except for a single case discussed in Chapter 6. It is included here primarily to illustrate the modeling considerations which arise for the problems of interest.

First we note that numerically dissipation-free fluxes are associated with symmetric (or central difference) schemes. Recalling equation (3.11), the modified Steger-Warming flux across the $\mathrm{f} = i + \frac{1}{2}$ face is given by

$$\begin{aligned} F'_{I_\mathrm{f}} &= F'^{-}_{I_\mathrm{f}} + F'^{+}_{I_\mathrm{f}} \\ &= \left(S^{-1}C^{-1}\Lambda^{-}CS\right)_\mathrm{f} \cdot U^R_\mathrm{f} + \left(S^{-1}C^{-1}\Lambda^{+}CS\right)_\mathrm{f} \cdot U^L_\mathrm{f} \\ &= \left(S^{-1}C^{-1}\frac{\Lambda - |\Lambda|}{2}CS\right)_\mathrm{f} \cdot U^R_\mathrm{f} + \left(S^{-1}C^{-1}\frac{\Lambda + |\Lambda|}{2}CS\right)_\mathrm{f} \cdot U^L_\mathrm{f} \\ &= \left(S^{-1}C^{-1}\Lambda CS\right)_\mathrm{f} \cdot \frac{U^L_\mathrm{f} + U^R_\mathrm{f}}{2} - \frac{1}{2}\left(S^{-1}C^{-1}|\Lambda|CS\right)_\mathrm{f} \cdot \left(U^R_\mathrm{f} - U^L_\mathrm{f}\right) \\ &= F'_I\left(\frac{U^L_\mathrm{f} + U^R_\mathrm{f}}{2}\right) + D \end{aligned} \tag{3.24}$$

Thus, with some algebra, we've recast the original upwind formulation as a sum of the original inviscid flux (evaluated symmetrically) and a dissipation term. Another perspective is gained if one considers this as a special case of an artificial dissipation scheme. Embracing this approach, we can conceive an alternative class of schemes in which the 'symmetric' and 'dissipative' contributions are computed separately and in a manner which minimizes the errors due to dissipation and spectral aliasing.

As an example, we can take advantage of the fact that various discrete forms of the nonlinear inviscid flux (corresponding to the 'symmetric' flux above) have different spectral aliasing properties. Consider the following forms of the incompressible convective terms

$$
\begin{aligned}
&u_j \frac{\partial u_i}{\partial x_j} && \textbf{convective} \\
&\frac{\partial}{\partial x_j}\left(u_i u_j\right) && \textbf{divergence} \\
&\frac{1}{2}\left[u_j \frac{\partial u_i}{\partial x_j} + \frac{\partial}{\partial x_j}\left(u_i u_j\right)\right] && \textbf{skew-symmetric}
\end{aligned}
$$

Although the above forms are equivalent in a continuous sense, Blaisdell et al. (1996) used Fourier analysis to demonstrate that aliasing errors arising from the discrete equations are greatly reduced when the nonlinear term is expressed in the skew-symmetric form.

Similarly, we can address the amount of dissipation by simply introducing a factor α to pre-multiply the dissipative term

$$F'_{I_\mathrm{f}} = F'_{\mathrm{sym}} + \alpha D$$

The factor should vary smoothly over the interval $0 \leq \alpha \leq 1$ and ideally be a function of the local flow state so that it can function without input from the user. One such possibility is suggested by Ducros et al. (1999)

$$\alpha = \frac{\left(\nabla \cdot \vec{u}\right)^2}{\left(\nabla \cdot \vec{u}\right)^2 + \|\vec{\omega}\|^2}$$

Near shock waves, this expression will have a value close to unity and the dissipation term will be fully applied to stabilize the scheme. In turbulent regions where the vorticity magnitude is large and numerical dissipation is not desired, the switch naturally takes on a value close to zero.

The preceding is a greatly simplified presentation. Much more sophisticated formulations can be devised which address spurious generation of entropy and kinetic energy from the approximation to the convective flux. These matters are beyond the scope of this thesis and the interested reader is strongly encouraged to read Subbareddy (2007) and Subbareddy and Candler (2009) for detailed discussions.

3.4.4 Time Accuracy

As derived previously, the implicit equation given by (3.20) is first-order accurate in time. For flows in which time accuracy is critical, one must be aware that the improved stability afforded by an implicit scheme can potentially lead to unacceptably large temporal discretization errors.

To address this concern, we have adopted the approach of limiting the time step so that it does not exceed the convective time scales associated with the propagation of information across cells located in turbulent flow regions. Thus we have the constraint

$$\Delta t \leq \frac{\Delta x}{\|u+a\|_{\max}}$$

Note that the time step is still applied globally; this expression is merely used as a guideline for selecting an appropriate CFL number. In practice, the maximum stable time step is often reached in simulations of unsteady, hypersonic flows before the above condition is exceeded although on certain meshes this is not universally the case.

Alternatively, we can seek to reduce the errors associated with the discretization itself by employing a higher-order method. We can do this implicitly using a dual-time method [see, for instance, Rumsey et al. (1996)]. Dual-time methods work by breaking down an unsteady problem into a series of steady-state problems. As with the previous section, we stress here that what follows has not been used in subsequent analyses with the sole exception of Chapter 6. However, in this section we present results of a simple analytical problem for illustrative purposes.

Consider the first-order method outlined earlier. The method was developed by discretizing

$$\frac{\partial U}{\partial t} + R = 0$$

where R is invoked to simplify notation and encompasses all spatial derivatives and source terms. The resulting system of equations to be solved (3.20) was

$$\left[\frac{V_{ij}}{\Delta t} I + \left(\tilde{A}^{+}_{i+\frac{1}{2}j} S_{i+\frac{1}{2}j} - \tilde{A}^{-}_{i-\frac{1}{2}j} S_{i-\frac{1}{2}j}\right) - V_{ij} C_{ij}\right]^{n} \delta U^{n}_{ij} =$$
$$\frac{V_{ij}}{\Delta t} \Delta U^{n}_{ij} + \left(\tilde{A}^{+}_{i-\frac{1}{2}j} S_{i-\frac{1}{2}j} \delta U^{n}_{i-1j} - \tilde{A}^{-}_{i+\frac{1}{2}j} S_{i+\frac{1}{2}j} \delta U^{n}_{i+1j}\right)$$

The dual-time problem solves a modified version of the original equations by introducing a fictitious temporal derivative. The goal is to find a steady-state solution in the fictitious (dual-) time. At steady-state, the dual-time derivative vanishes and we are left with a solution which simultaneously satisfies the original system of equations. The dual-time system can be expressed as

$$\frac{\partial U}{\partial \tau} + \frac{\partial U}{\partial t} + R \quad = \quad \frac{\partial U}{\partial \tau} + \hat{R} \quad = 0$$

Note how the original and dual-time systems are functionally equivalent. This feature allows us to derive a solution procedure which is nearly identical to the original. In principle, we can achieve an arbitrary order of accuracy by using an appropriate discretization of the physical time derivative. For example, a second-order implicit backward discretization yields

$$\frac{\delta U^k}{\Delta \tau} + [\Delta t_n]^{-1} \left[\frac{\tilde{r}+2}{\tilde{r}+1} U^{k+1} - \frac{\tilde{r}+1}{\tilde{r}} U^n + \frac{1}{\tilde{r}(\tilde{r}+1)} U^{n-1} \right] + R = 0$$

where we have defined $\Delta t_n = t_{n+1} - t_n$, $\tilde{r} = \frac{\Delta t_{n-1}}{\Delta t_n}$, and $\delta U^k = U^{k+1} - U^k$. Here, we are using k-superscripts to denote dual-time levels while n-superscripts indicate physical time levels. This example illustrates one of the primary disadvantages of higher-order implicit time integration methods, namely that they require flowfields computed at prior time levels to be stored in memory. Increasing the order of accuracy naturally means increasing the stencil width and therefore the storage penalty. Nevertheless, for most problems of interest second-order accuracy is sufficient and the storage penalty is relatively minor. One should also keep in mind the distinction between *accuracy* and *order of accuracy*. The latter provides insight into the scaling of the truncation error but not its magnitude. As a general observation, it is conceivable [and can readily be demonstrated, see Section 8.5 of Leveque (2002)] that a lower-order method will achieve better solution accuracy than a higher-order method for a given problem.

Returning now to the second-order implicit dual-time equation, and letting $\alpha_1 = \frac{\tilde{r}+2}{\tilde{r}+1}$, $\alpha_2 = \frac{\tilde{r}+1}{\tilde{r}}$, and $\alpha_3 = \frac{1}{\tilde{r}(\tilde{r}+1)}$, we can linearize the U^{k+1} term to yield

$$\delta U^k \left(\frac{1}{\Delta \tau} + \frac{\alpha_1}{\Delta t_n} \right) + [\Delta t_n]^{-1} \left[\alpha_1 U^k - \alpha_2 U^n + \alpha_3 U^{n-1} \right] + R = 0$$

From this, the modified set of equations to solve is

$$\left[\left(\frac{1}{\Delta\tau}+\frac{\alpha_1}{\Delta t_n}\right)V_{ij}I+\left(\tilde{A}^{+}_{i+\frac{1}{2}j}S_{i+\frac{1}{2}j}-\tilde{A}^{-}_{i-\frac{1}{2}j}S_{i-\frac{1}{2}j}\right)-V_{ij}C_{ij}\right]^{k}\delta U^{k}_{ij}=\frac{V_{ij}}{\Delta t_n}\Delta U^{k}_{ij}+$$
$$\left(\tilde{A}^{+}_{i-\frac{1}{2}j}S_{i-\frac{1}{2}j}\delta U^{k}_{i-1j}-\tilde{A}^{-}_{i+\frac{1}{2}j}S_{i+\frac{1}{2}j}\delta U^{k}_{i+1j}\right)-\frac{V_{ij}}{\Delta t_n}\left(\alpha_1U^{k}-\alpha_2U^{n}+\alpha_3U^{n-1}\right)$$

where $\Delta U^{k}_{ij}=U^{k}_{ij}-U^{n}_{ij}$. The new procedure is to integrate the dual-time equation for each physical time step until $\delta U^{k}\rightarrow 0$, at which point $U^{k}=U^{n+1}$. Interestingly, the dual-time step only appears as a modification to the diagonal weighting of the implicit operator. In general, this can be assumed to be infinite without adversely affecting the stability of the dual-time integration and thus its inverse can be neglected from the left-hand side of the equation.

A question arises concerning convergence of the dual-time equation. This is a very important matter because each dual-time subiteration has approximately the same cost as a first-order iteration in physical time. For instance, one may consider imposing some residual tolerance level to determine dual-time convergence. Yet if each time step takes 100 subiterations to achieve convergence then it is unlikely to be more efficient than simply reducing the first-order time step by two orders of magnitude. Fortunately, for reasonable values of CFL, experimentation has shown that 4 or 5 subiterations will typically reach a suitable level of convergence. This is clearly seen in Figure 3.1(a) which shows solutions to Sod's shock tube problem with the second-order scheme. The density profile is cleanly captured by the dual-time scheme and the 4 and 10 subiteration solutions are virtually identical. Furthermore, tests with the first-order scheme revealed that an approximately ten-fold decrease in the time step was required to ensure the same level of accuracy as the second-order scheme for this problem. Thus, we see in Figure 3.1(b) that the total required wall time was reduced by a factor of 2.5 over the first order result.

Ultimately, these results are problem-specific to some degree. In the absence of analytical solutions to the Navier-Stokes equations, it is up to the user to verify time accuracy by performing a temporal resolution study. This is done in much the same way as a spatial grid resolution study: the problem is run with varying time step sizes and the results then compared for 'convergence.' With the dual-time scheme, one may find superior choices for the number of subiterations than

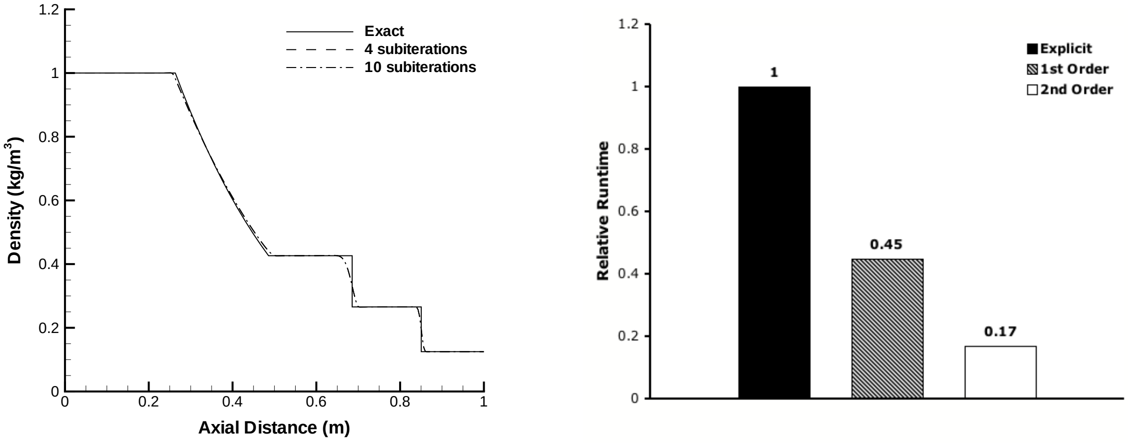

(a) (b)

Figure 3.1: (a) Solution to Sod's shock tube problem using 4 and 10 subiterations; (b) Run times using explicit, 1st-order implicit, and 2nd-order implicit time integration schemes. Times are given relative to the explicit solution.

that recommended above, which adds an extra degree of freedom to the problem. Recent tests on an aeroshell configuration in hypersonic flight suggested the disparity between first- and second-order run times to be smaller than for the simple shock tube problem. Finally, one must also respect the presence of other flow processes, such as chemical reactions, whose time scales may be substantially different than the convective time scales referenced here.

Chapter 4

Mars Science Laboratory Parachute System

4.1 Introduction

The Mars Science Laboratory (MSL), scheduled to launch in 2011, is designed to determine if Mars ever possessed an environment capable of supporting microbial life. The landed mass of the MSL rover vehicle will be 775 kg, approximately double any previous payload landed on Mars. The ballistic coefficient for the MSL aeroshell/payload (2750 kg) combination is sufficiently high that it requires the largest parachute and highest Mach number deployment of any Mars mission. As for all previous Mars missions, MSL will use a disk-gap-band (DGB) parachute. This parachute will have a nominal diameter of approximately 21.5 m and may be deployed at a Mach number of up to 2.2 and dynamic pressure of 750 Pa.

Full-scale flight tests for the Viking missions in the Earth's atmosphere used a 16.1 m DGB parachute deployed at Mach numbers up to 2.13. During previous Mars missions, the Viking parachutes were deployed at $M_\infty = 1.1$ and the parachutes for Mars Pathfinder (MPF) and Mars Exploration Rover (MER) were deployed at $M_\infty = 1.7 - 1.8$. In each of these cases, DGB parachutes have consistently exhibited partial canopy collapse in the band region when operating above Mach 1.5. While partial collapse and flutter are common in supersonic parachute operations and despite a great deal of informed speculation, the cause of these phenomena is not yet known.

Furthermore, the size and deployment conditions of the MSL parachute push it outside the realm of past experience. The purpose of this chapter is to apply the methodology outlined in Chapter 3 to the MSL capsule/parachute system in order to (1) predict the flowfield and pressure distribution for the MSL parachute, (2) determine scale and Mach number dependencies of this phenomenon, and (3) determine the physical process causing the partial collapse in the skirt region.

4.2 Problem Description

The primary concern for qualification of the parachute design is its extended operation at speeds in excess of Mach 1.5. While not yet suitable for the purpose of qualification, the role of computational fluid dynamics in this process is being actively pursued within the MSL program. A series of scaled supersonic wind tunnel tests have been carried out in NASA's Ames 9×7 and Glenn 10×10 facilities for the purpose of validating the ability of CFD to predict large-scale parachute dynamics and performance. The focus of this work will be on the rigid canopy tests conducted in the Ames 9×7 tunnel.

A schematic of the experimental setup for the rigid model is shown in Figure 4.1. The model is a 2.3% scale representation of the MSL vehicle at zero angle of attack. The non-dimensional canopy trailing distance is given in terms of the capsule diameter as $x/d = 10$. Throughout the literature, many different terms exist to describe individual components of the parachute system. In this chapter, we shall refer to the capsule and forebody interchangeably. This can be seen to the left of Figure 4.1 attached to the diamond cross-section capsule sting mount (or blade). The parachute itself is often referred to as a canopy. It is further broken down into its DGB constituents: the disk comprises the bowl-shaped part of the canopy and has a vent hole to permit a desired mass flux in order to reduce stress at deployment; the band constitutes the leading edge of the canopy and is separated from the disk by support struts across the gap which helps further relieve canopy stress. The entire canopy structure is attached to a cylindrical sting arm via four supports surrounding the vent hole. Initial tests with the model were conducted to provide drag measurements, as well as shadowgraph and PIV flow visualization. In this work, we shall consider three separate experimental configurations: capsule only, canopy only, and capsule with canopy. Three operating conditions were selected corresponding to Mach numbers of

1.5, 2.0, and 2.5. The freestream conditions are summarized in Table 4.1.

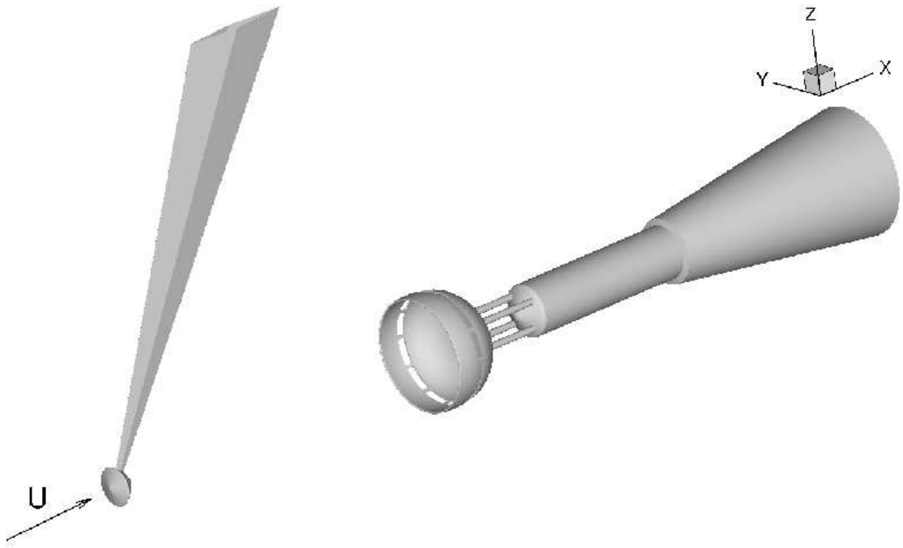

Figure 4.1: Schematic of MSL rigid parachute model in the NASA Ames 9 × 7 wind tunnel. Model is 2.3% scale.

Table 4.1: Freestream conditions used in MSL rigid parachute experiments.

Mach Number	**1.5**	**2.0**	**2.5**	
Re_L	7.4	9.6	12.4	(10^6/m)
ρ_∞	0.2357	0.2131	0.2000	(kg/m^3)
U_∞	436.6	524.4	589.2	(m/s)
T_∞	210.5	171.0	138.2	(K)

The flowfield surrounding the MSL capsule/canopy system is so complex that grid generation quickly becomes the limiting factor to determining how quickly and with what quality one can obtain a solution. The complexity is principally due to (1) the relatively large number of diverse flow features and (2) the broad range of length scales (in these cases, spanning a domain length of 2.65 m down to a viscous wall cell height of 5.0×10^{-6} m). In order to capture this complexity as accurately as possible with a minimum of computational effort, the grids used for this analysis were built up through a series of design steps. This method of grid generation requires that a number of sequential grids be created with a large variation in overall complexity. We begin by generating a relatively simple grid using only the most basic aspects of the geometry, such as the capsule and outer boundaries. The simplified model is simulated and analyzed to determine key flow features such as shock and shear layer positions, and wake structure. Using these results, the mesh is refined to better resolve key features. Once a baseline grid has been established, additional geometric features can be added, such as the capsule support and a simplified parachute model. This procedure is repeated until the highest level of geometry is included. Throughout the process, solutions from one design iteration are interpolated to the next so that startup transients (the time for the flow to reach its natural state) are virtually eliminated. The final grid contains an accurate representation of the entire wind tunnel model, including the capsule, blade, canopy with band support struts, support rods, and sting.

The final grid topology for the MSL system is shown in Figure 4.2. Lines indicate grid block boundaries, however these are ignored during domain decomposition in US3D. The topology takes advantage of the unstructured capability of US3D by incorporating numerous wraps and nested refinements to significantly reduce grid resolution in unimportant regions of the flow. The resulting grid contains 26 million hexahedral cells. Figure 4.3 shows the quality and refinement of the grid in the vicinity of the canopy.

4.3 Numerical Results

4.3.1 Full-Scale Mach Number Dependence

Before tests were begun with the scale model configurations, a series of simulations were run with the purpose of estimating at which flight Mach numbers the parachute design would begin to see performance degradation. This information was then used to guide the development of the experiments themselves. The simulations assume a rigid model of the full-scale MSL parachute in the Martian atmosphere and demonstrate a strong influence of Mach number on parachute performance. Figure 4.4 depicts the drag histories of this configuration for a range of Mach numbers. Time has been non-dimensionalized according the parachute trailing distance and freestream speed. The variation in loading becomes exaggerated as the parachute ap-

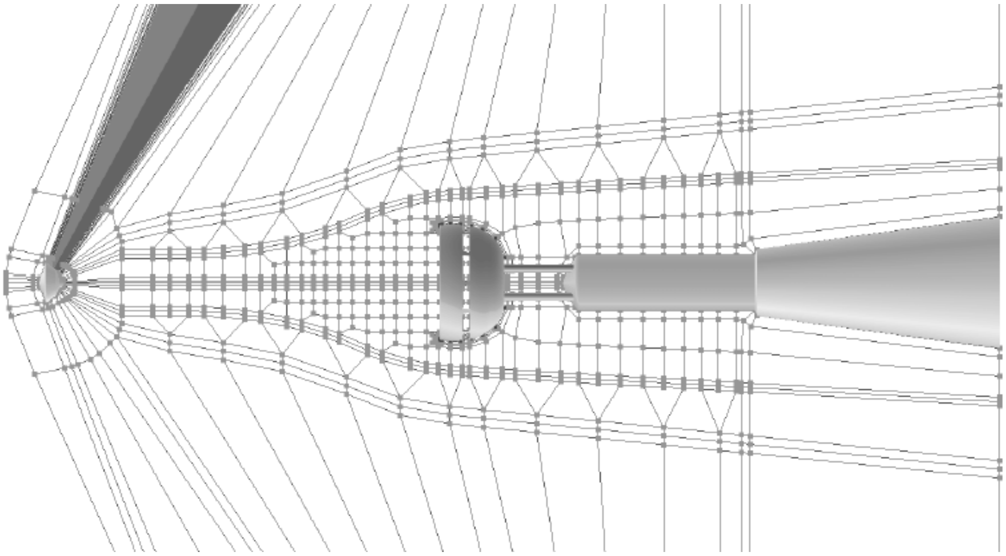

Figure 4.2: Topology used to generate the mesh for MSL capsule/canopy wind tunnel geometry.

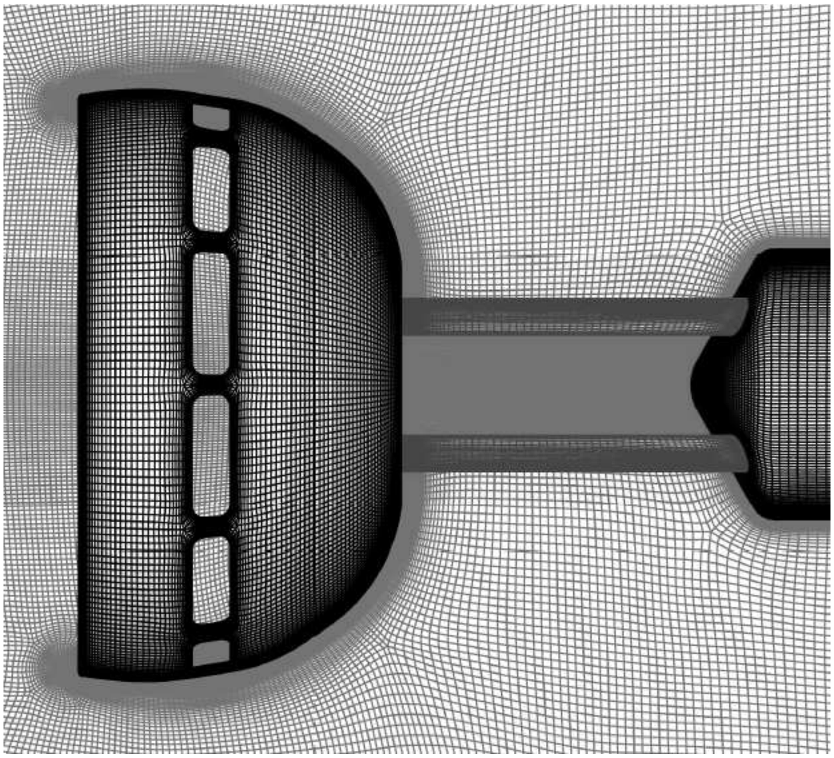

Figure 4.3: Grid detail surrounding canopy, support rods, and sting.

proaches Mach 2, while exhibiting relatively benign behavior both below and above this value. In particular, the simulations show that the most violent drag variations occur at Mach 1.8. We believe this indicates a critical performance Mach number that is a characteristic of the MSL parachute design. A common phenomenological understanding of the problem holds that the critical performance Mach number is a function of several parameters including relative forebody/canopy size, gap width, trailing distance, and the porosity of the parachute fabric. Below this Mach number the canopy is capable of supporting the incoming mass flux such that the wake deficit does not significantly excite any instability due to over-pressurization; above it the wake is sufficiently supersonic that the bow shock experiences less disruption due to the wake.

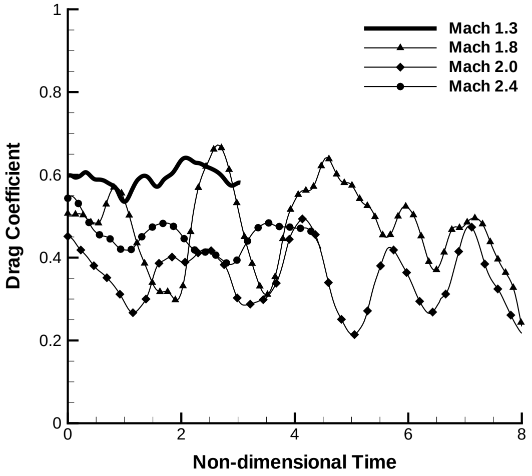

Figure 4.4: Variation in drag on the full-scale MSL parachute system for a range of Mach numbers.

4.3.2 Flow Structure of Wind Tunnel Experiments

The simulated flow structure for the capsule and canopy system is depicted with instantaneous Mach number contours in Figure 4.5. Fluid entering the domain passes through a bow shock surrounding the forebody which renders the flow subsonic. As the flow expands around the body, it becomes supersonic and separates slightly aft of the capsule shoulder. The bow shock impinges the leading edge of the capsule sting which, along with the sting wake, introduces a small asymmetry to the downstream flow as a result. Behind the capsule, a typical wake structure is generated which progresses downstream to the canopy bow shock. The capsule wake structure is characterized by large-scale structures with a helical instability, resulting in an unsteady momentum deficit feeding into the canopy bow shock. This in turn excites an instability in the bow shock which produces the unsteady cycling of pressure within the canopy itself. The dynamics of this process and its impact on canopy inflation will be discussed in more detail in a subsequent section.

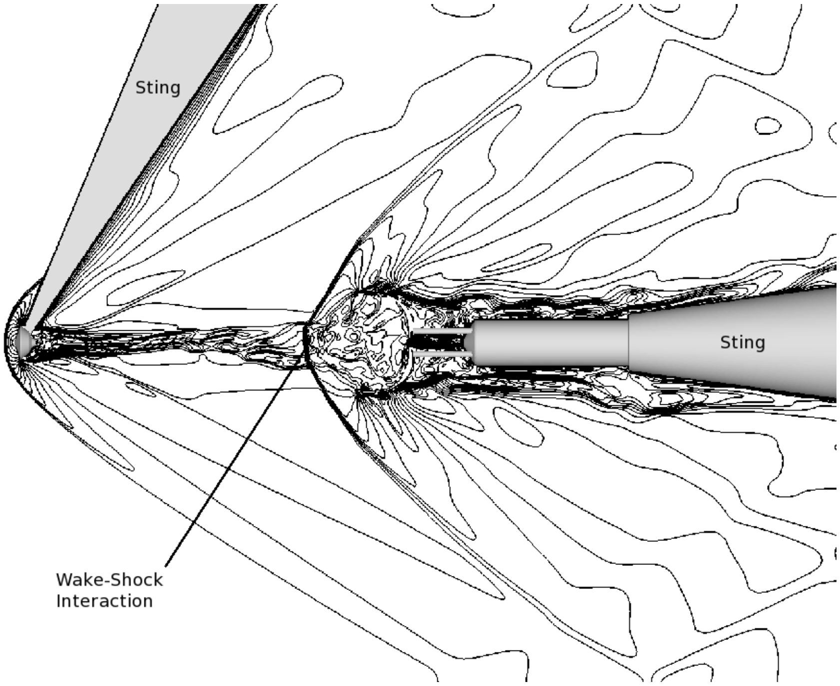

Figure 4.5: Simulated flowfield structure around MSL capsule and canopy configuration depicted with instantaneous Mach number contours.

4.3.3 Capsule-Only Configuration

Initial tests were conducted with a capsule-only configuration for the purpose of investigating the downstream evolution of the wake. PIV measurements were taken at two downstream locations: in the spanwise plane at $x/d = 2$, and in the radial plane at $x/d = 10$. The first location is in the near wake of the capsule while the second coincides with the location of the canopy leading edge.

Figures 4.6 and 4.7 show experimental and simulated velocity contours in the $x/d = 2$ plane at the Mach 2 condition. Note that the visible white lines in the PIV data are artifacts of the post-processing procedure. A qualitative comparison reveals good agreement overall except in the recirculating region directly behind the capsule. This is believed to be due to an inability to properly seed the flow for the PIV process. Nevertheless, the magnitude and shape of contours outside of the recirculating region are reasonably similar. In particular, we see that the shear layer angles match very well and the wake closure (the point at which the separated shear layer recompresses) is captured accurately.

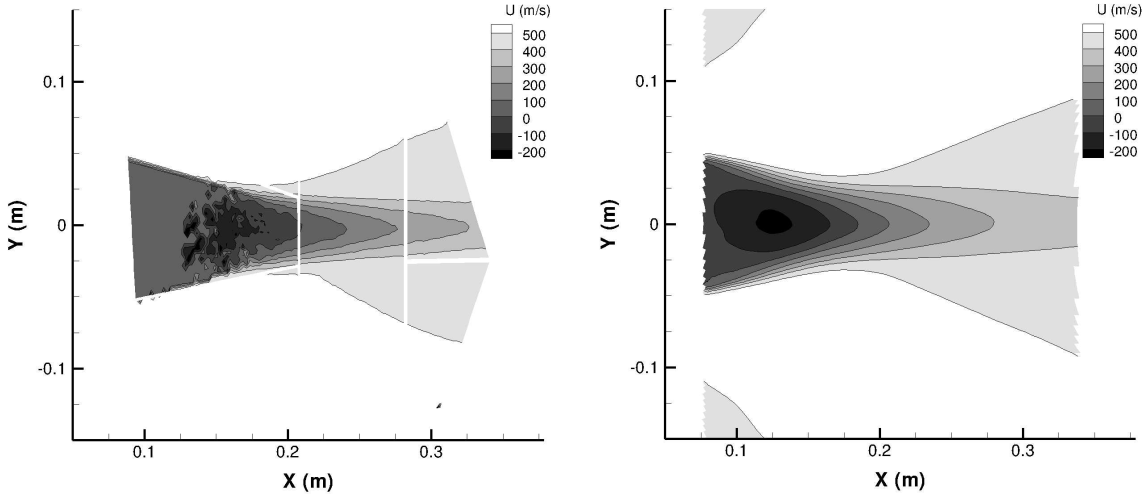

(a) Experiment (b) Simulation

Figure 4.6: Contours of the u-component of velocity in the $x/d = 2$ plane.

Figure 4.8 depicts experimental and simulated contours of the u-component of velocity in the $x/d = 10$ plane. Qualitative differences between the results are more dramatic at this location. The low-speed core is more prominent in the experiment and has an ellipsoidal character in contrast to the more circular contours seen in the simulation. The core widths remain approximately the same however. The momentum deficit from the capsule sting is also evident in the simulation yet not discernible in the experiment. Quantitative comparisons from this figure reveal much better agreement than is visually apparent, however, and they are presented in Figure 4.9. Along the y-axis, the computed profile has a maximum deviation inside the core of approximately 3% from the experimental value. Agreement improves outside of the

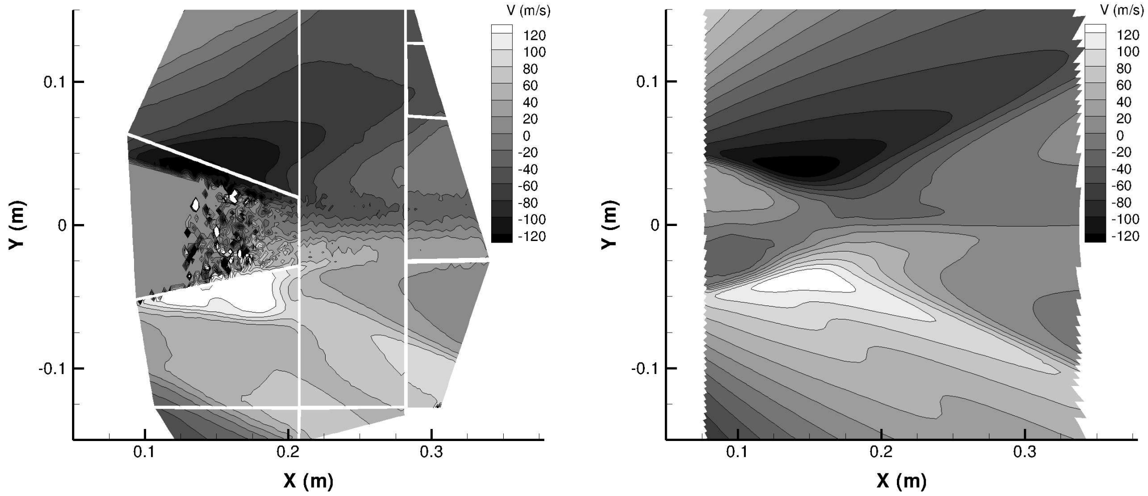

(a) Experiment (b) Simulation

Figure 4.7: Contours of the v-component of velocity in the $x/d = 2$ plane.

core to a radial distance of $0.06 - 0.07$ meters where the simulation begins to deviate once more. Nevertheless, while the computed profile uniformly exceeds experiment outside of this range, it remains within 2% of the measurement. We obtain a similar result along the z-axis. The main feature to note is the persistence of the sting wake readily discerned in the computation above a radial distance of 0.04 meters. This causes the simulated profile to level out while the experiment continues to recover to the freestream. It is also the only point in the wake which is underpredicted by the simulation. The maximum relative error is about 4% in this direction. Interestingly, the profiles obtained from experiment fail to recover exactly to the freestream outside of the wake, in contradiction to our expectation and to what is seen in the simulation. We also note that there is significant asymmetry in the y-axis profile suggesting that these results possibly reflect a bias error in the experiment or perhaps that the statistical profiles are not fully converged. This is confirmed by Sengupta (2007), who states that

> "...the PIV data in the wake deficit region itself are of limited quantitative value. The data quality is reduced as the seed particle density is limited in the low velocity regions of the flow. Insufficient seed particle density makes image cross correlation more difficult and the PIV measurement less accurate."

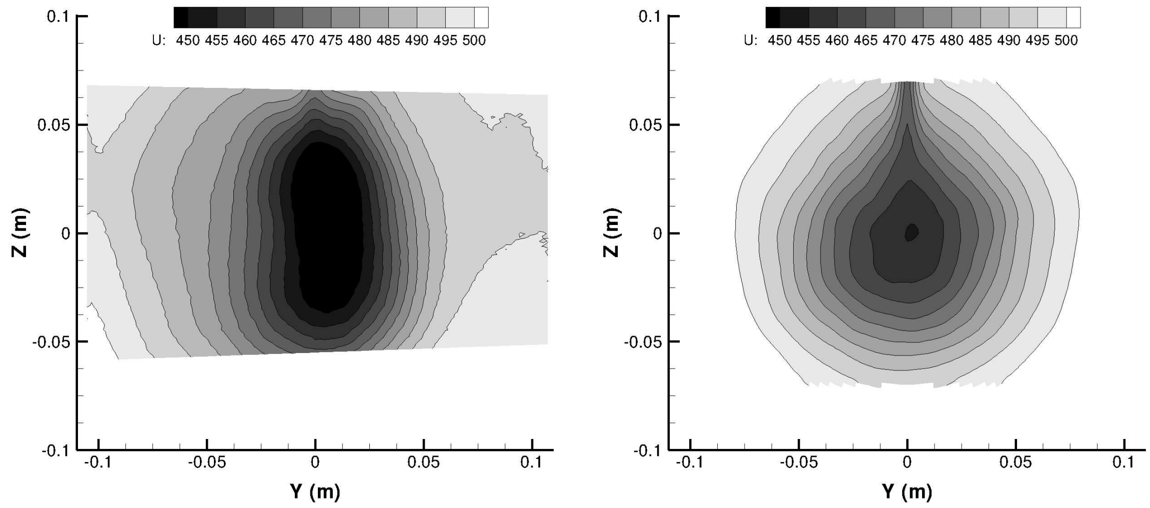

(a) Experiment

(b) Simulation

Figure 4.8: Contours of the u-component of velocity in the $x/d = 10$ plane.

4.3.4 Canopy-Only Configuration

Canopy-only tests were initiated in order to confirm the basic ability of the code to accurately capture the flow through the canopy and predict drag. In this configuration, the canopy bow shock remains almost entirely stationary and it is possible to measure its shape and location from shadowgraph photography. A representative shadowgraph image is shown in Figure 4.10(a). The flow upstream of the canopy is relatively benign, with the bow shock being the only exceptional feature. Yet inside the canopy, it is considerably more complex especially near the gaps. Here, the high-pressure fluid in the canopy escapes, forming a jet which acts to separate the boundary layer from the band. This induces separation on the canopy as a whole and generates numerous small shocks which interact with the nascent wake. The experimental and computed bow shock shapes at each Mach number are shown in Figure 4.10(b). Agreement is good overall with a maximum 1.5% deviation occurring in the Mach 2.5 case.

A more critical measure of the code's performance for this problem is its ability to predict the canopy drag. This is demonstrated in Figure 4.11 which shows the measured and predicted drag coefficient at each Mach number condition. In all cases, the simulation predicts the canopy drag almost exactly, with the difference never

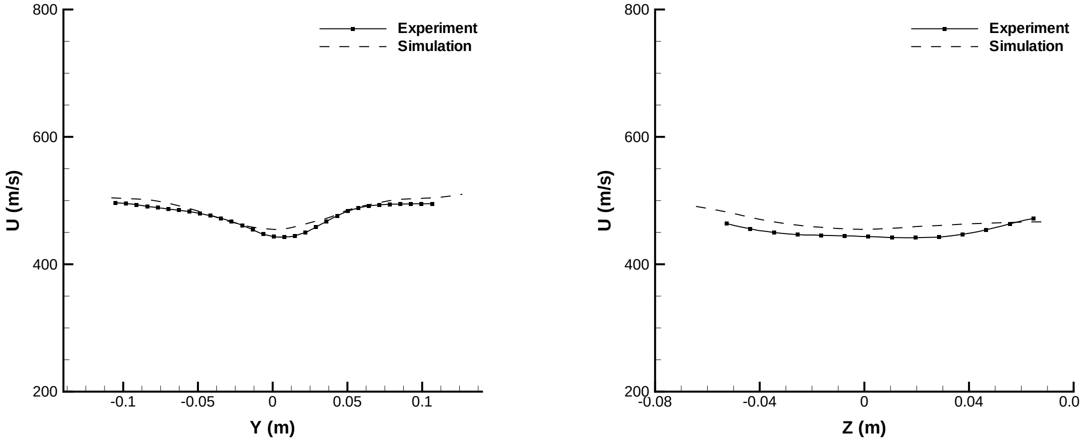

(a) (b)

Figure 4.9: Comparison of simulated and experimental u-component of velocity in the $x/d = 10$ plane. Results are shown for Mach 2.0 in the capsule-only configuration: (a) variation along y-axis; (b) variation along z-axis.

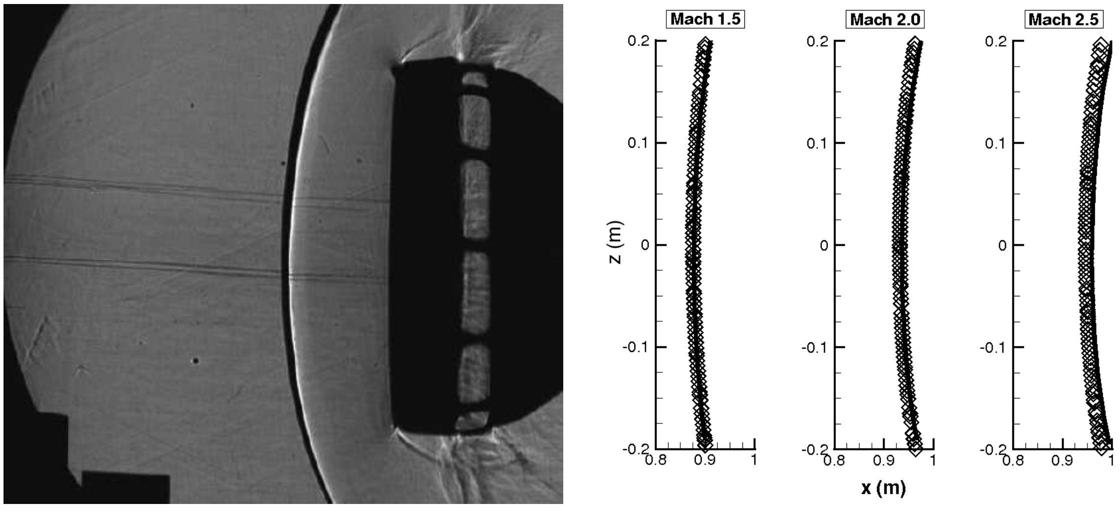

(a) (b)

Figure 4.10: (a) Shadowgraph of canopy-only configuration at Mach 2.0; (b) Comparison of experimental and computed bow shock shapes at each Mach number. Simulation results are indicated by symbols.

exceeding 0.5% of the measured value.

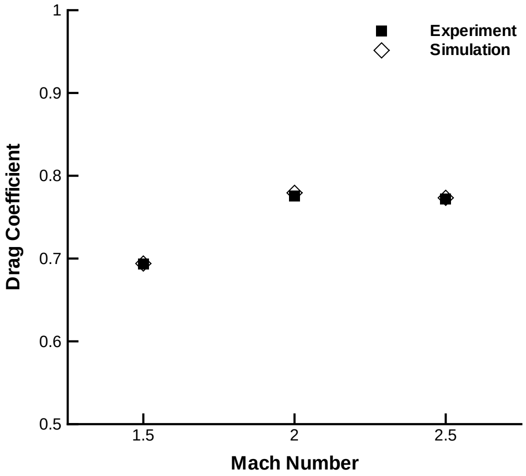

Figure 4.11: Comparison of experimental and computed drag coefficients in the canopy-only configuration.

4.3.5 Capsule with Canopy

In the previous section describing the flow structure of the capsule and canopy geometry, it was noted that the unsteady momentum deficit in the capsule wake generates instability in the canopy bow shock. This in turn leads to an unsteady cycling of pressure within the canopy and a complex, dynamical problem overall. For real supersonic parachutes, the dynamical nature of the problem often results in partial collapse of the canopy structure and therefore a reduction in drag. Because drag is the overriding performance metric in parachute design, we seek to mitigate the possibility of such detrimental phenomenon by understanding the physical mechanisms which drive them. While a truly representative analysis of this problem would require a flexible canopy and the ability to effectively model fluid-structure interactions, there is still useful information which may be gleaned from the current rigid description. In this section, we present a computational analysis of the rigid capsule/canopy problem.

The unsteady nature of the problem is best exemplified by two things: (1) the canopy drag and (2) the axial position of the canopy bow shock. Both quantities are shown in Figure 4.12 as functions of a non-dimensional flow time, defined as the ratio of the canopy trailing distance to the freestream speed. The time-averaged drag on the parachute over the time span of the figure is 2860 N, with oscillations approximately 25% of the mean. The period of the oscillations is between 1-2 flow times, however more data would need to be collected to conclusively determine long-term behavior. The axial shock position shows a similar variation, 0 indicating the leading edge of the parachute. The two curves are significantly correlated with a computed correlation coefficient of 0.72. The reason for this can be understood by looking more closely at the mechanism which drives the unsteadiness in the canopy.

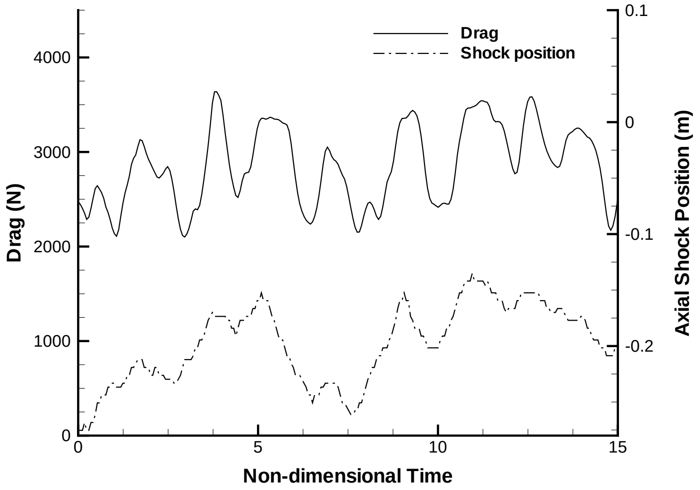

Figure 4.12: Instantaneous canopy drag and centerline bow shock location.

The pattern of over- and under-pressurization is represented schematically through a series of instantaneous images in Figure 4.13. The sequence proceeds from top to bottom. The left column shows a slice through the domain colored by pressure contours. In the first image, we see that the canopy is in an over-pressurized state. Coupled with the incoming momentum deficit in the wake, this serves to push the bow shock upstream. As it moves upstream, the bow shock also becomes more oblique, causing some incoming streamlines to be diverted and inhibiting mass flux into the canopy. In this state, the excess fluid within the canopy is able to escape around the edges of the parachute band, depressurizing the interior of the canopy. The bow shock immediately begins to collapse inward and assume a flatter profile, repressurizing the canopy, and the cycle repeats.

The right column of Figure 4.13 shows an exploded polar view of the surface from within the canopy. These images correspond in time to the images in the left column and are colored by the pressure differential across the canopy surface. Darker contours indicate a smaller outward-pointing differential. Thus, from the middle image, it is suggested that the cycle of pressurization is responsible for the observed area oscillations in supersonic parachutes. Here the pressure differential becomes relatively small and, in certain locations of the band, visibly negative, even for the case of a rigid canopy. It is clear that if the parachute were allowed to deform in this state that it would experience at least a partial reduction in its effective area. A similar mechanism was identified by Lingard and Darley (2005). In their work, they simulated the Mach 1.5 flow around the main Cassini-Huygens parachute coupled to the Stardust forebody with a methodology which also accounted for fluid-structure interactions with the canopy. However, whereas they reported a strong disruption to the forebody flowfield with the canopy bow shock lensing up to the capsule base, this is not evident in our simulations. A possible explanation for this is that the trailing distance of the parachute relative to its diameter was somewhat smaller than for MSL. Additionally, they reported a substantially subsonic wake which enhanced the ability of the canopy bow shock to travel upstream. While our simulations also reveal a partially subsonic wake, the canopy depressurizes before the shock can move into the capsule flowfield. In this case, the unsteady momentum deficit of the wake by itself is sufficient to drive the concurrent canopy instability.

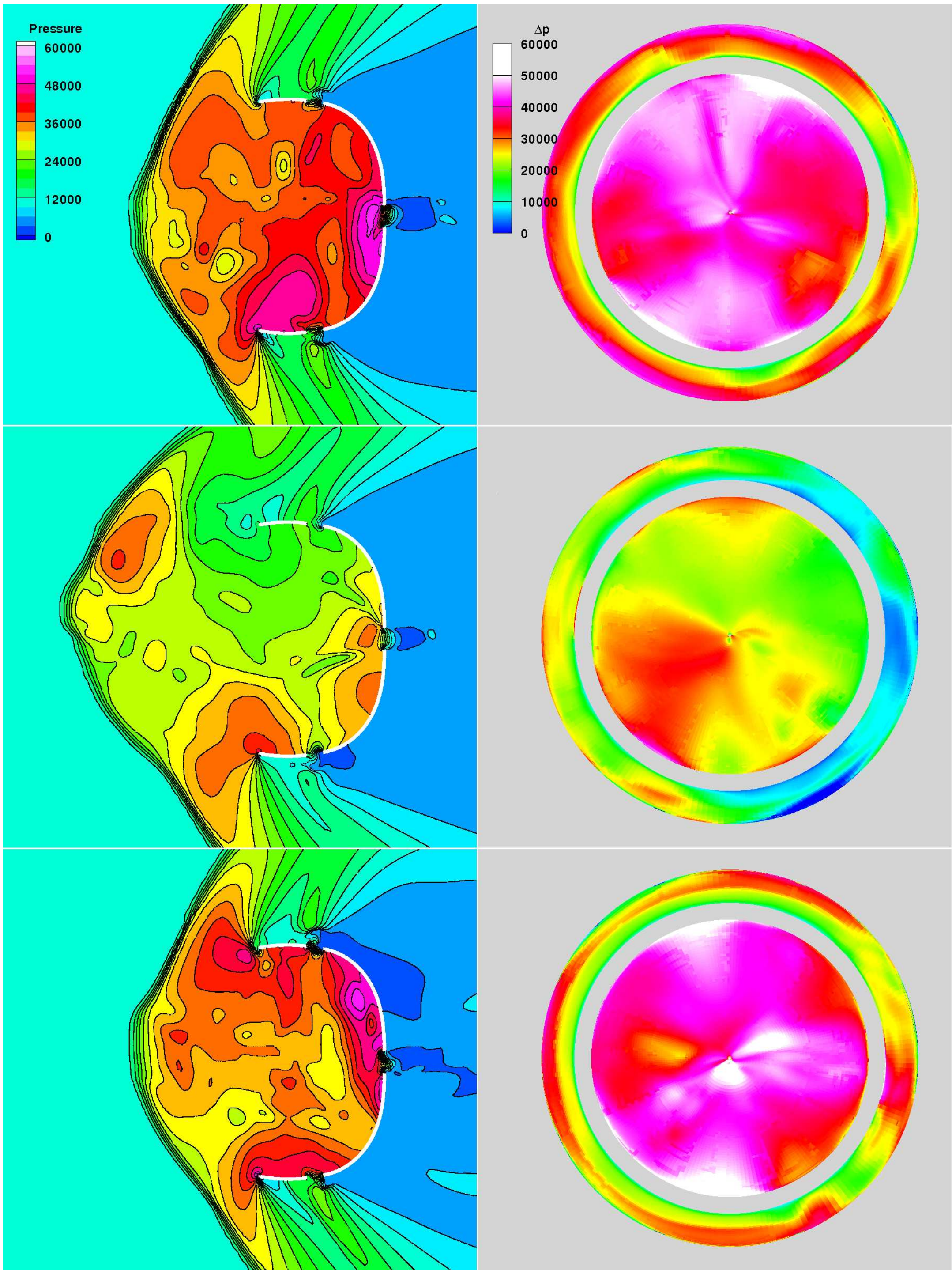

Figure 4.13: Sequential depiction of parachute pressurization cycle. Left images show pressure contours through domain symmetry plane. Right images show an exploded polar view of the pressure differential across the canopy surface.

Chapter 5

Reentry-F Flight Experiment

5.1 Introduction

In recent years, the aerospace industry has witnessed rapid development of applications whose designs depend critically on analysis of surface heating due to unsteady, turbulent flow. For instance, the MSL mission discussed in the previous chapter highlights the critical role of unsteady flows in the entry, descent, and landing phase of interplanetary missions. Before deployment of the parachute can occur, the vehicle must slow significantly by flying a controlled descent through the Martian atmosphere. This will require firing four pairs of reaction control system (RCS) thrusters during the initial entry. Firing of the thrusters into the vehicle wake can result in augmented heating to the backshell: the hot exhaust gas mixes with the wake, raising the overall temperature to which the afterbody TPS is subjected. In some circumstances, the jets may impinge directly on the vehicle surface, creating local hot spots and potential for burnthrough. Even during periods of RCS inactivity, the vehicle's wake itself can enhance afterbody heating upon becoming unsteady or turbulent by increased fluid mixing which acts to draw hotter fluid from outside of the boundary layer nearer to the vehicle surface. Accurate aerothermal predictions of these environments are important in order to avoid overly conservative TPS designs that arise from safety margins prescribed to mitigate mission risks. For example, the margin policy for the design of the Crew Exploration Vehicle (CEV) TPS currently lists the margin attributed to turbulent aeroheating during lunar return second only to that of radiative heating. The increased vehicle mass incurred by such policies directly results in larger mission costs through greater fuel demands and reductions in allowable payload.

CFD has been successful at predicting the flight environments of relatively simple configurations for which the flow remains attached or is largely laminar [see, for instance, Brown (2002) and Wright (2004)]. However, certain aspects of commonly used computational approaches are either incompatible or at odds with producing high-fidelity, unsteady aerothermal simulations. In particular, the conventional RANS approach, though widely used throughout the industry, is well known to incorrectly predict vehicle heating in highly separated flow regions. As demonstrated in the previous chapter and elsewhere in the literature, DES has shown promise with regard to capturing the dominant flow dynamics in relatively low Mach number supersonic flows, but its use in the hypersonic regime is mostly untested. Therefore, we look to the available experimental data as a means to examine the ability of DES to accurately model highly unsteady, compressible flows in which vehicle heating is a primary concern.

Experiments with hypervelocity flows can be broken into two general categories, ground and flight tests, each with their relative merits and drawbacks. Ground tests are excellent for applying a wide range of measurement techniques, including flow visualization. The measurements themselves are often very reliable and the flow conditions are well-defined. Unfortunately, a given test facility has a limited range of test conditions that it can achieve and cannot reproduce true flight environments. Examples include the studies of Horvath (1997) and Danehy (2006) in the NASA Langley Mach 10 wind tunnel, as well as various experiments by Holden in the LENS facilities. Conversely, flight tests have a fairly limited measurement capability but are the only way to test in actual flight conditions. Furthermore, the amount of flight test data is extremely limited due to the high costs of the tests themselves. Most available data at reentry conditions is nearly 40 years old, making it difficult to find appropriate documentation on which to build a reasonable simulation. A few good examples can be found in the FIRE II (1965), Sherman-Nakamura (1968), and Reentry-F (1968) tests. The interested reader is referred to Bulmer (1975) and Wright (2005) for excellent surveys of the experimental literature. Due to the large amount of documentation available for Reentry-F, as well as the overall quality of the dataset, we have selected it to analyze the performance of our approach under typical flight conditions. Analysis of ground based experiments is deferred to Chapter 6.

Prior work with the Reentry-F experiment has concentrated on comparisons to heating and pressure measurements along the conical section of the vehicle (herein referred to as the forebody). Wood *et al.* (1997) presented comparisons of boundary layer profiles along the forebody from three CFD codes at the 80 kft trajectory point but made no effort to compare with the flight data. Brown (2002) used the dataset to evaluate several RANS turbulence models. Several simplifying assumptions were made such as a constant isothermal wall temperature and zero angle of attack. Nevertheless, he concluded that an appropriate choice of model was sufficient to accurately predict forebody transition and heating within approximately 10% of the true values. In the study by Lin (2006), several trajectory points were selected to reflect laminar, transitional, and turbulent conditions on the base. The results from these simulations were somewhat mixed due to their use of a RANS model, however this only serves to highlight the shortcomings of such methods. Furthermore, the authors were able to discern a strong dependence on even slight angles of attack, a feature that we note in our analysis as well. In Barnhardt (2006), we presented preliminary results of the same conditions used in this work. Many assumptions were made, including zero angle of attack and lack of inclusion of the base support ring, and results were generally in poor agreement with the flight data. Nevertheless, the study exposed several potential sources of modeling error and guided further development of our computational methods.

5.2 Problem Description

5.2.1 Reentry-F

Reentry-F was a flight test conducted by NASA in 1968 whose goal was to investigate vehicle heating in a turbulent environment. For the experiment, the spacecraft was launched outside the atmosphere and then accelerated back at reentry velocity on a ballistic trajectory. A schematic of the vehicle is shown in Figure 5.1. The body consisted of a 3.96 m long 5° half-angle cone constructed from beryllium with a 0.254 cm radius graphite nose tip. Upon separation of the vehicle from the final stage of the launch rocket, a support ring remained attached to the base; its configuration may be found in *NASA TM X-2468* (1972). The center section of the base was closed with a glass phenolic bulkhead.

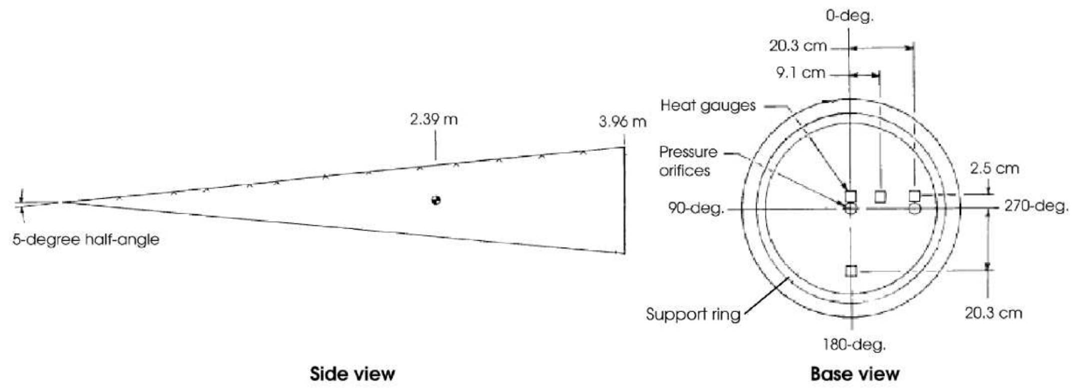

Figure 5.1: Schematic of the Reentry-F vehicle.

The conical section of the body was outfitted with a variety of instrumentation to aid in defining local flow conditions and boundary layer transition. Thermal measurements were made at 21 locations along the conical section of the body with two thermocouple arrays. The primary array ($\phi = 0°$, also referred to as the leeward array) consisted of 12 thermocouples while the secondary array ($\phi = 180°$, also referred to as the windward array) consisted of 5 thermocouples. The 4 remaining thermocouples were installed at the 90° and 270° circumferential positions of two separate axial locations. Additionally, there were 13 pressure taps along the forebody. Base instrumentation was comparatively limited and included 4 heat transfer gauges and 2 pressure ports.

Data collection spanning the beginning to end of boundary layer transition occurred over an altitude range of 100,000 to 60,000 feet. The Mach number over this period was approximately 20 while the unit Reynolds number of the freestream varied from 6.56×10^6 to 52.5×10^6 m^{-1}. The total enthalpy varied from 18.3 to 16.9 MJ/kg. For this study, two trajectory points were selected for which corresponding data indicated a transitional or turbulent flow on the base. The conditions are summarized in Table 5.1.

The angle of attack, η, was nonzero yet it remained less than 1° throughout the duration of the flight. While previous studies have generally treated this as small enough to be negligible, it in fact has a significant impact on computational results

Table 5.1: Freestream conditions used in Reentry-F simulations.

Altitude	**70 kft**	**80 kft**	
Re_L	30.10	18.50	(10^6/m)
M_∞	19.93	20.01	
ρ_∞	0.070920	0.043523	(kg/m^3)
U_∞	5.900	5.965	(km/s)
T_∞	218	221	(K)
T_{Base}	354.0	354.0	(K)

and must be properly considered.[1] At 80 kft, the vehicle was oriented with a 0.25° pitch angle and −0.2° yaw angle, for an effective angle of attack $\eta = 0.32°$. At 70 kft, the orientation changed to a 0.5° pitch angle and −0.35° yaw angle, for an effective angle of $\eta = 0.61°$.

Additional information concerning the spacecraft flight conditions, construction, instrumentation, and measurements may be found by searching NASA documentation; the most relevant reports used for this work are listed in the References section.[2]

5.2.2 Experimental Uncertainties

In order to properly define the numerical problem and assess our results, we must first identify and quantify the sources of experimental uncertainty. Some, such as instrument accuracy, are readily apparent and explicitly stated in the original reports. Others are the result of unforeseen circumstances that occurred during the flight. All of these contribute a certain degree of unreliability to the flight data, however we believe the overall quality of the dataset to be quite good. In this section, we attempt to establish reasonable bounds on the various experimental uncertainties.

The easiest to ascertain are the instrument accuracies because they were established through pre-launch calibration and reported in *NASA TM X-2308* (1971). The thermocouples had a rated accuracy of ±11 K. This combined with uncertainty in the data reduction process to produce a forebody heat flux accuracy of ±3.4 W/cm^2 for laminar conditions and ±17.0 W/cm^2 for turbulent conditions. Two types of pressure

---

[1] Lin (2006).

[2] See in particular *NASA TM X-1856* (1969) and *NASA TM X-2308* (1971).

gauges were used at each port indicating a low and high range of operation. The corresponding accuracies were ±14 Pa and ±140 Pa, respectively. Interestingly, despite listing a low-range pressure accuracy around 2%, it is stated in the report that "*the low-range gauges . . . were used primarily to indicate when transition first moved onto the base. They would not hold a constant calibration during ground tests and, hence, were not depended upon to give accurate pressure data.*" The heat transfer gauges on the base were rated to be accurate within ±1.13 $\mathrm{W/cm^2}$.

The vehicle orientation is stated to be accurate within ±0.1°. This is a rather high value considering the relatively small deviations from the nominal ballistic trajectory that the spacecraft experienced. An accurate representation is further complicated by the fact that the spacecraft experienced thermal distortion due to uneven surface heating and hence had a variable local angle of attack. Although the extent of distortion cannot be precisely determined, *NASA TM X-2250* (1971) provides an analysis based on a thin shell finite difference technique. This study found that the maximum local angle of attack augmentation was approximately 0.1° and 0.5° for the 80 kft and 70 kft altitudes, respectively. Forward of the vehicle bending point, the thermal distortion had a net effect of *increasing* the orientation angle. Aft of the bending point, however, the vehicle experienced a *decrease* in effective orientation angle. Thus, the potential error in defining the vehicle's orientation is roughly the same magnitude as the measured orientation itself. The sensitivity of the CFD results to such errors will be discussed in further detail in a subsequent section.

No sensors were present to measure the base wall temperature, however it is necessary to provide an estimate for the CFD solver. The base temperature was determined from the provided heat flux measurements by solving the thermal diffusion equation and approximating the glass phenolic bulkhead as regular glass. This resulted in an isothermal wall temperature of 354 K. Note that this approach has large uncertainty but it is the only available estimate at this time. We believe that the potential error resulting from this procedure would have only a minor impact on the computational results.

Nose tip recession occurred during the flight due to ablation. Although no detailed measurements of recession were made, estimates may be found in *NASA TM X-1856* (1969). It is noted in the report that the analysis accounts only for thermochemical ablation despite ground test evidence that mechanical erosion of graphite would also be expected at reentry flight conditions. Since the effect of nose radius on the downstream measurements cannot be determined *a priori*, we chose in this study to use both minimum and maximum estimates during preliminary simulations. The results suggest that the overall impact is negligible except in a small laminar region just downstream of the nose tip.

Finally, *NASA TM X-2308* provides accuracy estimates for the freestream conditions; however, they are not considered in the present work. All freestream conditions are extracted directly from interpolation of the published measurements. A summary of pertinent experimental uncertainties is provided in Table 5.2.

Table 5.2: Experimental uncertainties of the Reentry-F test.

	Uncertainty
Thermocouple	±11 K
Laminar Heating	±3.4 W/cm^2
Turbulent Heating	±17.0 W/cm^2
Pressure Gauge	
Low	±14 Pa
High	±140 Pa
Base Heat Gauge	±1.13 W/cm^2
Orientation, η	
Measured	±0.1°
Thermal Distortion	0.1° (80 kft)
	0.5° (70 kft)

5.3 Simulation Methodology

5.3.1 Flow Modeling

The temperatures in the stagnation region of the nose and the shear layer recompression downstream of the base are sufficiently high to cause nitrogen and oxygen dissociation, yet not so high that the flow becomes ionized. Therefore we have chosen to model the chemical kinetics of the gas with a five species finite-rate model comprised of N_2, O_2, NO, N, and O. Forward reaction rates are computed using Park's 1990 coefficients with equilibrium constants determined from NASA Glenn thermodynamic data.[3] Laminar diffusion coefficients are computed using a combination of Blottner curve fits for viscosity, an Eucken relation for thermal conductivity,[4] and, for mass diffusion, a constant Lewis number of 1.4 for air.

5.3.2 Mesh Design

Because it was unknown beforehand what mesh spacing was necessary to sufficiently resolve the turbulent structures in the wake and their effect on the Reentry-F vehicle, we therefore took the approach of splitting the simulation into two independent parts, the forebody and base. Working independently of the base flow, the forebody can quickly and easily be computed via the line relaxation methods discussed earlier. From the perspective of the base simulation, the forebody is thus treated as a 'black box' and, once a suitable forebody solution is obtained, the results are used to provide an inflow boundary condition to the base. This is justified because the flow over the forebody remains attached and steady so that there is no adverse flow interference from the base and the solution does not change once the near wall gradients are adequately resolved. Splitting the simulation in this manner allows us to easily assess various mesh topologies and resolutions for the base and select the optimal ones.

Forebody solutions were generated using the isothermal wall temperature distribution given in *NASA TM X-1856* for locations downstream of the 0.406 m thermocouple. Malik (2003) estimated the temperature distribution upstream of this location for Reentry-F at 100 kft; we adopted this same distribution but scaled it to match the temperature at the first thermocouple. Early simulations showed a weak dependence on the ablated nose radius except in the laminar region near the nose tip itself. Therefore we simply chose to use the minimum estimates given in the literature for subsequent simulations. No effort was made to model transition to turbulence along the forebody. Instead, the S-A model's production term was suppressed until a specified transition location. Since our primary interest is the base flow, the transition locations were determined by matching the locations of peak turbulent heating to those reported in the Reentry-F dataset.

Once a good set of inflow conditions has been obtained from a forebody simula-

---

[3] *NASA RP-1311* (1994)

[4] Vincenti and Kruger (1982)

tion, the main concerns in the base region are to properly capture the primary shear layers and adequately resolve the near wake. In order to resolve the shear layers, the grid topology was aligned to them as much as possible. Three different grid resolutions were employed to assess the near wake resolution of DES. An initial grid resolution estimate was made from experience with the simulations found in Sinha *et al.* (2004) and Barnhardt (2005, 2006). Various mesh topologies were then tested in an attempt to optimally distribute grid cells in the wake. The final coarse, medium, and fine grids consisted of 1.7, 4.2, and 9.7 million cells, respectively. The corresponding nominal cell dimensions, Δr, in the near wake were 1.11, 0.60, and 0.25 cm. Figure 5.2 shows the coarse base mesh alongside an associated instantaneous solution.

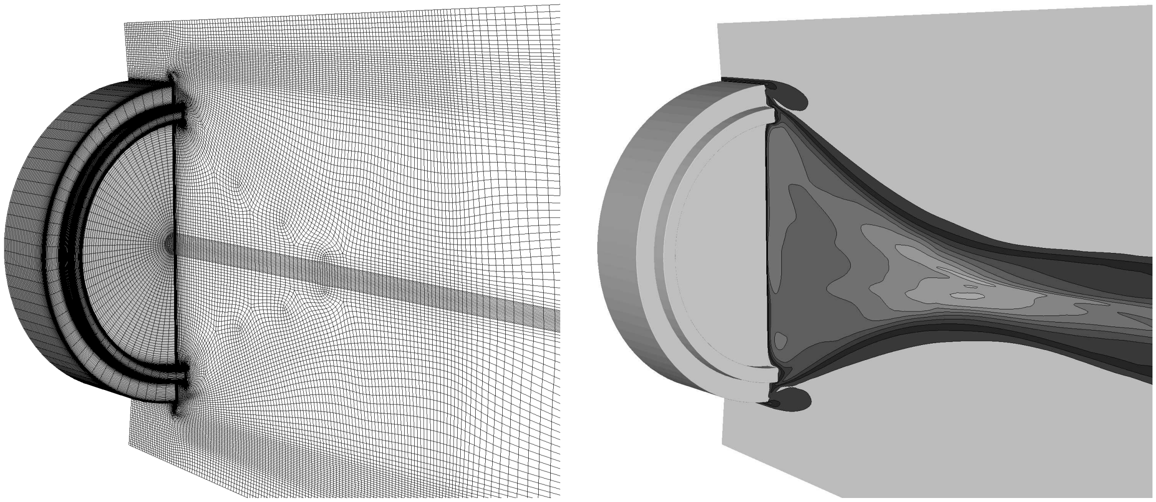

(a) (b)

Figure 5.2: (a) Grid topology used in the base simulations. Coarse grid resolution is depicted; (b) Overlay of corresponding temperature contours at 80 kft conditions.

Table 5.3: Summary of grids used in this study.

	Cell Count (millions)	Δr (cm)
Coarse	1.7	1.11
Medium	4.2	0.60
Fine	9.7	0.25

5.3.3 Data Reduction Process

Due to the unsteady nature of the base flow, we have chosen to present our results based on the time-averaged flow field from which we can derive expected quantities. Clearly, however, for a given trajectory point, there is a fairly large variation in measured quantities throughout the simulation time. This is shown graphically in Figure 5.3 where we see both instantaneous and time-averaged heat flux contours on the base.

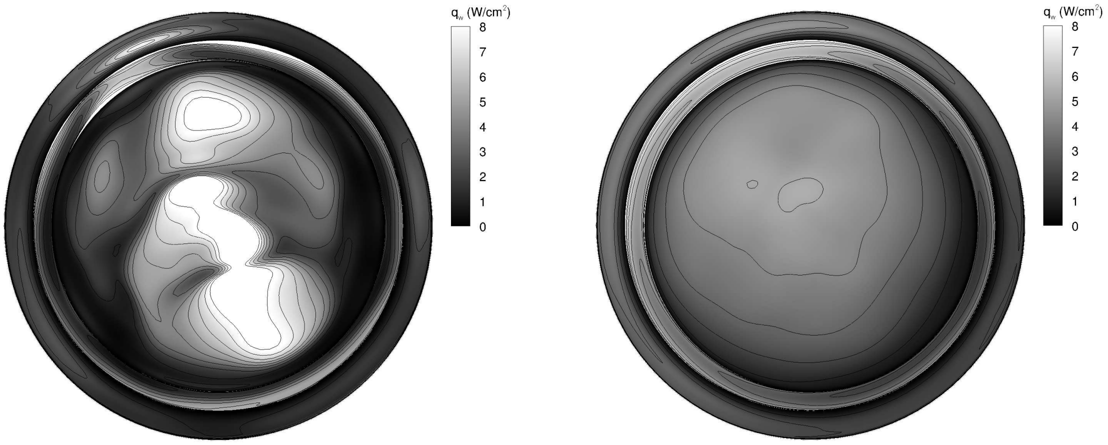

(a) Instantaneous

(b) Time-averaged

Figure 5.3: Comparison between instantaneous and time-averaged representations of heat flux contours on the Reentry-F base at 80 kft, $\eta = 0°$.

During the experiment, heat flux measurements were taken at a frequency of 10 Hz. In contrast, the computational time scale is approximately 10^{-7} seconds per time step. Thus it is impractical to analyze data over a time period equivalent to the experiment. To overcome this limitation, we time-average the data for a predetermined number of flow times (approximately 200 for each simulation), defined here as the ratio of the base diameter to freestream velocity. While it is possible with this process that some low frequency modes present in the flow may not be completely captured, in our experience the mean readily converges to a near steady state. Experimentation with this method has shown that variation of the mean between simulations is small relative to experimental uncertainties, and therefore this effect may be ignored. Additionally, use of this technique in combination with other statistical measures such as RMS and standard deviation should be considered in order to develop a more complete understanding of the flow. It is important to note, however, that there is no fundamental connection to be made between the unsteady, instantaneous data from the experiment and our time-averaged results. As can be seen in Figure 5.3, the variation in heat flux on the base exhibits such a range that it would be all but impossible to correlate to any one instant from the flight data, particularly because the flight data were sampled at a much lower frequency than the unsteady time scales of the base flow, see Figure 5.4. Moreover, information regarding the transient response of the gauges is not available and makes it impossible to precisely determine how accurately the gauge measurements resolved the time scales of the wake. Yet we may infer from other Apollo-era experiments that the transient response was probably quite low and therefore resulted in the recorded data points being, in a sense, "time-averaged" as the flow evolved at a rate faster than the gauges could respond. Hence the time-averaged comparisons presented herein should be regarded not as a direct validation of the computational method but only as providing compelling evidence (or lack thereof) of a strong correlation between the flight data and simulation.

5.4 Flow Structure

As mentioned previously, the flow along the forebody remains attached and steady. Temperatures in the stagnation region are sufficiently high to cause dissociation of nitrogen and oxygen but the flow does not ionize. As the flow expands around the spherical nose along the body it is essentially chemically frozen. At some point downstream, the flow transitions to turbulence; when the slight angle of attack is considered, the transition profile around the body becomes asymmetric. Progressing deeper into the atmosphere pushes the transition front forward along the vehicle. Once the boundary layer has become fully turbulent, the velocity profiles at the wall naturally become fuller and temperature gradients are enhanced, increasing the heat flux to the wall.

Figure 5.5 depicts the typical base flow structure. The shear layer separates from the forebody and expands to enclose the recirculating region. Downstream the shear layer recompresses, heating the gas significantly and leading to further dissociation. The structure of the recirculating region changes as the flow passes from the laminar

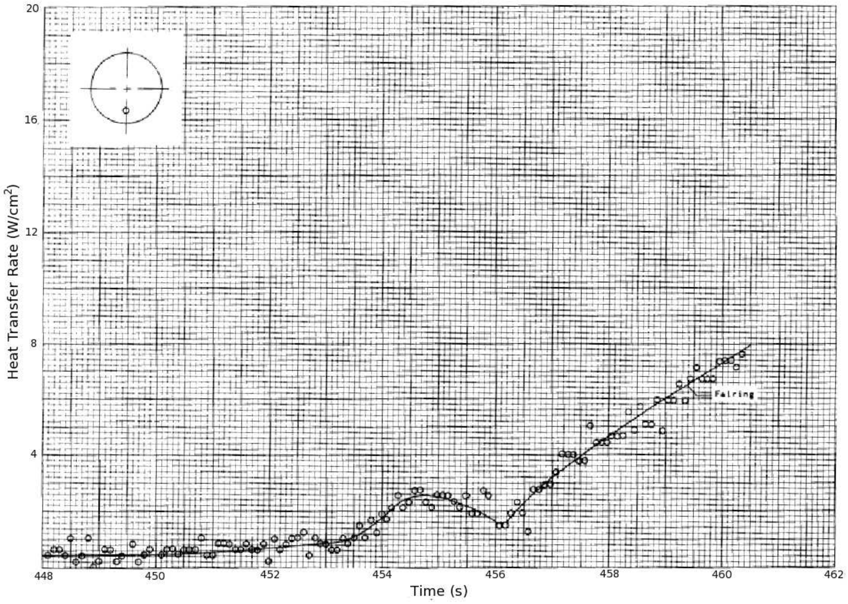

Figure 5.4: Example of available base flow data from Reentry-F experiment. Figure depicts instantaneous measurements of heat transfer rate from the $r = 20$ cm, $\phi = 180°$ gauge.

to turbulent regimes. When the flow is laminar, the base flow is dominated by a single large toroidal vortex. The transonic flow at the vortex center impinges on the base, compressing the flow and creating peaks in surface pressure and heating profiles near the base center. The vortex begins to break down through transition until the flow is turbulent. At this point, the flow is very unsteady and chaotic with eddies breaking down into a large range of length scales. The enhanced turbulent mixing in the wake works to create more uniform pressure and heating profiles.

5.5 80 kft Trajectory Point

5.5.1 Forebody

Building on the work first presented in Barnhardt (2006), we maintained the initial assumption of zero angle of attack while incorporating the previously neglected support ring. Forebody transition profiles from the earlier axisymmetric simulations are shown in Figure 5.6 for two ablated nose radii at the 80 kft condition. Note that the two nose radii provide very similar profiles except in the laminar region near the

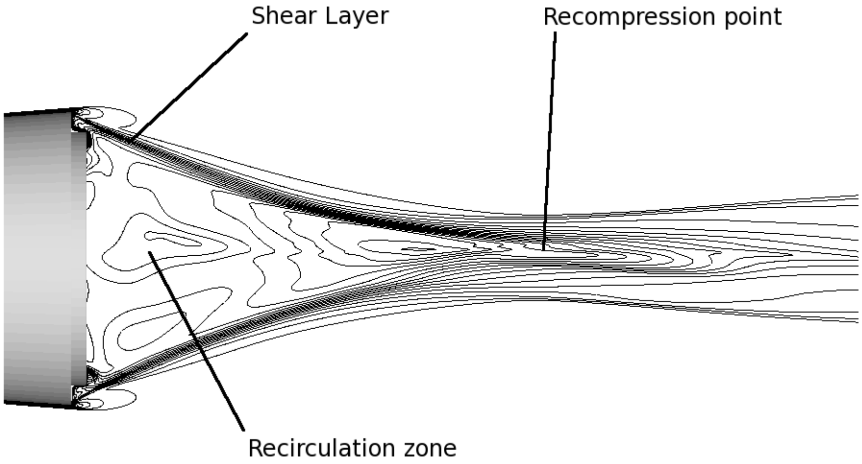

Figure 5.5: Base flow structure of Reentry-F.

nose tip. All else being equal, the smaller estimate more accurately reproduces the flight data in this instance and this observation was assumed to extend to subsequent cases. The transition zone is captured poorly as expected from the crude method described earlier. Nevertheless, the S-A model does a reasonable job predicting the turbulent heating levels.

5.5.2 Base Grid Resolution Study

Since no turbulence spectra are available from the flight data, we have no way of estimating beforehand how well the base flow will be resolved by the mesh. Therefore we must rely on a grid resolution study to evaluate the fidelity of the DES model. Simulations were run on each of the coarse, medium, and fine mesh resolutions and comparisons of base pressure and heating profiles at 80 kft are shown in Figure 5.7. Error bars reflect the reported uncertainty from the flight test. Not surprisingly, on a coarse mesh, the DES model's behavior reverts to a RANS-like trend with pronounced peaks near the centerline. In fact, as we shall demonstrate for this particular case, the DES result on a coarse grid is much worse than the corresponding RANS result on a refined grid. Refining the mesh improves the model's accuracy considerably. At medium and fine resolutions, pressure recovers the expected nearly uniform profile and, while it lies outside the bounds of experimental uncertainty, the relative error is well under 15% across much of the base. We note also the original report's comment

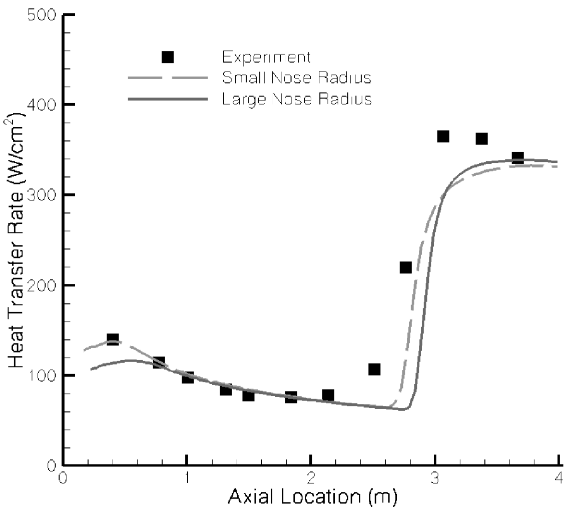

Figure 5.6: Transitional heating profile along the forebody at 80 kft, $\eta = 0°$.

that the gauges "*were not depended upon to give accurate pressure data*" in this range due to calibration issues. The predicted heat transfer profile improves to actually lie within the experimental uncertainty. Based on this result, we determined that the medium resolution mesh provided the optimal balance between solution accuracy and computational cost, and it was therefore chosen as the base resolution for all subsequent simulations.

5.5.3 DES v. RANS

Because RANS is still so widely used for aerothermal applications, it is instructive to analyze the accuracy of RANS relative to that of a resolved DES simulation. Figure 5.8 depicts a comparison between the RANS and DES models using the inflow profile of Figure 5.6 on the medium mesh. Neither RANS nor DES is capable of predicting the base pressure within the experimental uncertainty, however they both do a reasonable job of capturing the fairly uniform trend. As noted previously, despite missing the experimental uncertainty, the DES profile stays within 15% of the correct value. The heat flux profiles show a similar trend. RANS greatly overpredicts heating near the base center and the distribution does not correlate well to the experiment. DES captures the essential distribution within measurement uncertainty for the most part.

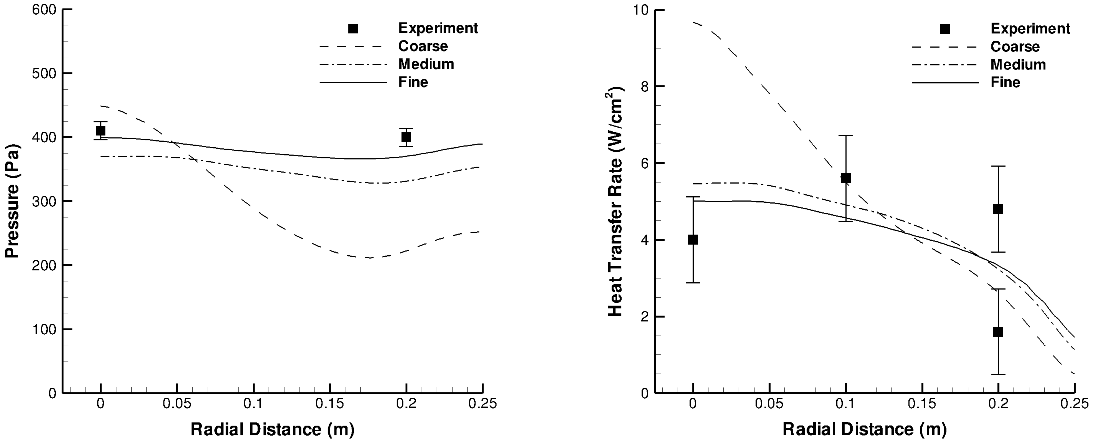

(a) Pressure

(b) Heat Flux

Figure 5.7: Base pressure and heating profiles at 80 kft on coarse, medium, and fine meshes, $\eta = 0°$.

This comparative behavior is explained by the aforementioned excessive dissipation created by the RANS formulation which tends to damp out small-scale eddies so only a single toroidal vortex remains. Thus, despite the turbulence model being active and increasing diffusive transport, the flow structure is such that a peak appears in the heating profile near the center. Interestingly, this has the concurrent effect of distributing the fluid mass so that the density is excessively low inside the ring. This explains why the pressure is significantly underpredicted.

5.5.4 0.32° **Effective Angle of Attack**

It now remains to explain the discrepancy between the two heat gauges located 20 cm radially from the base center. Recalling Figure 5.7, when $\eta = 0°$ the base heat flux profile splits neatly between the two measurements. This suggests that the asymmetry is perhaps due to the vehicle's orientation. The effective angle of attack at this altitude was actually 0.32°, although we had approximated this to be 0° in the initial simulations. To assess the influence of a small orientation angle, we now present results incorporating the full three-dimensional body with correct pitch and yaw angles as determined from the flight data.

In *NASA TM X-1856*, it is shown that the forebody boundary layer transitioned

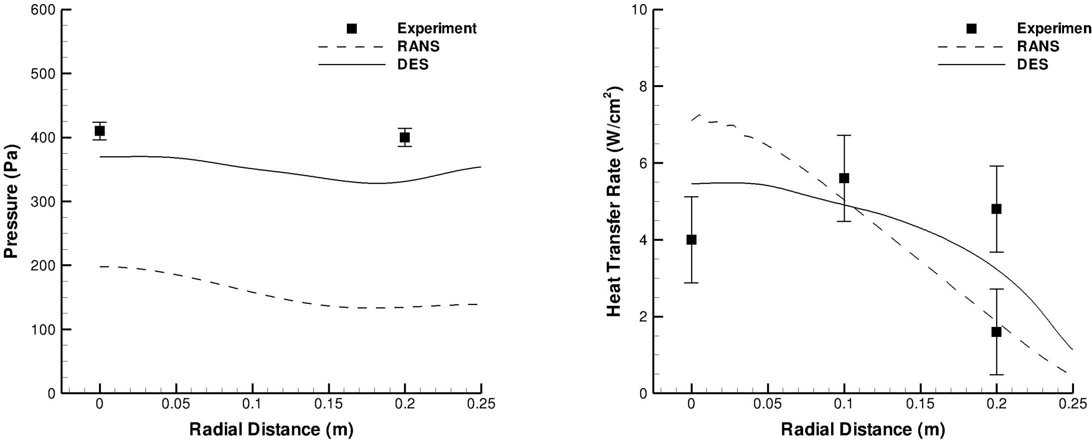

(a) Pressure (b) Heat Flux

Figure 5.8: Comparison of DES and RANS solutions at 80 kft, $\eta = 0°$. Simulations performed on medium mesh.

asymmetrically and this is attributed to the small effective angle of attack. This is a fact which, to the author's knowledge, has not been addressed in any prior studies. We incorporate this effect into our three-dimensional simulation by specifying a leeward and windward transition location (determined from the report), and then linearly interpolating between them to determine the circumferential location of the transition front. Doing so yields the transition profile illustrated in Figure 5.9. Agreement with the experimental data is quite good along both leeward and windward arrays.

Figure 5.10 shows the adjusted base heat transfer contours accounting for the vehicle orientation. The black squares on the contour plot indicate the locations of the heat transfer gauges. Sampling these locations and plotting against experiment reveals excellent agreement. Each point lies within the measurement uncertainty of the corresponding gauge. Thus it is confirmed that the slight pitch and yaw angles play a critical role in explaining the apparent asymmetry of the Reentry-F flight data.

5.6 70 kft Trajectory Point

Finally, let us consider another trajectory point at a lower altitude. The larger Reynolds number implies a greater range of length scales and provides an interesting case to test the DES model's ability across a broader range of conditions. We choose

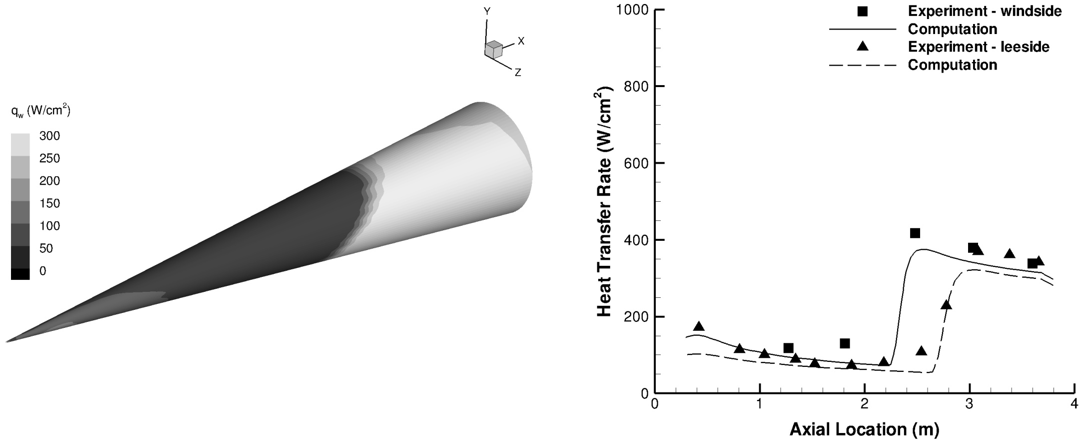

(a) (b)

Figure 5.9: (a) Heat flux contours on the forebody at 80 kft, $\eta = 0.32°$; (b) Transition profiles along windside ($\phi = 180°$) and leeside ($\phi = 0°$) thermocouple arrays.

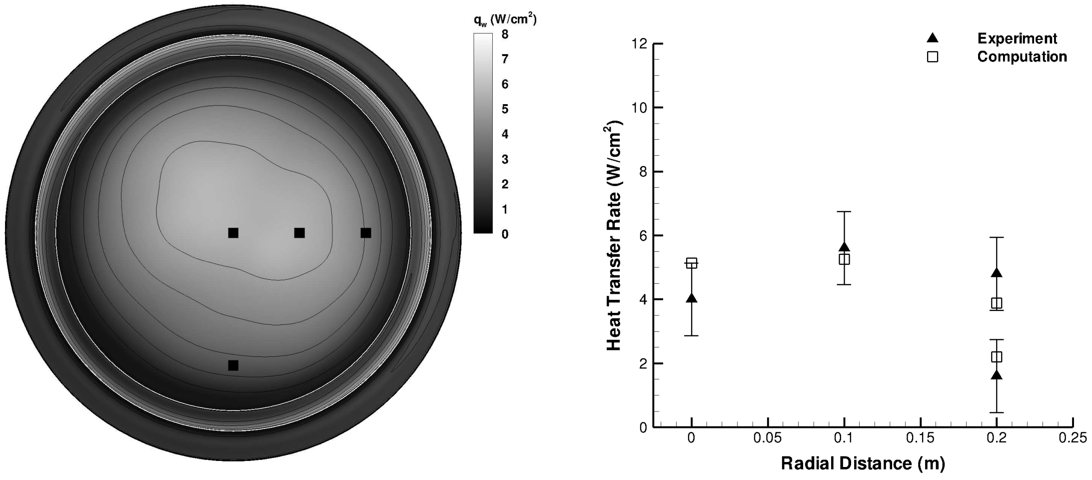

(a) (b)

Figure 5.10: (a) Heat flux contours on the base at 80 kft, $\eta = 0.32°$. Gauge locations are depicted as black squares; (b) Comparison of discretely sampled heat flux values.

the 70 kft conditions specified earlier with the knowledge that thermal distortion of the vehicle was appreciable at this point in the trajectory. The potential error in defining the effective angle of attack is of the order of the measured angle of attack. In order to determine the sensitivity of the base flow to such errors, we simulated the vehicle at the reported pitch and yaw angles as well as an artificially selected orientation, namely half the nominally reported angles. The artificial orientation is chosen specifically to reflect that the vehicle bent upward about a forward point, thus reducing the effective angle of attack on the bulk rear portion of the forebody, and to lie within the bounds of the previously reported uncertainties.

5.6.1 Forebody

Figure 5.11 plots the leeward and windward transition profiles along the forebody for both orientations. The artificially determined orientation has little impact on the overall accuracy of the predicted heat transfer rates; the windside becomes slightly less accurate while the leeside prediction improves. Nevertheless, neither simulation produces error in excess of 10% with the exception of the transition region for reasons discussed earlier.

5.6.2 Base Grid Resolution Study

Due to the larger Reynolds number, a separate grid resolution study was performed for this altitude. The coarse grid was rejected out of hand because it was found to be insufficient at 80 kft. The remaining two resolutions are shown in Figure 5.12, which plots the discretely sampled gauge measurements at the $\eta = 0.6^\circ$ orientation. It is apparent that the finely resolved mesh does little to improve upon the accuracy of the medium resolution mesh. Pressure exhibits a flat trend in both cases with the finer mesh attaining slightly higher levels. The heat transfer rate follows a similar pattern. Neither simulation is particularly accurate with pressure off by as much as 15% and heat flux off by 30% at the $r = 10$ cm gauge location. Using the medium resolution mesh, we next examine the sensitivity of the base flow to errors in the specification of vehicle orientation.

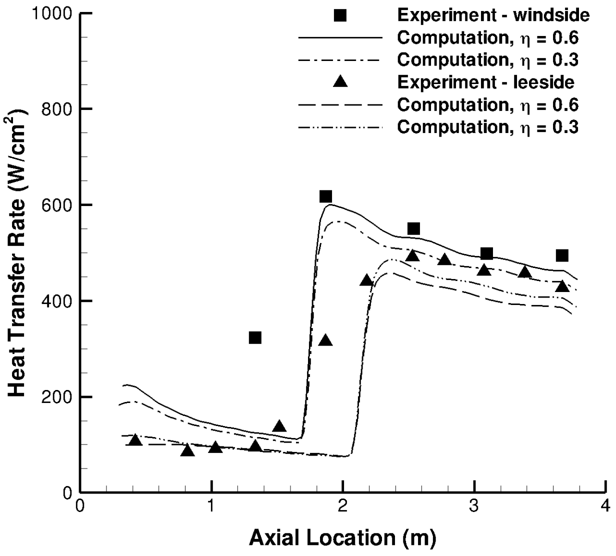

Figure 5.11: Transitional heating profile along the forebody at 70 kft, $\eta = 0.6°$ and $0.3°$.

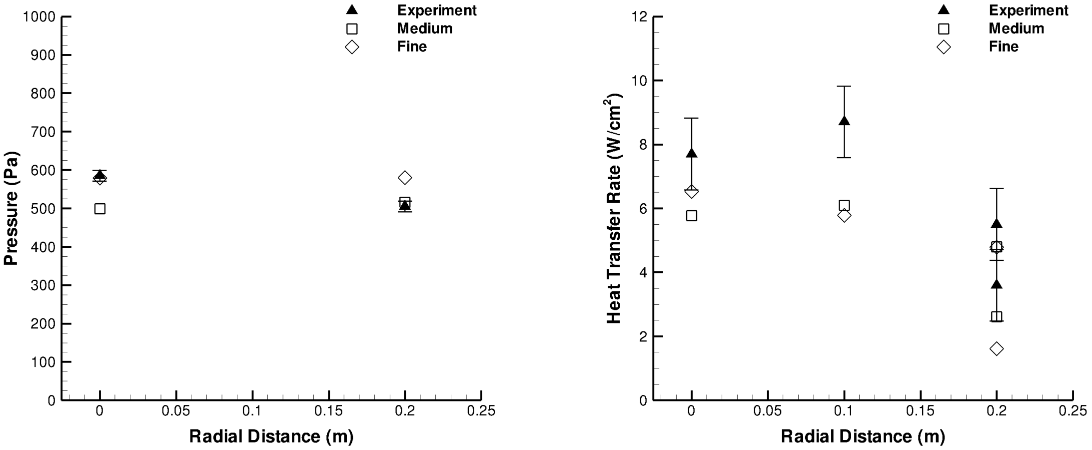

(a) Pressure

(b) Heat Flux

Figure 5.12: Base pressure and heating profiles at 70 kft on medium and fine meshes, $\eta = 0.6°$.

5.6.3 Angle of Attack Sensitivity

The computed base measurements exhibit a much greater sensitivity to orientation than do forebody measurements. This is illustrated in Figure 5.13, which plots the measured heat transfer rate at the selected orientations. Here we see that the difference in orientation of 0.3° can plausibly explain the error in base heat flux seen at the reported pitch and yaw angles. Given that the artificially chosen orientation lies within the stated measurement uncertainty, and that this orientation physically approximates the effects of thermal distortion, it seems justified to conclude that the DES model is quite capable of accurately predicting base heat flux for this case within our limits to accurately specify the vehicle orientation, geometry, and flow conditions.

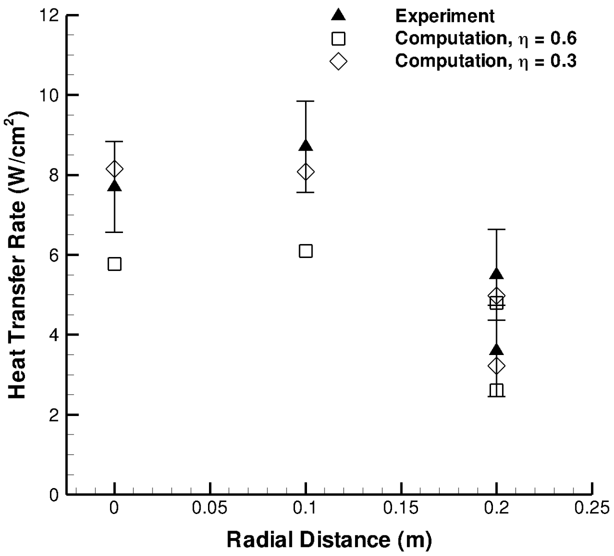

Figure 5.13: Computed heat transfer rates on the base at 70kft, $\eta = 0.6°$ and $0.3°$.

Chapter 6

Spherical Capsule Experiments

6.1 Introduction

In the previous chapter, we examined our methodology in the context of a flight environment via the Reentry-F experiment. By comparing our simulations to the experimental data, we concluded that the methodology could indeed predict vehicle heating in a turbulent environment within the limits of our ability to accurately specify the flight conditions. Yet the uncertainty of the experimental specification remains and, with it, a certain amount of uncertainty in the analysis itself is unavoidable: there is simply no mechanism by which we can unequivocally identify the relative contributions of the various sources of error. A second consideration is the relative simplicity of the Reentry-F configuration. The slender shape of the cone, with its sharply terminating base, reduces the complexity of the near wake to its basic elements: a shear layer and recirculating region. While this is helpful as a means to understand the essential structure and behavior of a turbulent base flow, the Reentry-F test is insufficient to answer all questions pertaining to validation of our methodology in a practical flight environment.

In this chapter, we address these concerns by presenting further validation against spherical capsule experiments conducted in the high-speed wind tunnels at CUBRC. First, the controlled nature of the CUBRC tests and the use of modern data acquisition techniques provides a tremendous wealth of reliable data. Problems can be broken down parametrically in order to discern dependencies on such things as angle of attack, Mach number, Reynolds number, or freestream enthalpy. Likewise, improvements in instrument design allow modern models to be densely instrumented with gauges capable of accurately resolving transient phenomena within the kilohertz frequency range (recall for comparison that Reentry-F's heat gauges operated at a 10 Hz sampling rate). Second, the capsule model which we have selected for this study is essentially a stand-in for an Apollo-style configuration and hence the NASA Crew Exploration Vehicle (CEV) as well. The tests are therefore relevant toward understanding the nature of separated flows in a practical flight environment. Additionally, the gradual flow separation experienced by the capsule model and the aftbody presence of a sting mount add significant complexity and should provide a unique challenge to our underlying numerical and physical models.

6.2 Problem Description

6.2.1 CUBRC Facilities

The CUBRC facilities are comprised of four distinct tunnels: the LENS-I, LENS-II, and 48" reflected shock tunnels, and the LENS-X expansion tunnel. Each tunnel is designed to replicate a particular range of velocity and altitude conditions. Taken together, the CUBRC tunnels are able to reproduce almost entirely the Apollo and Space Shuttle entry trajectories in the continuum regime.

The reflected shock tunnels work by heating and pressurizing a stagnant test gas which is then expanded through a converging-diverging nozzle to achieve the desired test condition. They were designed primarily to investigate flow physics of interceptor and scramjet configurations at full-scale. LENS-I is thus capable of duplicating flight conditions from Mach 7 to 15 while matching Reynolds number up to Mach 22. LENS-II is a complementary tunnel with an operational capability from Mach 3.5 to 10. The LENS-X expansion tunnel is designed to produce a high enthalpy flow in such a way that the flow is largely free of frozen, dissociated contaminants. This is accomplished in two stages. First, the test gas is compressed and heated by a shock without being stagnated by a reflected shock. Next, additional energy is added to the flow via an unsteady expansion through an acceleration segment. The test gas is then expanded isentropically through the test chamber to reach its final high-enthalpy state. While this process typically results in shorter test times than a reflected shock tunnel (up to 4 ms, versus approximately 25 ms in LENS-I and 100 ms in LENS-II [Holden et al. (2008)]), it is necessary in order to cleanly duplicate a flight condition in excess of 10 MJ/kg (MacLean et al., 2009).

The driving factor in selecting a suitable set of tests for this study was to maximize the test duration time such that the turbulent base flow could fully establish and still have sufficient time to acquire data over many flow times (defined by the freestream velocity and capsule diameter). A secondary consideration was to maximize the peak Reynolds number to ensure turbulent behavior. A trade study was performed by MacLean et al. (2008) in which they concluded that the 48" tunnel operating at a nominal Mach number of 6 offered the most balanced solution. At this condition, the tunnel can reach Reynolds numbers as high as 8.5×10^7 per meter, or a full order of magnitude greater than what was seen to produce transitional wake behavior in previous studies. Preliminary runs indicated that reliable heat transfer measurements typically took around 9 ms to establish, followed by an additional 10-12 ms of usable test time.

Further details of the CUBRC facilities' design and operation may be found in the previously cited works.

6.2.2 Capsule Configuration

As stated earlier, the nominal model configuration used in this study is an Apollo-style spherical capsule chosen to closely resemble the proposed Crew Exploration Vehicle being designed by NASA as a replacement for the soon-to-retire Space Shuttle fleet. A detailed schematic is shown in Figure 6.1. All dimensions shown in the figure are given in inches. The scale of the model was chosen after carefully considering the test core diameter of the 48" tunnel as well as the time necessary for the model's wake to fully establish. The model is fixed with a 28° angle of attack, which is near the peak L/D for this configuration. Three sting mount configurations were used during the course of testing: (1) round center mounted sting, (2) diamond cross-section center mounted sting, and (3) a split sting attached to the capsule at two lateral points. Of these, only the round center mounted sting was considered in this study.

The topologies and sizing used in this work are developed from experience with the simulations presented in the previous chapters. While not shown here, the sizing was further refined through a preliminary grid resolution study of the most turbulent case and a single grid was used for all simulations. To the extent possible, grid refinement

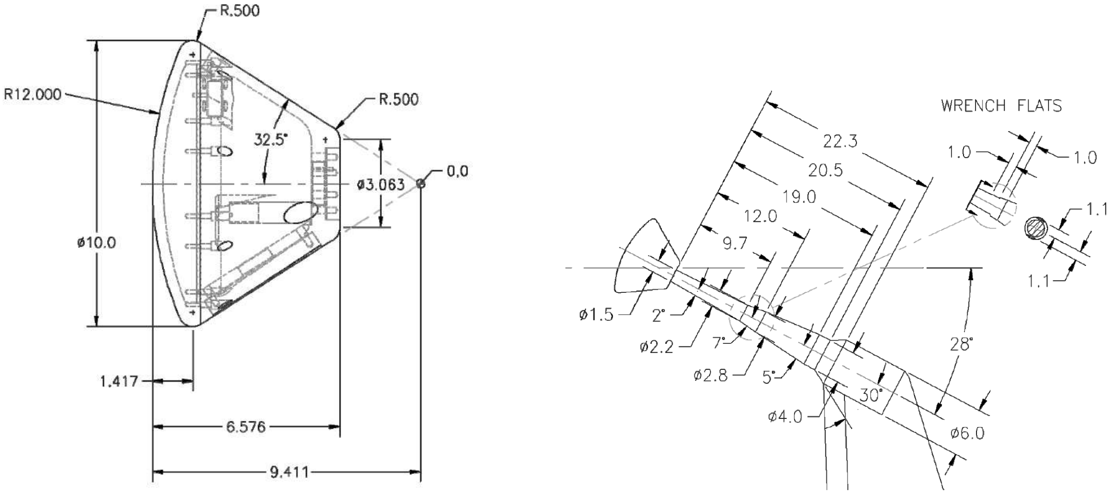

(a) Capsule

(b) Round Sting Mount

Figure 6.1: Schematic of the spherical capsule geometry.

was localized to the wake region of the leeside aftbody so that unnecessary refinement of the far field was minimized. The final result is a mesh comprised of 9.7 million cells. The cell width in the wake is nominally 2.5 mm, or approximately 1% of the model diameter. Figure 6.2 depicts the surface and symmetry planes of the mesh.

The capsule model is instrumented with a total of 85 sensors, including all inserts and optional measurements. Of these, 38 are piezoelectric pressure gauges and 47 are heat transfer gauges. With the round center-mounted sting in place, the number of gauges was reduced to 35 and 39, respectively. The complete instrumentation map is shown in Figure 6.3. The forebody instrumentation is relatively sparse and is meant only for basic confirmation of test conditions. Four coaxial thermocouple gauges are placed on the capsule centerline, with two additional thin-film gauges at each shoulder. The pressure gauges are located along two orthogonal rays. It is important to note that the limited amount of forebody instrumentation also limits our knowledge of boundary layer transition, a fact which affects some of our subsequent modeling choices for this problem.

The remaining gauges are distributed in rays along the aftbody. In this study, because the number of gauges is quite large, proper identification of each component is a critical task in order to coherently break down the presentation of results. To this end, we have chosen to label the instrument rays according to a clockwise angular

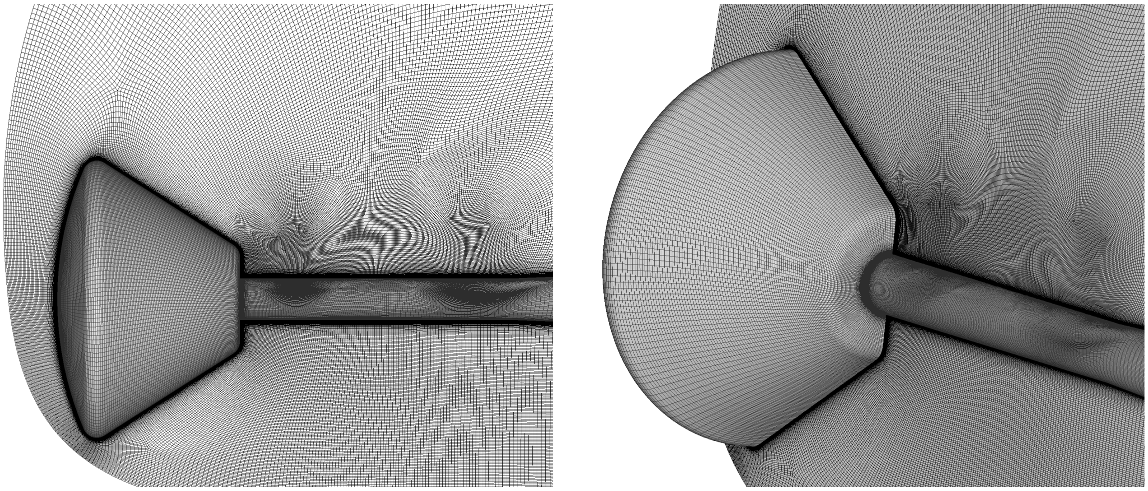

(a) Symmetry Plane

(b) Perspective View

Figure 6.2: Grid topology used in the spherical capsule simulations.

naming convention, where the angle is denoted by ϕ. At 28° angle of attack, the $\phi = 0^\circ$ ray corresponds to the most leeward side of the capsule while $\phi = 180^\circ$ is most windward. The individual gauges are identified using a consecutive numbering scheme. Thus, accounting for missing and inoperable gauges, the pressure gauges are simply labeled [1 - 35] and the heat transfer gauges [36 - 74]. Note that this numbering scheme differs somewhat from that used by MacLean et al. (2008). For detailed comparison to that study, refer to Table 6.1 for a complete transposition of the two labeling schemes. Throughout the remaining text, we have made an effort to further identify the gauges descriptively so that the spatial relationships among the gauges are clear.

6.2.3 Test Conditions

Numerous datasets are available from this series of experiments, representing runs using the various sting configurations across a range of Reynolds numbers and freestream enthalpies. For simplicity, we have chosen to limit our analysis to the runs which used the round center mounted sting. Five runs were made in this configuration, spanning a range of Reynolds numbers from 2.6×10^6 to 8.5×10^7 per meter. The relevant freestream conditions are given in Table 6.2. Of these cases, Run 5 exhibited peculiarities during the data reduction process and so it was rejected for inclusion in this study. We also determined that Runs 1 and 3 were redundant because their

Table 6.1: Transposition of gauge numbering schemes referred to in this study.

	Current	MacLean et al. (2008)
Pressure	1 - 35	P1 - P7, P10 - P37
Heat Transfer	36 - 74	T1 - T11, T13 - T17, T21 - T43
Forebody		
	1 - 3, 12 - 15	P1 - P3, P14 - P17
	36 - 41	T1 - T6
$\phi = 0°$		
	4 - 7	P4 - P7
	42 - 46	T7 - T11
$\phi = 13°$		
	16 - 18	P18 - P20
	52 - 55	T21 - T24
$\phi = 26°$		
	19 - 21	P21 - P23
	56 - 59	T25 - T28
$\phi = 38°$		
	22 - 24	P24 - P26
	60 - 63	T29 - T32
$\phi = 64°$		
	25 - 27	P27 - P29
	64 - 66	T33 - T35
$\phi = 90°$		
	28 - 30	P30 - P32
	67 - 69	T36 - T38
$\phi = 135°$		
	31 - 33	P33 - P35
	70 - 72	T39 - T41
$\phi = 150°$		
	34, 35	P36, P37
	73, 74	T42, T43
$\phi = 180°$		
	8 - 11	P10 - P13
	47 - 51	T13 - T17

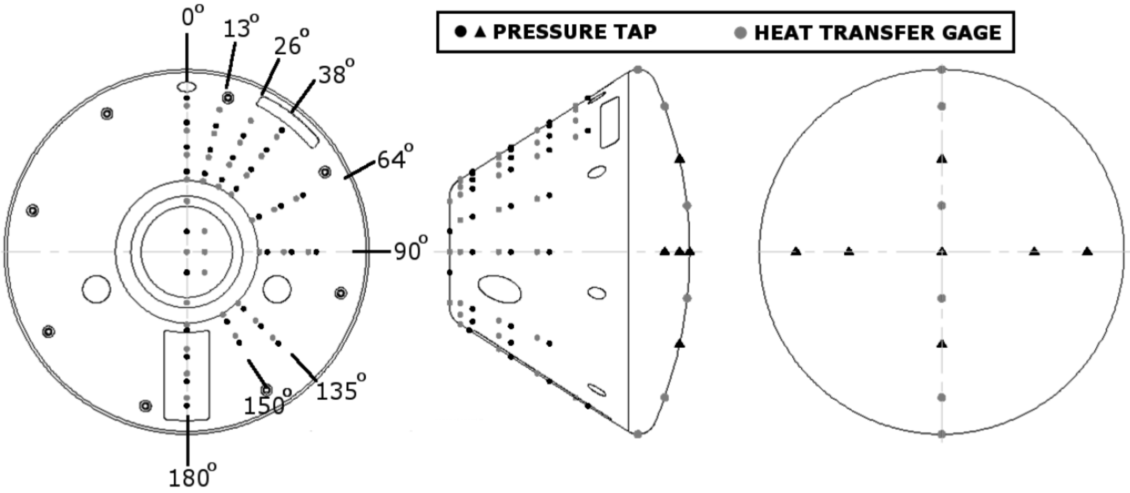

Figure 6.3: Instrumentation map for spherical capsule experiments. (l) aftbody, (m) side view, (r) forebody.

Table 6.2: Test conditions for the spherical capsule with round center mounted sting.

	Run 1	**Run 2**	**Run 3**	**Run 4**	**Run 5**	
Re_L	13.50	42.40	24.80	2.57	84.90	(10^6/m)
M_∞	6.37	6.41	6.43	6.46	6.45	
ρ_∞	0.05261	0.19252	0.11229	0.01371	0.33424	(kg/m^3)
U_∞	964.63	1102.46	1106.85	1292.38	994.11	(m/s)
T_∞	57.08	73.63	73.76	99.62	59.13	(K)
T_{Wall}	295.56	295.56	292.78	292.78	292.78	(K)

respective Reynolds numbers placed them both in the transitional regime and our primary interest is to assess turbulence modeling, not enthalpy effects. Our final analysis is therefore concerned with Runs 4, 3, and 2, representing nominally low, medium, and high Reynolds number wake flows, respectively.

6.3 Numerical Results

6.3.1 Flow Structure

Flow visualizations of the temperature contours in the symmetry plane are shown in Figure 6.4. Aside from the higher freestream enthalpy apparent from the forebody

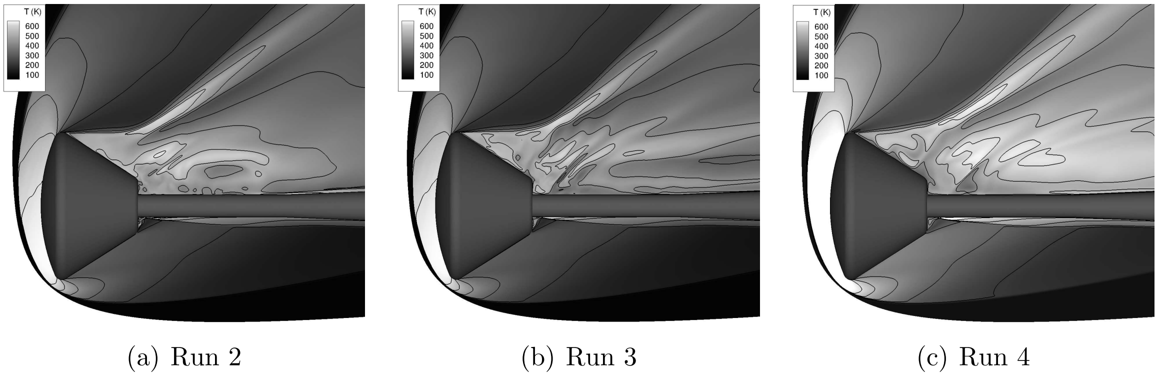

(a) Run 2 (b) Run 3 (c) Run 4

Figure 6.4: Flow visualization of temperature contours in the symmetry plane.

contours of Run 4, all of these runs share essentially similar flow features. The flow along the windside aftbody is aligned with the freestream and therefore remains steady and attached. Depending on the freestream Reynolds number, the boundary layer in this region may transition to turbulence. The boundary layer then separates at the base of the capsule, creating a small recirculating region that interacts with the sting mount. As we move circumferentially about the capsule toward the leeside, the flow gradually begins to separate until we are in the wake region. At this point, the flow is fully separated and we see a marked increase in unsteadiness. All cases are characterized by the shedding of vortices from the aftbody, although the range of apparent length scales is greater in the turbulent cases as expected. Furthermore, a secondary interaction exists between the larger separated capsule flow and that which emanates from behind the sting.

6.3.2 Low Reynolds Number, Run 4

We first examine the capabilities of our method in a nominally laminar flow as a means of isolating purely numerical errors from those due to problems inherent to turbulence modeling. Wright et al. (2006) demonstrated a reasonable ability to predict laminar afterbody heating on the Apollo AS-202 command module using DPLR without regard for resolving the temporal evolution of the flow. Thus, at a minimum, we should be able to reproduce their accuracy levels given the heritage shared by DPLR and US3D.

Figure 6.5 depicts comparisons between experimental and numerical measurements of time-averaged pressure and heat transfer rate for Run 4 at all gauge loca-

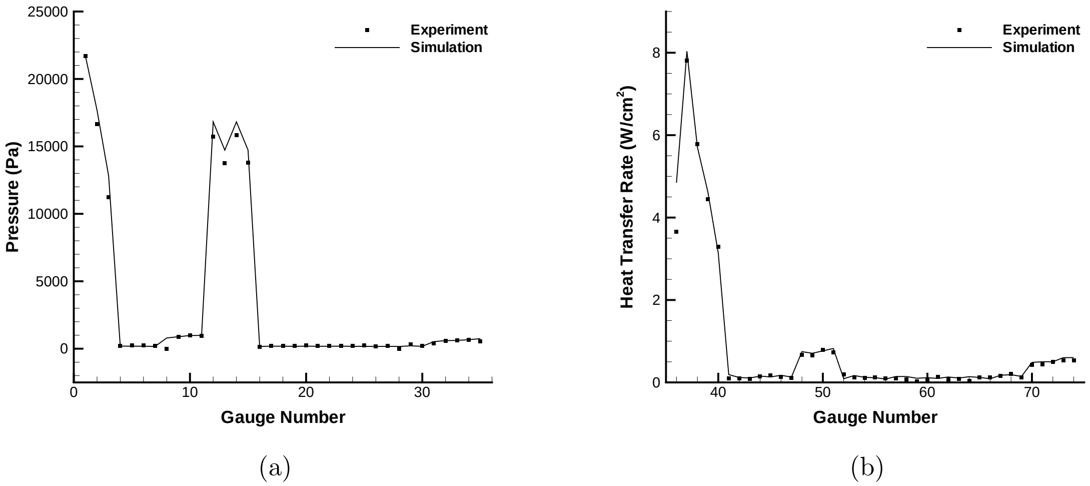

(a) (b)

Figure 6.5: Comparison of experimental and numerical measurements for Run 4. (a) Pressure, (b) Heat transfer rate.

tions. We remark here that not all gauges were operable during each run. Gauges P8, P9, T12, and T18 - T20 (as referenced in MacLean et al. (2008)) were all removed in order to accommodate mounting of the capsule to the round center-mounted sting. Thus, as stated earlier, the gauges have been renumbered in a consecutive manner, ignoring the absent gauges for ease of presentation.

In this numbering scheme, the forebody instrumentation is represented by gauges [1 - 3, 12 - 15, 36 - 41]. Interestingly, agreement between computation and experiment at these conditions is uniformly excellent except for the forebody pressure. In fact, the experimental measurements for these gauges were independently deemed anomalous prior to conducting the computational phase of this study. The reasons for the discrepancy remain unclear although it has been speculated (MacLean, private communication) that it is perhaps due to calibration error. That the computational results are unable to adequately predict what is typically a very routine measurement supports this conjecture. Nevertheless, all of the remaining gauges compare quite favorably, always within a few percent of the experimental value.

6.3.3 Medium Reynolds Number, Run 3

We next turn our attention toward modeling of transitional and turbulent flows. For a transitional flow, weve simply selected Run 3 by virtue of it having the next highest Reynolds number, one which also coincides with previous experience simulating the transitional/turbulent flow of the Reentry-F vehicle. As noted earlier, turbulence modeling is handled by the Spalart-Allmaras equation with the standard DES modification.

Because the flow is transitional, we can anticipate that it will be difficult to accurately capture the experiment in the absence of some relatively sophisticated transition model. We therefore adopted the approach to simulate the experiment as both a laminar and fully turbulent flow with the hope that the results will bound the data. This is reflected in Figure 6.6, which shows results similar to that for Run 4.

Pressure, as we would expect, is unaffected by the turbulence model. In both simulations, we obtain uniformly excellent agreement with the experiments. Heat transfer, on the other hand, is considerably more erratic. First, we note the large differences between the experimentally measured forebody values and those predicted by the simulations. The laminar model here is clearly inappropriate, underpredicting the peak heating value by nearly 60%. Still, one cannot say that the turbulent simulation performs perfectly either, particularly in the stagnation region between the nose and windside shoulder. This kind of behavior has been noted in several prior studies dealing with high Reynolds number forebody flows. An explanation for the disagreement is not currently available, however it is apparent in all of our simulations for which the forebody exhibited characteristics of turbulent behavior.

Otherwise, the aftbody simulations perform as expected. That is, the laminar solution uniformly underpredicts the experiment while the fully turbulent solution uniformly overpredicts it. This is best exemplified by the windside gauges [47 - 51] along the $\phi = 180°$ ray. Here we see that the laminar profile maintains an essentially flat character while the turbulent profile immediately peaks near the capsule shoulder (gauge 51) and then gradually decreases toward the base (gauge 47). In contrast, we see a slow ramping up of turbulent heating from the shoulder to the base in the experiment. By the time the flow reaches gauge 47, the comparison between experiment and the fully turbulent simulation is actually quite good. This suggests

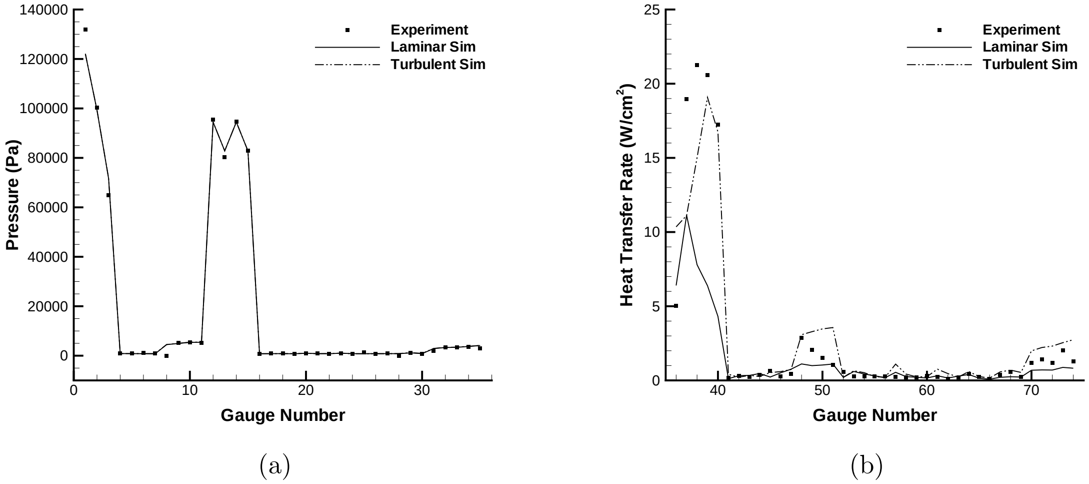

(a) (b)

Figure 6.6: Comparison of experimental and numerical measurements for Run 3. (a) Pressure, (b) Heat transfer rate.

that the flow is indeed transitional and that an accurate simulation of this flow would be possible with the incorporation of a suitable transition model.

6.3.4 High Reynolds Number, Run 2

Let us now consider the high Reynolds number case of Run 2. Because this case was expected to be fully turbulent, the simulation was performed using only the fully turbulent model. As with Runs 3 and 4, the results are presented in Figure 6.7 for the entire range of gauges. Again, agreement of the pressure profiles is uniformly excellent. The apparent disagreement at gauges [8 - 11] is due to these gauges being inoperable during the test. With regard to heat transfer rate, we see much improved agreement over the transitional results at nearly every gauge, often within the measured standard deviation of the flowfield. Yet there are a couple of problematic regions. The difficulty of predicting stagnation point heating at high Reynolds number is once again evident. The windside boundary layer also has a slower transition relative to the computation. Nevertheless, these errors seem to be relatively localized and the aftbody gauges are unaffected.

It is instructive to break down the presentation into the constituent rays of gauges in order to gain some insight into the spatial dependence of our computational accu-

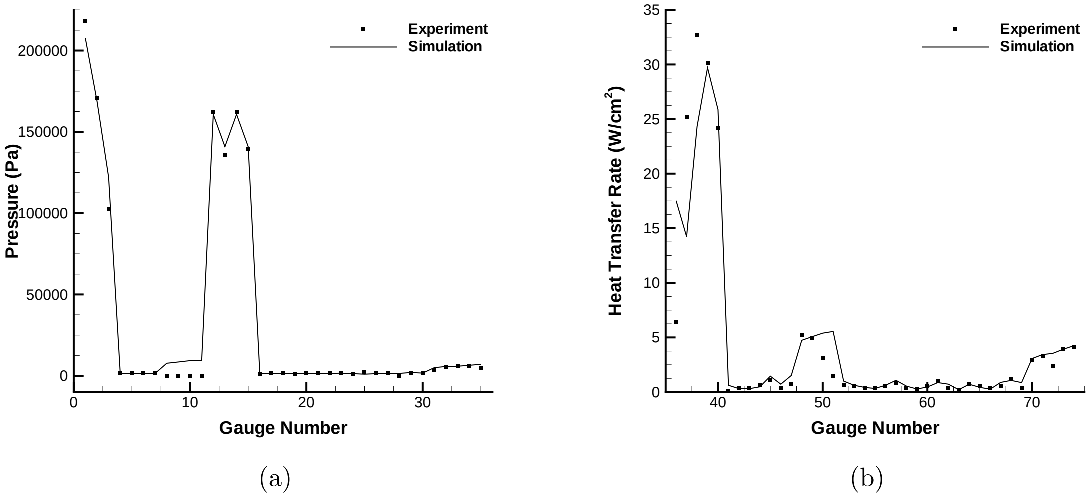

(a) (b)

Figure 6.7: Comparison of experimental and numerical measurements for Run 2. (a) Pressure, (b) Heat transfer rate.

racy. This is shown in Figures 6.8 and 6.9, which depict pressure and heat transfer comparisons for each ray of instrumentation. Here the computational results are denoted with a solid line and the experiment by symbols. The bars reflect the measured standard deviation of the flow at each location and therefore provide an indication of the variation and unsteadiness of the local flowfield. As the x-coordinate increases, we are moving from the shoulder toward the base; corresponding gauge numbers are shown for the first and final gauges in each ray.

Principally, as is evident from Figure 6.7 as well, we see very good agreement for both pressure and heat transfer. For the most part, the computation lies within one standard deviation of the experiment, and when even that fails the disagreement is often within a few percent. There are however a couple of points which do stand out. First, with pressure we see significant disagreement at gauges 25, 31, and 35 (corresponding to P27, P33, and P37). Each of these gauges is spatially surrounded by other gauges that perform well in the comparison, which raises the possibility that they are outliers, yet there is no indication from the experiment of malfunction. One may note however that both gauges 25 and 31 are located near the junction of the conical afterbody and flat base. The inability to accurately predict these locations may well be due to the sharp flow separation and interaction between the aftbody flow and the flow behind the sting. It's worth noting that, irrespective of the cause, the effects are localized to these gauges. Gauge 35 has indications of being an outlier due to its rather benign location in the windside acreage and the fact that it is surrounded by three other gauges which compare favorably with the experiment.

The most notable aspect of the heat transfer measurements is that the computation tends to overpredict results near separation points. This is particularly true for locations in which the flow is transitioning from the windside to the leeside, see for instance the $\phi = 90°$ ray. This seems to indicate an inability of the computational model to accommodate a rapid expansion of the flowfield, not unlike the frequently seen heat transfer spikes at the shoulders of capsule geometries. It is also indicative of the grid possibly being under-resolved near the separation points. Again, we note that this phenomenon is almost completely localized such that it has little or no impact on the gas subsequent to separation.

Finally, we may gain further insight into our numerical performance for this particular case by looking closer at the detailed transients of a few selected gauges. While we cannot expect to perfectly replicate transient phenomena in our simulations, we can reasonably compare frequencies and amplitudes of oscillation. For this purpose, we have run our simulations over a time period comparable to the flow time achieved in the experiment and extracted transient data along the $\phi = 0°$ ray.

The resulting comparisons for gauges [42 - 46] are shown in Figure 6.10. Note that increasing gauge number indicates movement from the shoulder toward the base of the capsule. Gauge 42 therefore reflects the state of the flow just subsequent to the strong expansion off the leeside shoulder. Here we see that the ability of the computation to correctly capture the amplitude and frequency of the flow is severely degraded. Interestingly, this does not detrimentally affect the time-averaged result. As we move away from the shoulder toward the base, we see a steady improvement in the simulations prediction of oscillation frequencies and amplitudes. There is however a slight bias toward overprediction near the base, a fact which is apparent in the time-averaged results of Figure 6.9. These results suggest that an additional local refinement of the computational mesh near the shoulder separation and wake/sting interaction may be necessary in order to accurately capture transient behavior in these regions. It is worth noting however that the discrepancies have a nearly negligible impact on the statistical results.

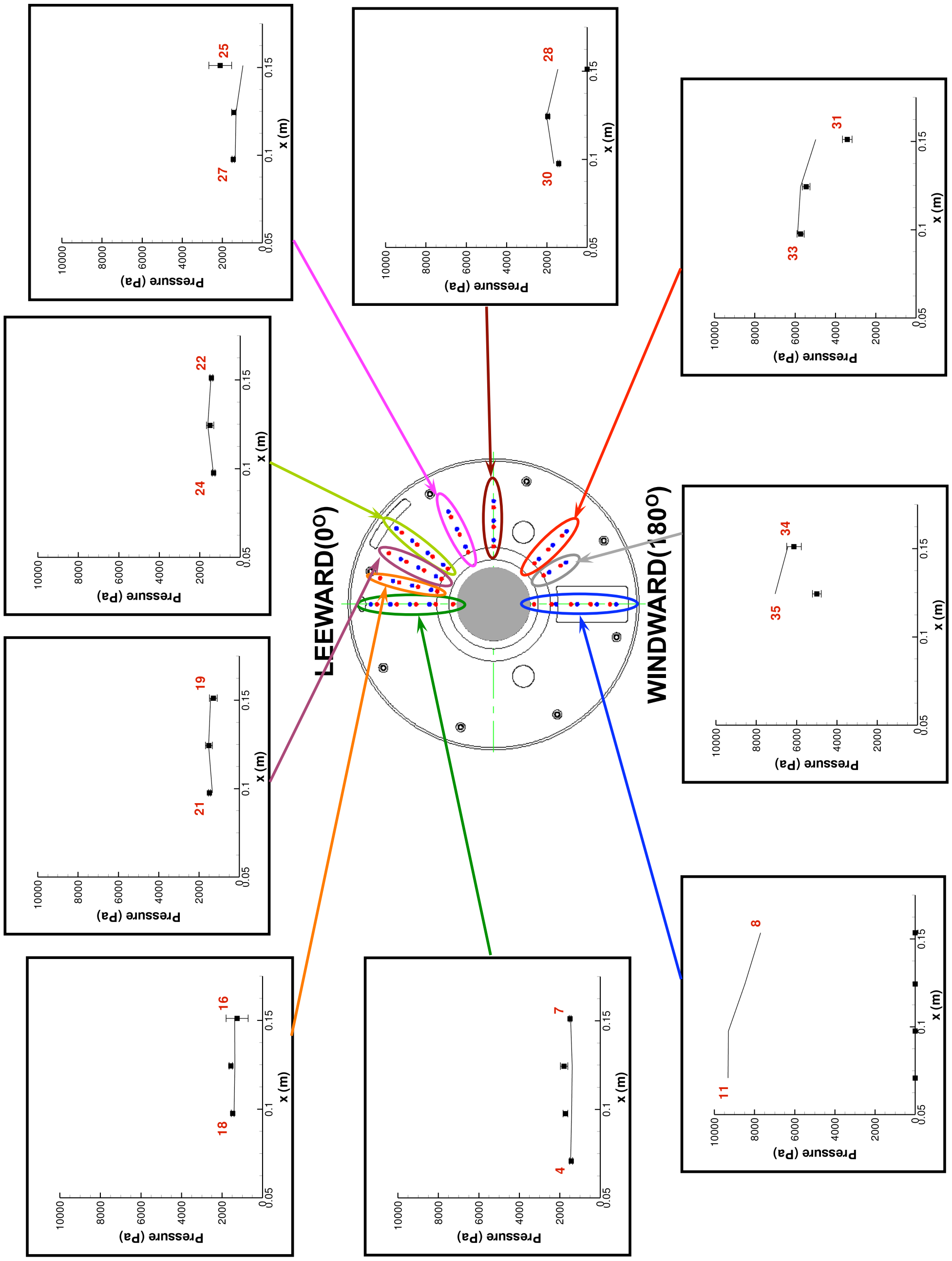

Figure 6.8: Comparison of experimental and numerical pressure measurements along instrument rays for Run 2. Symbols denote experiment, solid lines denote simulation.

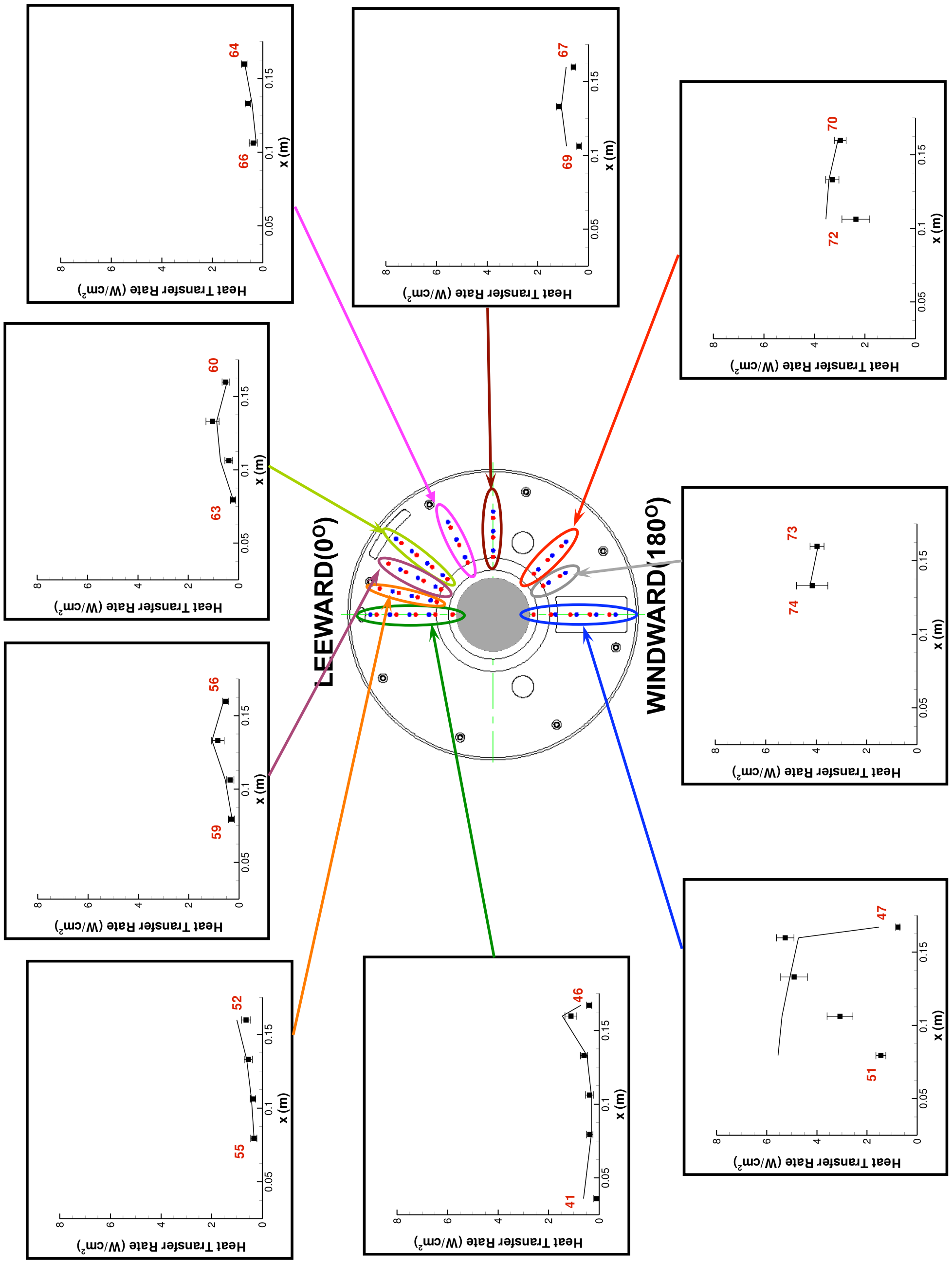

Figure 6.9: Comparison of experimental and numerical heat flux measurements along instrument rays for Run 2. Symbols denote experiment, solid lines denote simulation.

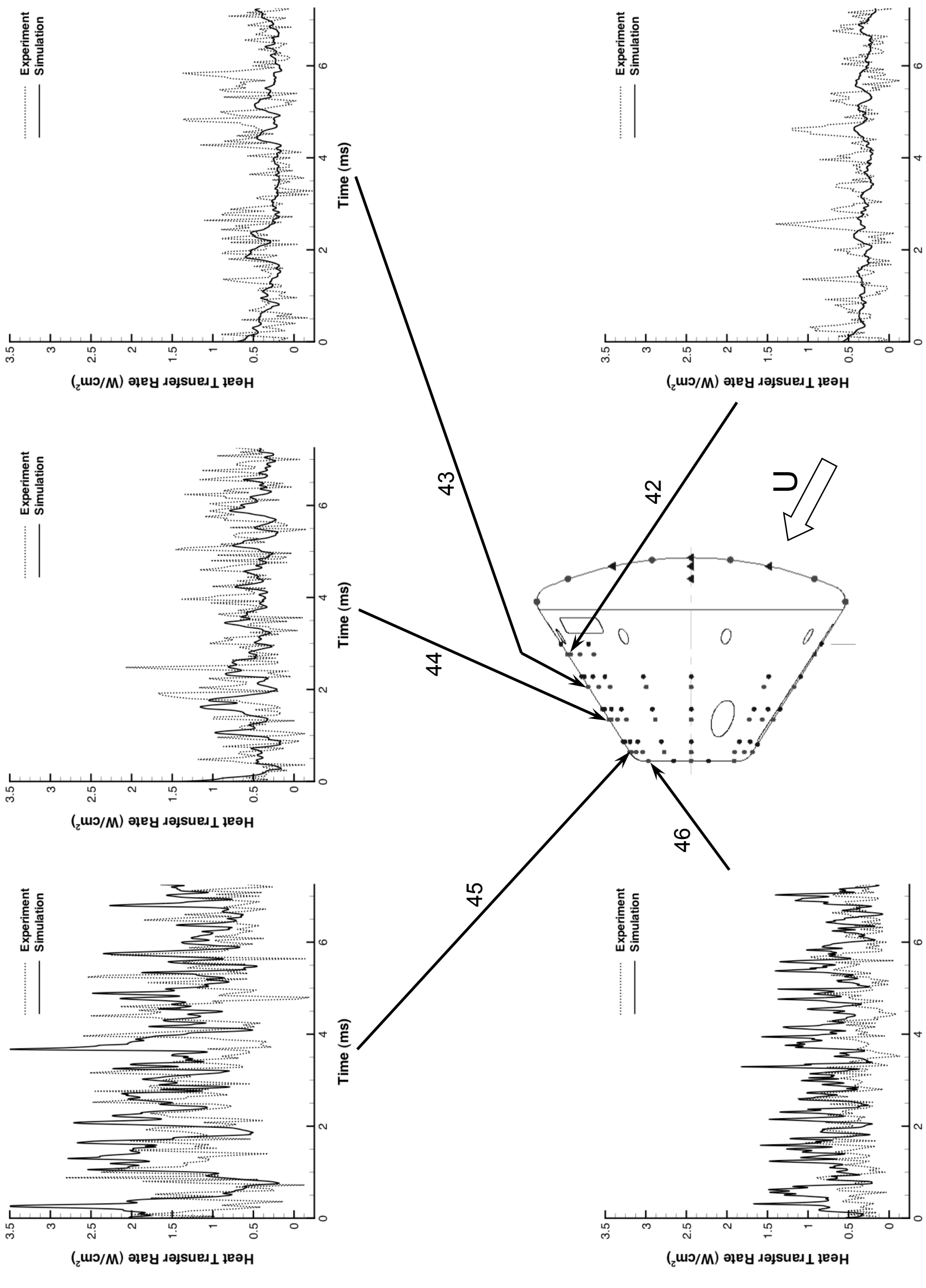

Figure 6.10: Comparison of CFD to experimental transient heat transfer along $\phi = 0°$ ray for Run 2.

6.3.5 DES v. RANS

As in our analysis of Reentry-F, we performed simulations of the Run 2 conditions utilizing the RANS turbulence model. Comparisons for both DES and RANS models are shown in Figure 6.11. As we expect, there is very little difference in predicted pressure between the two models because they are physically coupled to the Navier-Stokes equations through the viscous terms while pressure is principally an inviscid effect. In fact, with the current formulation, the *only* way in which pressure can be affected is indirectly as a result of balancing the momentum equations, i.e. changes in flow structure due to the action of eddy viscosity.

In contrast, the effects of the two models on heat transfer are more pronounced due to their essentially viscous nature. One can actually deduce from Figure 6.11(b) whether gauges are located in attached or separated flow regions by simply comparing the DES and RANS curves. In the attached regions of the forebody and windward aftbody, DES and RANS give nearly identical results, a consequence of RANS being a limiting case of DES under such conditions. Elsewhere, however, there is variance evident between the two methods. Significantly, we see that the predictive accuracy of the RANS model is degraded relative to DES, even on an identical, highly-refined mesh.

On a per-gauge basis, there is no discernible pattern of over- or under-prediction in the RANS model. Rather, the excessive dissipation introduced by the model simply creates an ‘alternative’ flow structure. Separation and reattachment lines are moved, and convection streamlines are dramatically altered to accommodate the more ‘viscous’ flow. For the capsule case (and indeed for all cases investigated during the course of this research), the result is that the RANS model tends to produce a much smoother flowfield with very little local fluctuation, while the DES model exhibits a much greater degree of disorder and unsteadiness. Analytically, this is precisely what we expect to occur because the DES simulation essentially amounts to transferring the bulk of modeling work from the approximate turbulence model to the exact Navier-Stokes equations. In other words, the success of DES in our simulations stems not so much from the model producing a more ‘correct’ value of eddy viscosity, but merely by the fact that it interferes minimally with the fidelity that Navier-Stokes already provides. (This is *not* to suggest that the particulars of the subgrid model are trivial; they certainly are not.)

Thus, the capsule surface is subjected to different levels and distribution of heating depending on which model one chooses. This observation is quantitatively verified in Figure 6.12 which depicts the simulated transient heat fluxes at gauge 45. In this figure, we have started the DES and RANS simulations from an identical initial condition and allowed them to evolve over a period of time while keeping the CFL number fixed. Note that the time scale has been truncated relative to Figure 6.10 in order to draw out distinctions in the resolved heat flux measurements.

First, after the initial ∼0.5 ms transient has passed, during which time the flow is adjusting to the models being switched on, it is apparent that the RANS simulation has a greatly diminished ability to resolve flow unsteadiness. Looking at the standard deviation (using the full time trace data as shown in Figure 6.10), we find that the magnitude relative to the experimentally measured mean is 52% for DES and only 0.64% for RANS. Thus the amplitude of fluctuation is reduced by nearly two orders of magnitude. The DES simulation, on the other hand, compares quite favorably to the experiment.

Second, the RANS simulation greatly overpredicts the experiment across nearly the entire flow time and so it fails to achieve even the correct mean heat flux. We compute the relative error of the mean heat flux for this case to be 30% and 156% for DES and RANS, respectively. The computed statistics for the experiment and both simulations at gauge 45 are summarized in Table 6.3. By integrating over all of the gauges located in the wake, we obtain total error estimates of 36% and 57% for DES and RANS, respectively. The reduction in total error for the RANS case is chiefly due to the inclusion of gauges located near the shoulder separation (like gauges 42 and 43 in Figure 6.10) where flow unsteadiness is fairly weak. In light of RANS being the most favored modeling approach employed in today's production CFD codes, we can surmise that the use of more sophisticated methods like DES, if applied during the design phase of an actual flight vehicle, could crucially impact development of an afterbody thermal protection system.

6.3.6 Flux Dissipation and Time-Accuracy

Finally, let us emphasize that nearly all of the preceding analysis has been predicated on comparisons with *statistical* data, i.e. mean, RMS, and standard deviation. By doing so, we necessarily circumvent notions of time-accuracy. It is clear, how-

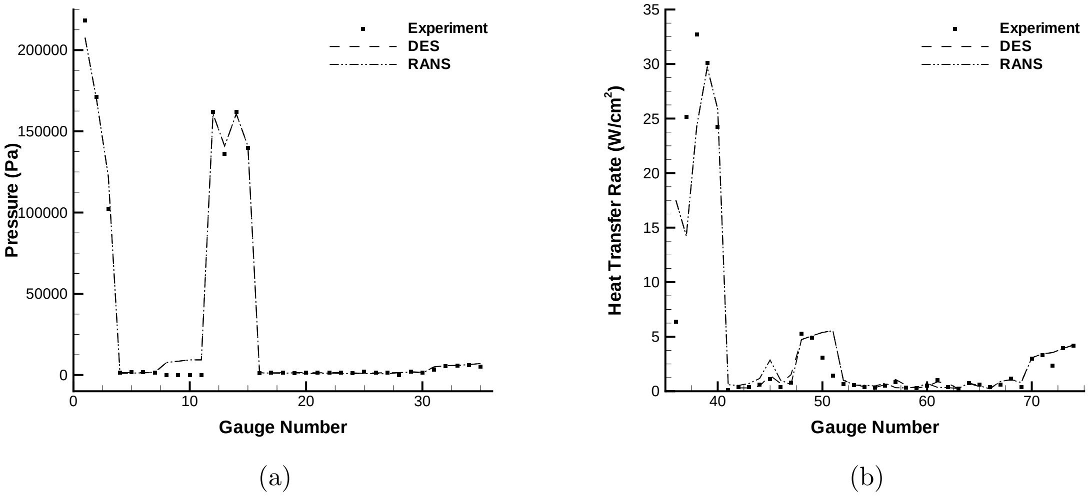

(a) (b)

Figure 6.11: Comparison of numerical measurements using DES and RANS models for Run 2. (a) Pressure, (b) Heat flux.

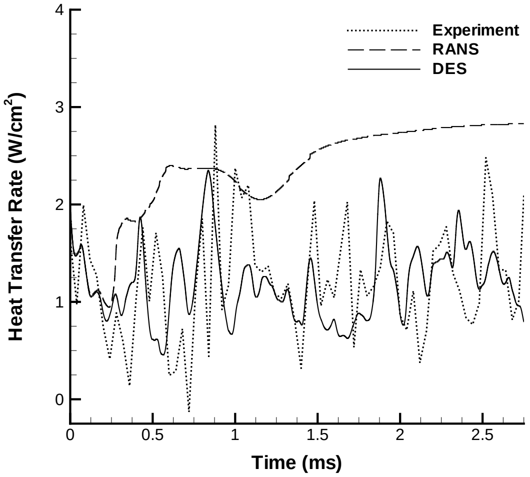

Figure 6.12: Heat flux transients from gauge 45 of Run 2 simulated with RANS and DES.

Table 6.3: Computed statistics for gauge 45 of Run 2.

	μ (W/cm^2)	σ	μ/μ_{exp}	σ/μ_{exp}
Experiment	1.1178	0.5962	1.0000	0.5334
DES	1.4509	0.5855	1.2980	0.5238
RANS	2.8601	0.0072	2.5587	0.0064

ever, that accuracy in a statistical sense does not imply transient accuracy. As an example, one could model the function $f(t) = \sin t$ as $\tilde{f}(t) = \sin 10t$ or $\tilde{f}(t) = 10 \sin t$ and still obtain the correct mean value of 0, while incorrectly predicting by factors of 10 the transient period and amplitude, respectively. We noted this phenomenon in Figure 6.10, where gauge 42 of the simulation clearly does not capture the same amplitude of fluctuation as seen in the experiment, yet it ultimately yields a reasonable estimate of mean heat flux.

Based on the results presented over the last three chapters, it can be argued that, with regard to our stated applications of interest (external, reentry-type flows), no further improvement on the numerical scheme's accuracy is necessary in order to produce accurate *statistical* results. That is to say, for these cases, a traditional 1$^{\text{st}}$ order in time, 2$^{\text{nd}}$ order in space discretization is sufficient when coupled with an adequate turbulence model and good CFD practices (grid refinement studies, time-step limiting). However, this may not hold true for cases which require that the transient processes be resolved.

To illustrate how the apparent limitations displayed in Figure 6.10 might be mitigated, we ran the same case incorporating the low-dissipation and dual-time schemes discussed in Chapter 3. The results are depicted in Figure 6.13. Recall for this case that the Steger-Warming scheme failed to capture correctly the amplitude and frequency of the transient heat flux. By comparison, Subbareddy's low-dissipation scheme does a remarkable job of recovering amplitudes comparable to those seen in the experiment. By eliminating unnecessary numerical dissipation, the scheme also allows us to take advantage of the simulation's temporal resolution. It is thus capable of resolving transient flow features on a smaller scale than even that captured in the experiment. While this does not conclusively demonstrate the performance benefits

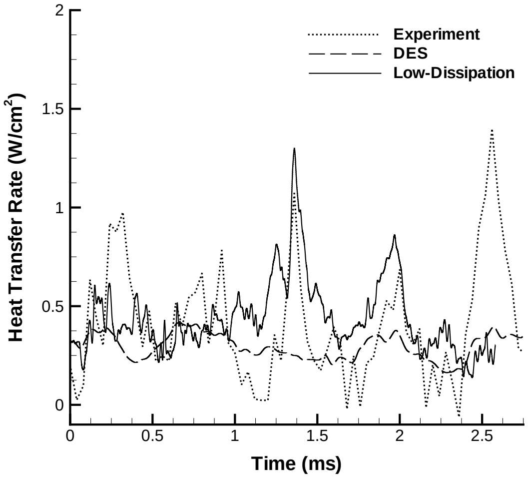

Figure 6.13: Heat flux transients from gauge 42 of Run 2 simulated with the original Steger-Warming scheme and the low-dissipation scheme of Subbareddy.

of the scheme, it does show how simulations are critically impacted by the choice of numerics, notwithstanding their level of physical modeling fidelity.

Chapter 7

Summary and Conclusions

7.1 Summary

This thesis presented and discussed the broad challenges surrounding the simulation of high-speed, unsteady wake flows. We were motivated by the desire to limit the impact of current modeling uncertainty on the design of thermal protection systems for reentry vehicles. Prior studies have depended on traditional methodologies, largely unchanged for two decades, and they consequently have exhibited little success outside of quasi-steady, laminar wake flows. Our objective was to develop a new methodology, rooted within these traditions, which would also incorporate some of the advances made in low-speed, unsteady flow analysis.

In Chapters 2 and 3, we developed the mathematical framework describing the equations of fluid motion and how to solve them. The traditional Navier-Stokes equations form the basis of this framework, with additional source terms to account for nonequilibrium thermochemical behavior. Recent advances in modeling of laminar transport coefficients and chemical equilibrium constants were presented as a means to improve predictive accuracy over the commonly used methods exemplified in Nompelis (2004) and many other sources. This approach was deemed to be sufficient for modeling laminar flows. A key development was made for transitional and turbulent flows, for which we adopted the DES methodology advanced by Spalart et al. (1997). This approach had received very little attention in the hypersonics community despite being widely used in the analysis of low-speed and even some supersonic flows. The remainder of the thesis was devoted to validating our approach at higher Mach numbers, with the ultimate aim being the accurate simulation of turbulent, reentry flows.

In Chapter 4, we addressed the basic issue of verification. That is, we applied our methodology to a previously analyzed flow regime in order to assess whether our implementation was consistent with the mathematical framework and, qualitatively, with the observations of prior studies. The MSL parachute system was chosen for analysis because: (1) It is a very challenging problem of practical interest to the aerospace community, and (2) There exists a small amount of experimental data by which we can also validate our results.

A series of tests were run in capsule-only, canopy-only, and capsule-with-canopy configurations. In a full-scale test of the entire parachute system at flight conditions, we were able to verify numerically the commonly observed phenomenon of performance degradation near Mach 2. This was manifested by a decrease in drag and apparent increase in flow instability due to the interaction of the capsule wake with the canopy bow shock. This phenomenon was addressed in more depth by comparing to several scale wind tunnel experiments. First, we examined the structure of the turbulent capsule wake and found favorable comparison between the new DES method and experimental PIV. Next, we looked at the canopy-only configuration to validate our ability to capture the bow shock and canopy drag. In all cases, the deviation from experimentally measured values never exceeded 1.5%. This test also demonstrated, by correctly predicting a stationary bow shock, that the DES methodology was not generating any *spurious* flow instability. Finally, with the entire scaled configuration, we examined the mechanism of instability that drives the ‘panting’ phenomenon commonly seen in supersonic parachutes. We observed in our simulations a repeating pattern of over- and under-pressurization driven by the unsteady capsule wake feeding into the canopy bow shock. Indeed, this fact was implied by the compound results of the capsule- and canopy-only configurations. Upon closer inspection, it was revealed that the unsteady momentum deficit of the capsule wake essentially causes the shock standoff distance to increase, as one would expect for any body subjected to a lower freestream velocity. Consequently, the region behind the shock becomes under-pressurized and the high-pressure fluid within the canopy is then driven to escape around the canopy edges. In order to maintain balance of the system, the bow shock collapses inward, thus re-pressurizing the canopy and beginning the cycle anew. Through this process, we were able to verify that portions of the parachute band were actually subjected to *inward pointing* pressure gradients, thus providing a plausible explanation for the riffling of parachute bands and attendant reduction in effective drag area that occurs at supersonic speeds.

In Chapter 5, we studied the performance of our method at reentry flight conditions using data from the Reentry-F experiment. The 70 and 80 kft trajectory points were chosen for analysis and a systematic study of experimental uncertainties derived from the original reports was presented. For the 80 kft case, which was initially assumed to be at a total angle of attack of $\eta = 0°$, DES was found to considerably improve predictions over a standard RANS model, yet neither simulation could address the apparent disagreement of the two $r = 20$ cm gauges seen in the flight data. The case was then re-run using the measured pitch and yaw angles ($\eta = 0.32°$) and this was found to account for the discrepancy. Noting the sensitivity of the slender cone's base flow to the vehicle orientation, the 70 kft case was simulated using the measured pitch and yaw angles yet the experimental agreement was still poor. During a review of the post-flight analysis reports, it was found that thermal distortion effects could account for a nearly 100% uncertainty in the reported total angle of attack. A simulation accounting for this effect demonstrated that it could plausibly explain the poor experimental agreement.

In Chapter 6, we turned our attention to the spherical capsule experiments of MacLean et al. (2008) in order to (1) obviate concerns that were raised concerning ambiguity of the Reentry-F flight data, and (2) extend our analysis to realistic reentry vehicle geometries. Three test runs were chosen for analysis, corresponding to nominally laminar, transitional, and turbulent conditions. The laminar case displayed uniformly excellent agreement with the experiment, with the exception of the forebody pressure gauges. This was attributed to a possible calibration error during testing. The transitional case posed some difficulty for our simulation procedure due to inadequate knowledge of the boundary layer transition front. The case was instead run twice, fully laminar and fully turbulent. The two simulations bounded the experiment nicely, suggesting that inclusion of an appropriate transition model would be sufficient to adequately simulate the flow. In the turbulent case, good agreement was obtained using the fully turbulent DES model. A more detailed analysis was then presented to shed light on the relationship between flow structure and

DES performance. In particular, the model's performance was found to deteriorate in the vicinity of strong expansions, such as those seen near the vehicle shoulder and base. This limitation was also found to be fairly localized and had little discernible impact on gauges located downstream of the separation. Furthermore, DES simulations showed exceptional improvement over the RANS model for this case. Total error integrated over the separated flow gauges was reduced from 57% for RANS to 36% for DES. Inspection of the heat flux transients showed that the RANS model nearly eliminated the inherent unsteadiness of the flow while the DES model compared favorably with experiment. Finally, we examined the effects of numerics on the solutions by incorporating a low dissipation flux scheme and 2$^{\text{nd}}$ order time accuracy. Use of these methods was found to qualitatively enhance the simulation's ability to resolve transient characteristics of the flow and could provide a useful avenue for future improvements of our methodology.

7.2 Conclusions

This study demonstrated that currently available computational methods are capable of accurately simulating unsteady, separated flows at high Mach numbers. In general, the most critical barrier to overcome in a simulation is dissipation, whether physical or numerical. From a physical standpoint, it is easily demonstrated (and fairly well-documented in the literature) that classic RANS models produce excessive turbulent dissipation which then result in unrealistic wake structure and, therefore, unrealistic predictions of base pressure and heat flux. The effects of numerical dissipation, on the other hand, are generally felt at the discretization scale and act to damp out small-scale fluctuations which could adversely affect applications in which transient resolution of the flow is important.

We adopted the detached eddy simulation model in order to address the issue of excessive turbulent dissipation. The DES model provided a clear improvement over RANS in all cases presented here. The main caveat is that DES requires a fairly substantial increase in spatial resolution in order to achieve the desired modeling effect. Thus, as with all simulations but perhaps even more so here, one should always conduct a careful grid convergence study to ensure that the model is performing adequately. Additionally, one must always be cognizant of how the grid points are distributed. For example, there is little benefit in resolving the wake if the separation is captured so poorly that the shape and extent of the wake are inaccurate. Similarly, the version of DES used here is well-known to behave poorly if the RANS/LES transition occurs in the boundary layer. More recent versions have been proposed [see Spalart et al. (2006)] which may eliminate this problem, and we recommend that others consider their use in future studies.

For the external, reentry flows considered here, a standard 1^{st} order in time, 2^{nd} order in space Steger-Warming scheme was numerically sufficient to accurately model each of the experimental datasets. Nevertheless, we note that the primary method of analysis depended on statistically measured quantities which obfuscates transient characteristics of the simulations. Indeed, in our examination of the spherical capsule, we saw that frequencies and amplitudes were greatly diminished in the vicinity of flow separations, yet the resulting statistics still agreed well with experiment. It is therefore recommended that future studies on problems outside the scope of interest here continue to investigate the influence of time accuracy and flux dissipation. Improvements in these areas may prove critical for more demanding applications. We believe the dual-time and low-dissipation schemes discussed in Chapter 3 to be very promising candidates for enhancing our methodology's effectiveness.

Bibliography

Arranged by subject and date of publication:

General

Millikan, R. C. and D. R. White. 1963. *Systematics of Vibrational Relaxation*, Journal of Chemical Physics **39**, 3209–3213.

Pallone, A.J., J.I. Erdos, J. Eckerman, and W. McKay. 1963. *Hypersonic Laminar Wakes and Transition Studies*, AIAA Paper **63-171**.

Lien, H., J.I. Erdos, and A.J. Pallone. 1963. *Nonequilibrium Wakes with Laminar and Turbulent Transport*, AIAA Paper **63-447**.

Zeiberg, S. L. and G. D. Bleich. 1964. *Finite-Difference Calculation of Hypersonic Wakes*, AIAA Journal **2**, no. 8, 1396–1402.

Berger, S. A. 1971. *Laminar Wakes*, American Elsevier Publishing Company, Inc.

Bulmer, B. 1975. *Study of Base Pressure in Laminar Hypersonic Flow: Re-entry Flight Measurements*, AIAA Journal **13**, no. 10, 1340–1348.

Sod, G. A. 1978. *A Survey of Several Finite Difference Methods for Systems of Nonlinear Hyperbolic Conservation Laws*, Journal of Computational Physics **27**, 1–31.

Steger, J. L. and R. F. Warming. 1981. *Flux Vector Splitting of the Inviscid Gasdynamic Equations with Application to Finite-Difference Methods*, Journal of Computational Physics **40**, 263–293.

Vincenti, W. G. and C. H. Kruger. 1982. *Introduction to Physical Gas Dynamics*, Krieger Publishing Comapny.

MacCormack, R. W. 1985. *Current Status of Numerical Solutions of the Navier-Stokes Equations*, AIAA Paper **1985-0032**.

Lee, J-H. 1985. *Basic Governing Equations for the Flight Regimes of Aeroassisted Orbital Transfer Vehicles*, Progress in Aeronautics and Astronautics **96**, 3–53.

Park, C. 1988. *Assessment of a Two-Temperature Kinetic Model for Dissociating and Weakly Ionizing Nitrogen*, Journal of Thermophysics and Heat Transfer **2**, no. 1, 8–16.

Candler, G. V. 1988. *The Computation of Weakly Ionized Hypersonic Flows in Thermo-chemical Nonequilibrium*, Ph.D. Thesis, Stanford University.

Park, C. 1989. *Assessment of Two-Temperature Kinetic Model for Ionizing Air*, Journal of Thermophysics and Heat Transfer **3**, no. 3, 233-244.

MacCormack, R. W. and G. V. Candler. 1989. *The Solution of the Navier-Stokes Equations Using Gauss-Seidel Line Relaxation*, Computers and Fluids **17**, no. 1, 135–150.

Gnoffo, P. A., R. N. Gupta, and J. L. Shinn. 1989. *Conservation Equations and Physical Models for Hypersonic Air Flows in Thermal and Chemical Nonequilibrium*, NASA **TP 2867**.

Yee, H. C. 1989. *A Class of High-Resolution Explicit and Implicit Shock-Capturing Methods*, NASA **TM 101088**.

Gokcen, T. 1989. *Computation of Hypersonic Low-density Flows with Thermochemical Nonequilibrium*, Ph.D. Thesis, Stanford University.

Marvin, J.G. and T.J. Coakley. 1989. *Turbulence Modeling for Hypersonic Flows*, NASA **TM 101079**.

Park, C. 1990. *Nonequilbrium Hypersonic Aerothermodynamics*, John Wiley and Sons.

Gnoffo, P. A. 1990. *A Code Calibration Program in Support of the Aeroassist Flight Experiment*, Journal of Spacecraft and Rockets **27**, no. 2, 131–142.

Gupta, R. N., J. M. Yos, R. A. Thompson, and K-P. Lee. 1990. *A Review of Reaction Rates and Thermodynamic and Transport Properties for an 11-species Air Model for Chemical and Thermal Nonequilibrium Calculations to 30,000 K*, NASA **RP 1232**.

Gnoffo, P. A., J. M. Price, and R. D. Braun. 1991. *On the Computation of Near Wake, Aerobrake Flowfields*, AIAA Paper **1991-1371**.

Venkatapathy, E., G. Palmer, and D. K. Prabhu. 1991. *AFE Base Flow Computations*, AIAA Paper **1991-1372**.

Candler, G. V. and R. W. MacCormack. 1991. *Computation of Weakly Ionized Hypersonic Flows in Thermochemical Nonequilbrium*, Journal of Thermophysics and Heat Transfer **5**, no. 3, 266–273.

Ramshaw, J. D. and C. H. Chang. 1991. *Ambipolar Diffusion in Multicomponent Plasmas*, Plasma Chemistry and Plasma Processing **11**, no. 3, 395–403.

Spalart, P. R. and S. R. Allmaras. 1992. *A One-Equation Turbulence Model for Aerodynamic Flows*, AIAA Paper **1992-0439**.

Conti, R. J. and R. W. MacCormack. 1992. *Navier-Stokes Computation of Hypersonic Near Wakes with Foreign Gas Injection*, AIAA Paper **1992-0838**.

Gordon, S. and B. J. McBride. 1994. *Computer Program for Calculation of Complex Chemical Equilibrium Compositions and Applications*, NASA **RP 1311**.

Horvath, T. J., C. B. McGinley, and K. Hannemann. 1996. *Blunt Body Near-Wake Flow Field at Mach 6*, AIAA Paper **1996-1935**.

Blaisdell, G. A., E. T. Spyropoulos, and J. H. Qin. 1996. *The Effect of the Formulation of Nonlinear Terms on Aliasing Errors in Spectral Methods*, Applied Numerical Mathematics **21**, 207–219.

Rumsey, C. L., M. D. Sanetrik, R. T. Biedron, N. D. Melson, and E. B. Parlette. 1996. *Efficiency and Accuracy of Time-Accurate Turbulent Navier-Stokes Computations*, Computers and Fluids **25**, no. 2, 217–236.

Wright, M. J., G. V. Candler, and M. Prampolini. 1996. *Data-Parallel Lower-Upper Relaxation Method for the Navier-Stokes Equations*, AIAA Journal **34**, no. 7, 1371–1377.

Wright, M. J. 1997. *A Family of Data-Parallel Relaxation Methods for the Navier-Stokes Equations*, Ph.D. Thesis, University of Minnesota.

Olejniczak, J. 1997. *Computational and Experimental Study of Nonequilibrium Chemistry in Hypersonic Flows*, Ph.D. Thesis, University of Minnesota.

Horvath, T. J. and K. Hannemann. 1997. *Blunt Body Near-Wake Flow Field at Mach 10*, AIAA Paper **1997-0986**.

Spalart, P. R., W-H. Jou, M. Strelets, and S. R. Allmaras. 1997. *Comments on the Feasibility of LES for Wings and on a Hybrid RANS/LES Approach*, AFOSR International Conference on DNS/LES.

Holden, M. S., J. K. Harvey, I. D. Boyd, and T. J. Horvath. 1997. *Experimental and Computational Studies of the Flow Over a Sting Mounted Planetary Probe Configuration*, AIAA Paper **1997-0768**.

Wright, M. J., G. V. Candler, and D. Bose. 1998. *Data-Parallel Line Relaxation Method for the Navier-Stokes Equations*, AIAA Journal **36**, no. 9, 1603–1609.

Shur, M., P. R. Spalart, M. Strelets, and A. Travin. 1999. *Detached Eddy Simulation of an Airfoil at High Angle of Attack*, 4th Int. Symp. Eng. Turb. Modeling and Measurements.

Ducros, F., V. Ferrand, F. Nicoud, C. Weber, D. Darracq, C. Gacherieu, and T. Poinsot. 1999. *Large-Eddy Simulation of the Shock/Turbulence Interaction*, Journal of Computational Physics **152**, 517–549.

Gordon, S. and B. J. McBride. 1999. *Thermodynamic Data to 20,000 K for Monatomic Gases*, NASA **TP 1999-208523**.

Ducros, F., F. Laporte, T. Souleres, V. Guinot, P. Moinat, and B. Caruelle. 2000. *High-Order Fluxes for Conservative Skew-Symmetric-like Schemes in Structured Meshes: Application to Compressible Flows*, Journal of Computational Physics **161**, 114–139.

Catris, S. and B. Aupoix. 2000. *Density Corrections for Turbulence Models*, Aerospace Science and Technology **4**, 1–11.

Zehe, M. J., S. Gordon, and B. J. McBride. 2002. *CAP: A Computer Code for Generating Tabular Thermodynamic Functions from NASA Lewis Coefficients*, NASA **TP 2001-210959/REV1**.

Strelets, M. 2001. *Detached Eddy Simulation of Massively Separated Flows*, AIAA Paper **2001-0879**.

Spalart, P. R. 2001. *Young Person's Guide to Detached Eddy Simulation Grids*, NASA **CR-2001-211032**.

Leveque, R. J. 2002. *Finite Volume Methods for Hyperbolic Problems*, Cambridge Texts in Applied Mathematics.

Mavriplis, D. J. 2003. *Revisiting the Least-squares Procedure for Gradient Reconstruction on Unstructured Meshes*, NASA **CR-2003-212683**.

Kee, R. J., M. E. Coltrin, and P. Glarborg. 2003. *Chemically Reacting Flow: Theory and Practice*, John Wiley and Sons.

Pope, S. B. 2003. *Turbulent Flows*, Cambridge University Press.

Sinha, K., M. Barnhardt, and G. V. Candler. 2004. *Detached Eddy Simulation of Hypersonic Base Flows with Application to FIRE II Experiments*, AIAA Paper **2004-2633**.

Nompelis, I. N., T. Drayna, and G. V. Candler. 2004. *Development of a Hybrid Unstructured Implicit Solver for the Simulation of Reacting Flows Over Complex Geometries*, AIAA Paper **2004-2227**.

Gnoffo, P. A. and J. A. White. 2004. *Computational Aerothermodynamic Simulation Issues on Unstructured Grids*, AIAA Paper **2004-2371**.

Levin, E. and M. J. Wright. 2004. *Collision Integrals for Ion-Neutral Interactions of Nitrogen and Oxygen*, Journal of Thermophysics and Heat Transfer **18**, no. 1, 143–147.

Nompelis, I. N. 2004. *Computational Study of Hypersonic Double-Cone Experiments for Code Validation*, Ph.D. Thesis, University of Minnesota.

Nompelis, I. N., T. Drayna, and G. V. Candler. 2005. *A Parallel Unstructured Implicit Solver for Hypersonic Reacting Flow Simulations*, AIAA Paper **2005-4867**.

Barnhardt, M. and G. V. Candler. 2005. *Detached Eddy Simulation of Hypersonic Base Flows: Application to Titan Entry*, 1st JANNAF Meeting of Spacecraft Propulsion Subcommittee.

Wright, M. J., F. S. Milos, and P. Tran. 2005. *Survey of Afterbody Aeroheating Flight Data for Planetary Probe Thermal Protection System Design*, AIAA Paper **2005-4815**.

Edquist, K. T. 2005. *Afterbody Heating Predictions for a Mars Science Laboratory Entry Vehicle*, AIAA Paper **2005-4817**.

Wright, M. J., D. Bose, G. E. Palmer, and E. Levin. 2005. *Recommended Collision Integrals for Transport Property Computations, Part 1: Air Species*, AIAA Journal **43**, no. 12, 2558–2564.

Subbareddy, P. and G. V. Candler. 2005. *Numerical Investigations of Supersonic Base Flows Using DES*, AIAA Paper **2005-0886**.

Danehy, P. M., J. A. Wilkes, D. W. Alderfer, S. B. Jones, A. W. Robbins, D. P. Patry, and R. J. Schwartz. 2006. *Planar Laser-Induced Fluorescence (PLIF) Investigation of Hypersonic Flowfields in a Mach 10 Wind Tunnel*, AIAA Paper **2006-3442**.

Wright, M. J., D. K. Prabhu, and E. R. Martinez. 2006. *Analysis of Afterbody Heating Rates on the Apollo Command Modules, Part 1: AS-202*, Journal of Thermophysics and Heat Transfer **20**, no. 1, 16–30.

Edquist, K. T., M. J. Wright, and G. A. Allen. 2006. *Viking Afterbody Heating Computations and Comparisons to Flight Data*, AIAA Paper **2006-0386**.

Spalart, P. R., S. Deck, M. L. Shur, K. D. Squires, M. Strelets, and A. Travin. 2006. *A New Version of Detached-Eddy Simulation, Resistant to Ambiguous Grid Densities*, Theoretical and Computational Fluid Dynamics **20**, no. 3, 181–195.

Candler, G. V., M. Barnhardt, T. Drayna, I. N. Nompelis, D. M. Peterson, and P. Subbareddy. 2007. *Unstructured Grid Approaches for Accurate Aeroheating Simulations*, AIAA Paper **2007-3959**.

Subbareddy, P. 2007. *Stable Low-Dissipation Schemes for Turbulent Compressible Flows*, Ph.D. Thesis, University of Minnesota.

Subbareddy, P. and G. V. Candler. 2009. *A Fully Discrete, Kinetic Energy Consistent Finite-Volume Scheme for Compressible Flows*, Journal of Computational Physics **228**, 1347–1364.

Mars Science Laboratory

Lingard, J. S. and G. Darley. 2005. *Simulation of Parachute Fluid Structure Interaction in Supersonic Flow*, AIAA Paper **2005-1607**.

Sengupta, A. 2007a. *Overview of the Mars Science Laboratory Parachute Decelerator System*, AIAA Paper **2007-2578**.

______. 2007b. *Supersonic Delta Qualification by Analysis Program for the Mars Science Laboratory Parachute Decelerator System*, AIAA Paper **2007-2542**.

Barnhardt, M., T. Drayna, I. N. Nompelis, G. V. Candler, and W. Garrard. 2007. *Detached Eddy Simulations of the MSL Parachute at Supersonic Conditions*, AIAA Paper **2007-2529**.

Sengupta, A. 2008. *Results from the Mars Science Laboratory Parachute Decelerator System Supersonic Qualification Program*, 2008 IEEE Aerospace Conference.

Gidzak, V., M. Barnhardt, T. Drayna, I. N. Nompelis, G. V. Candler, and W. Garrard. 2008. *Detached Eddy Simulations of the MSL Parachute at Supersonic Conditions*, AIAA Paper **2008-6910**.

Reentry-F

1967. *Reentry F Turbulent Heat Experiment Familiarization Manual*, NASA **CR 66501**.

Rumsey, C. B., H. S. Carter, E. C. Hastings, J. L. Raper, and E. V. Zoby. 1969. *Initial Results from Flight Measurements of Turbulent Heat Transfer and Boundary-Layer Transition at Local Mach Numbers Near 15 (Reentry F)*, NASA **TM X-1856**.

Woodbury, G. E. and W. D. Morris. 1970. *Angle-of-Attack Analysis of a Spinning Slender Cone with Slight Aerodynamic and Mass Asymmetries (reentry F)*, NASA **TN D-5948**.

Wright, R. L. and E. V. Zoby. 1971. *Flight Measurements of Boundary-Layer Transition on a 5° Half-Angle Cone at a Free-stream Mach Number of 20 (Reentry F)*, NASA **TM X-2253**.

Howard, F. G. 1971. *Thermal Analysis Methods and Basic Heat-Transfer Data for a Turbulent Heating Flight Experiment at Mach 20 (Reentry F)*, NASA **TM X-2282**.

Carter, H. S., J. L. Raper, W. F. Hinson, and W. D. Morris. 1971. *Basic Measurements from a Turbulent Heating Flight Experiment on a 5° Half-Angle Cone at Mach 20 (Reentry F)*, NASA **TM X-2308**.

Alley, V. L. and R. J. Guilotte. 1971. *Postflight Analysis of Thermal Distortions of the Reentry F Spacecraft*, NASA **TM X-2250**.

Stainback, P. C., C. B. Johnson, L. R. Boney, and K. C. Wicker. 1972. *A Comparison of Theoretical Predictions and Heat-Transfer Measurements for a Flight Experiment at Mach 20 (Reentry F)*, NASA **TM X-2560**.

Johnson, C. B., P. C. Stainback, K. C. Wicker, and L. R. Boney. 1972. *Boundary-Layer Edge Conditions and Transition Reynolds Number Data for a Flight Test at Mach 20 (Reentry F)*, NASA **TM X-2584**.

Dillon, J. L. and H. S. Carter. 1972. *Analysis of Base Pressure and Base Heating on a* 5° *Half-Angle Cone in Free Flight Near Mach 20 (Reentry F)*, NASA **TM X-2468**.

Wood, W. A., C. J. Riley, and F. M. Cheatwood. 1997. *Reentry F Flowfield Solutions at 80,000 ft*, NASA **TM 112856**.

Brown, J. L. 2002. *Turbulence Model Validation for Hypersonic Flows*, AIAA Paper **2002-3308**.

Malik, M. R. 2003. *Hypersonic Flight Transition Data Analysis Using Parabolized Stability Equations with Chemistry Effects*, Journal of Spacecraft and Rockets **40**, no. 3, 332–344.

Lin, T. C., L. K. Sproul, M. Kim, M. Olmos, and H. Feiz. 2006. *Hypersonic Reentry Vehicle Wake Flow Fields at Angle of Attack*, AIAA Paper **2006-0582**.

Barnhardt, M. and G. V. Candler. 2006. *Detached Eddy Simulation of Hypersonic Base Flows During Atmospheric Entry*, AIAA Paper **2006-3575**.

______. 2008. *Detached Eddy Simulation of the Reentry-F Flight Experiment*, AIAA Journal, under review.

CUBRC Spherical Capsule Tests

MacLean, M., E. Mundy, and R. Parker. 2008. *Year 1 Summary Report for Study of Wake Flows on Capsule Bodies*, unpublished.

Holden, M., T. Wadhams, and M. MacLean. 2008. *Experimental Studies in the LENS Supersonic and Hypersonic Tunnels for Hypervelocity Vehicle Performance and Code Validation*, AIAA Paper **2008-2505**.

MacLean, M., E. Mundy, T. Wadhams, M. Holden, M. Barnhardt, and G. V. Candler. 2009. *Experimental and Numerical Study of Laminar and Turbulent Base Flow on a Spherical Capsule*, AIAA Paper **2009-0783**.

Appendix A

Model Parameters

Table A.1: Species formation enthalpies.

Species	h_s° (J/kg)
N_2	0.0
O_2	0.0
NO	2.996123×10^6
N	3.362161×10^7
O	1.542000×10^7

Table A.2: Characteristic vibrational temperatures.

Species	θ_{vs} (K)
N_2	3395
O_2	2239
NO	2817

Table A.3: Coefficients for the Blottner viscosity model.

Species	A_s	B_s	C_s
Air	0.0268142	0.3177838	-11.3155513
N_2	0.0268142	0.3177838	-11.3155513
O_2	0.0449290	-0.0826158	-9.2019475
NO	0.0436378	-0.0335511	-9.5767430
N	0.0115572	0.6031679	-12.4327495
O	0.0203144	0.4294404	-11.6031403

Table A.4: Constant parameters used in the Spalart-Allmaras turbulence model.

Parameter	Value
σ	$\frac{2}{3}$
κ	0.41
c_{b1}	0.1355
c_{b2}	0.6220
c_{w1}	$\frac{c_{b1}}{\kappa^2} + \frac{1+c_{b2}}{\sigma}$
c_{w2}	0.3
c_{w3}	2
c_{v1}	7.1

Table A.5: Arrhenius coefficients for forward reaction rates (Park, 1990).

Reaction	C_{f_m} (for each collision partner)			η_m	θ_m
	N_2, O_2	NO	N, O		
1	7.00×10^{18}	7.00×10^{18}	3.00×10^{19}	-1.60	113200
2	2.00×10^{18}	2.00×10^{18}	1.00×10^{19}	-1.50	59500
3	5.00×10^{12}	1.10×10^{14}	1.10×10^{14}	0.00	75500
4			6.40×10^{14}	-1.00	38400
5			8.40×10^{9}	0.00	19400

Table A.6: Park curve fit parameters for computing K_{c_m} (Park, 1990).

Reaction	C_m	A_{1m}	A_{2m}	A_{3m}	A_{4m}	A_{5m}
1	1000	1.606000	1.57320	1.39230	-11.5330	-0.004543
2	1000	0.641830	2.42530	1.90260	-6.62770	0.035151
3	1000	0.638170	0.68189	0.66336	-7.57730	-0.011025
4	1	0.967940	0.89131	0.72910	-3.95550	0.006488
5	1	-0.003732	-1.74340	-1.23940	-0.94952	-0.046182

Appendix B

Gupta-Yos Transport Model

In Chapter 2 we presented the transport model of Gupta et al. (1990) as an alternative to the more simplistic methods used in the course of this work. In this section, we complete our presentation of the model by providing definitions for α_{ij} and $\Delta_{ij}^{(l)}$.

The Gupta-Yos model provides the following expressions for mass, momentum, and energy transport coefficients

$$\begin{aligned} D_{ij} =& \frac{kT}{p\Delta_{ij}^{(1)}} \\ \mu =& \frac{1}{N_A}\sum_i \left(\frac{M_i X_i}{\sum_j X_j \Delta_{ij}^{(2)}}\right) \\ \kappa =& \frac{15}{4}k\sum_i \left(\frac{X_i}{\sum_j \alpha_{ij} X_j \Delta_{ij}^{(2)}}\right) + \frac{1}{N_A}\sum_i \left(\frac{C_{\mathrm{p}_i}^{(int)} M_i X_i}{\sum_j X_j \Delta_{ij}^{(1)}}\right) \end{aligned}$$

The quantities, $\Delta_{ij}^{(l)}$, are related to the collision integrals, $\pi\overline{\Omega}_{ij}^{(l,l)}$, which define the average collision cross-section between species i and j. Their expression is given in Gupta et al. (1990) as

$$\begin{aligned} \Delta_{ij}^{(1)} =& \frac{8}{3}\left(\frac{2M_i M_j}{\pi RT\left(M_i + M_j\right)}\right)^{1/2} \pi\overline{\Omega}_{ij}^{(1,1)} \\ \Delta_{ij}^{(2)} =& \frac{16}{5}\left(\frac{2M_i M_j}{\pi RT\left(M_i + M_j\right)}\right)^{1/2} \pi\overline{\Omega}_{ij}^{(2,2)} \end{aligned}$$

Appropriate values for $\pi\overline{\Omega}_{ij}^{(l,l)}$ must be determined by the user but can often readily be found as curve fits to temperature in the literature; see Levin and Wright (2004) and Wright et al. (2005) for discussions of available collision integral data pertinent to calculations in weakly ionized air. The expression for α_{ij} needed to compute the translational component of thermal conductivity is defined as

$$\alpha_{ij} = 1 + \frac{\left(1 - \frac{M_i}{M_j}\right)\left(0.45 - 2.54\frac{M_i}{M_j}\right)}{\left(1 + \frac{M_i}{M_j}\right)^2}$$